

MAGNETIC ANISOTROPY GRADED
MEDIA AND Fe-Pt ALLOY
THIN FILMS

by

ZHIHONG LU

A DISSERTATION

Submitted in partial fulfillment of the requirements
for the degree of Doctor of Philosophy in the
Department of Physics and Astronomy
in the Graduate School of
The University of Alabama

TUSCALOOSA, ALABAMA

2009

Copyright Zhihong Lu 2009
ALL RIGHTS RESERVED

ABSTRACT

Anisotropy graded media are promising to overcome the writability problem in achieving ultrahigh areal density for magnetic recording media. To more conveniently study and compare various media with regard to a particular figure of merit, a new energy landscape method of analysis is suggested. Using this method, the theoretical limit of the figure of merit for a graded medium is found to be 4. This limit can be approached by a graded medium with anisotropy quadratically increasing from zero to its maximum value. In order to characterize the anisotropy distribution of a graded medium, hard axis loops of graded media with various anisotropy profiles are simulated and analyzed. It is found that the second derivative of the hard axis loop can give useful information on the anisotropy distribution in a graded medium. $\text{Fe}_{50}\text{Pt}_{50}$ with the $L1_0$ structure, as one of the magnetically hardest materials, has great potential for media application. By using a first-principles calculation method, the magnetic and electronic structures of $L1_0$ structured $\text{Fe}_{50}\text{Pt}_{50}$ have been studied. These calculations show that although the ferromagnetic phase is the most stable phase for $\text{Fe}_{50}\text{Pt}_{50}$ with the $L1_0$ structure, there is a competition between the antiferromagnetic and the ferromagnetic phases when the ratio of lattice constants, c/a , decreases. Experimental investigations of $\text{Fe}_{50}\text{Pt}_{50}$ films with graded order parameter fabricated by varying the growth temperature during deposition demonstrate that these films have much smaller switching field than fully ordered $\text{Fe}_{50}\text{Pt}_{50}$, which suggests it is possible to make graded media by using this kind of films. $\text{Fe}_{100-x}\text{Pt}_x$ films with compositional gradient were also studied; however, the large easy axis dispersion in these films makes them

unsuitable for the fabrication of graded media. Films with $[\text{FePt}_3(\text{ordered})/\text{FePt}_3(\text{disordered})]_n$ superlattices were deposited on MgO substrates and sapphire substrates. It was found that the superlattices deposited on MgO substrates show higher exchange bias field. Polarized neutron reflectivity results show that ferromagnetic layers on MgO substrates contain more antiferromagnetic component than those on sapphire substrates. The larger exchange bias of the superlattice on MgO substrate is hypothesized to be due to larger exchange bias in its ferromagnetic layers.

ACKNOWLEDGMENTS

I wish to express my sincerest gratitude to my advisor, Dr. William H. Butler for his instructive guidance during all the period of my Ph.D. study. I really appreciate that he offered me a great chance to collaborate with other professors. I believe this kind of experience will be beneficial to my future career.

I would like to thank Dr. Gary Mankey, for his infectious enthusiasm and infinite patience while teaching me vacuum science and various experimental techniques.

I am very grateful to Dr. Pieter Visscher who gave me many instructions in micromagnetic simulation and always patiently answered my questions.

I would like to thank to Dr. J. W. Harrell, for his kind and supportive suggestions in my research.

I would like to thank the Department of Physics and the MINT center for providing financial assistance in the form of tuition and stipend through the years.

I am indebted to my dissertation committee, comprised of Dr. Gary Mankey, Dr. J. W. Harrell, Dr. Pieter Visscher, Dr. Gregory Thompson, and Dr. Jerome Busenitz, for their time and suggestions.

I would like to thank Dr. Shishou Kang and Dr. Yashuhiro Fukuma, former post doctoral fellows at the MINT Center, for their valuable suggestions and collaboration in some of my projects.

Thanks are also due to James Weston and John Hawkins, former and current facility manager, for providing technical support and training me on various instruments. I would

also like to thank Jason Foster (MINT Center) for computer support. Thanks are also given to all the wonderful office staff, Tabatha, Jamie and Casey, for streamlining travel arrangements and the tactful handling of administrative issues.

I would like to acknowledge several colleagues and former UA students, such as Shifan Shi, Weihao Xu, Shuxia Wang, and Qunshen Liu, for friendly help and discussion.

I would like to thank my parents for their constant love and understanding. I owe all my success to their faith in my abilities.

CONTENTS

ABSTRACT.....	ii
ACKNOWLEDGMENTS	iv
LIST OF TABLES.....	ix
LIST OF FIGURES	x
CHAPTER 1 INTRODUCTION	1
1.1 Background of Magnetic Recording Media	1
1.2 Trilemma in Magnetic Recording	3
1.3 Methods for Escaping the Recording Trilemma.....	6
1.4 Exchange Coupled Composite (ECC) Media and Graded Media	8
1.5 Reader Head and Exchange Bias	12
CHAPTER 2 DOMAIN WALL SWITCHING – ENERGY LANDSCAPE OPTIMIZATION.....	14
2.1 One-Dimensional Model.....	14
2.2 Media with a Uniform Perpendicular Magnetic Anisotropy	18
2.3 Theoretical Limit for the Figure of Merit	21
2.4 Multilayer Exchange Coupled Composite Media and Graded Media.....	23
CHAPTER 3 ANISOTROPY GRADED MEDIA: MAGNETIC CHARACTERIZATION....	36
3.1 LLG Simulation and Convergence	36
3.2 Easy Axis Loops of Graded Media	39
3.3 Effects of a Lateral Field	42

3.4	Hard Axis Loops of Graded Media and the Anisotropy Distribution Function	46
CHAPTER 4	FIRST PRINCIPLES STUDY OF MAGNETIC AND ELECTRONIC STRUCTURES OF L1 ₀ MPt (M=Fe AND Mn)	57
4.1	Calculation Method.....	58
4.2	Ground State of FePt and MnPt.....	62
4.3	Magnetocrystalline Anisotropy (MCA).....	63
4.4	Electronic Structure – Density of States	66
4.5	Effects of c/a Value on Magnetic and Electronic Properties	69
4.6	Discussion Based on Electronic Structures of FePt and MnPt	75
4.7	Band Structure of MnPt near the Fermi Energy	78
CHAPTER 5	EXPERIMENTAL TECHNIQUES AND EQUIPMENT.....	81
5.1	Sample Fabrication – Sputtering System	81
5.2	Crystal Structure Characterizations – X-ray Diffractometry	87
5.3	Magnetic Characterizations – Alternating Gradient Magnetometry.....	90
5.4	Characterization of Magnetic Structures – Neutron Scattering and Polarized Neutron Reflectometry.....	93
CHAPTER 6	MAGNETIC PROPERTIES OF Fe ₅₀ Pt ₅₀ FILMS WITH GRADED ORDER PARAMETERS	100
6.1	Sample Fabrication and Order Parameter Determination	101
6.2	Crystal Structures and Magnetic Properties of Uniform Fe ₅₀ Pt ₅₀ Films	105
6.3	Structures and Magnetic Properties of Fe ₅₀ Pt ₅₀ Thin Films with Graded Order Parameters.....	112
CHAPTER 7	MAGNETIC PROPERTIES OF EPITAXIAL Fe _{100-x} Pt _x (001) UNIFORM FILMS AND MULTILAYERS	118
7.1	Sample Preparation	118
7.2	Structures and Magnetic Properties of Uniform Fe _{100-x} Pt _x (x≥33) Films	122

7.3 Structures and Magnetic Properties of Uniform Fe ₇₅ Pt ₂₅ Films	126
7.4 Magnetic Properties of Fe _{100-x} Pt _x Films with Graded Compositions (25≤x≤50).....	129
CHAPTER 8 MAGNETIC STRUCTURE OF FePt ₃ AND SELF-EXCHANGE BIAS IN FePt ₃ (ORDERED)/FePt ₃ (DISORDERED) SUPERLATTICES	132
8.1 Sample Preparation	134
8.2 Determination of Order Parameter and Growth Temperature	135
8.3 Order Parameter Modulation in FePt ₃ (Ordered)/FePt ₃ (Disordered) Superlattices.	139
8.4 Magnetic Spin Configurations of a Fully Ordered FePt ₃ Film.....	141
8.5 Magnetic Structure and Interface of [FePt ₃ (Ordered)/FePt ₃ (Disordered)] _n Superlattice Films on MgO Substrates	144
8.6 Magnetic Structure and Interface of [FePt ₃ (Ordered)/FePt ₃ (Disordered)] _n Superlattice Films on Sapphire Substrates	147
8.7 Exchange Bias in [FePt ₃ (Ordered)/FePt ₃ (Disordered)] _n Superlattice Films	154
CHAPTER 9 CONCLUSIONS	158
REFERENCES	162

LIST OF TABLES

Table 4.1. Calculated and experimental lattice constants, magnetic moments and relative energies of the three possible magnetic structures (shown in Fig. 4.1) of MnPt and FePt (energies are given relative to the most stable phases).....	63
Table 4.2. Energies (relative to [100]) and atomic magnetic moments of FePt.	64
Table 4.3. Energies (relative to [100]) and atomic magnetic moments of MnPt.....	65
Table 4.4. Lattice constants and distances between atoms at different c/a.....	76
Table 6.1. Parameters for the calculations of (001) and (002) peak intensities.....	105
Table 7.1. Sputtering rates and powers of Fe and Fe ₅₀ Pt ₅₀ for co-sputtering of Fe _{100-x} Pt _x	122
Table 7.2. Parameters for the calculations of peak intensities of fully ordered Fe ₇₅ Pt ₂₅	126
Table 8.1. Parameters for the calculations of (001) and (002) peak intensities.....	135
Table 8.2. Model for the X-ray reflectivity fitting.....	145
Table 8.3. Thicknesses and interface roughness in the FePt ₃ /FePt ₃ superlattice film on a sapphire substrate.....	150

LIST OF FIGURES

Fig. 1.1. Growth of the areal density of conventional recording media [1].....	1
Fig. 1.2. Cartoon for the track structure of a hard disc medium [10].	2
Fig. 1.3. Energy barrier for binary magnetic recording.	3
Fig. 1.4. Trilemma in Magnetic recording.....	5
Fig. 1.5. Longitudinal recording and perpendicular recording.	6
Fig. 1.6. Two-spin model of ECC media.	9
Fig. 1.7. Typical Structure of the TMR device used in reader heads.	13
Fig. 2.1. One-dimensional model for the energy landscape calculation.....	15
Fig. 2.2. Energy landscape $E(m_z)$ for a Stoner-Wohlfarth particle.	19
Fig. 2.3. Energy landscape $E(m_z)$ for a particle with a small exchange parameter.....	20
Fig. 2.4. Magnetization profiles for the particle whose energy landscape is shown in Fig. 2.3..	21
Fig. 2.5. Energy landscape for grains with the same energy barrier and moment.....	22
Fig. 2.6. Energy landscape (a) and magnetization profiles (b) for a particle with two different anisotropy energies.	24
Fig. 2.7. Comparison of energy landscapes among particles with different anisotropy profiles..	26
Fig. 2.8. Anisotropy profile (a) and energy landscape (b) of a particle with a quadratic anisotropy distribution.	27
Fig. 2.9. Energy landscapes for grains with different grain lengths.	28
Fig. 2.10. Dependence of the figure of merit and coercivity on grain length.....	30
Fig. 2.11. Anisotropy profile (a) and energy landscape (b) for a grain with a finite anisotropy at the soft end.	31

Fig. 2.12. Anisotropy profile (a) and energy landscape (b) for a grain with a soft-tail.	32
Fig. 2.13. Comparison between energy landscapes of grains with and without a hard tail.	33
Fig. 2.14. Dependence of Energy barrier, figure of merit and coercivity on the exchange stiffness constant.	34
Fig. 3.1. Change of the moment (m_z) as a function of time.	38
Fig. 3.2. Comparison of the simulated easy axis loops when a grain is separated into 26 cells and 31 cells.	39
Fig. 3.3. Comparison of the simulated easy axis loops of a grain with and without the demagnetizing field being considered .The grain has a quadratic anisotropy profile.	40
Fig. 3.4. Easy axis loops of a grain with a quadratic anisotropy profile and a nonzero anisotropy in the soft-end (a) and a grain with a linear anisotropy profile (b).	42
Fig. 3.5. Effect of a lateral field on the hysteresis loops of a grain with a quadratic anisotropy profile: a) Demagnetizing field not considered (the insert shows the part of curves corresponding to domain wall nucleation); b) Demagnetizing field considered.	43
Fig. 3.6. Dependence of H_c on the applied field direction for a grain with a quadratic anisotropy profile and $K_{soft}=0$	44
Fig. 3.7. Dependence of H_c on the applied field direction for a grain with a quadratic anisotropy profile and $K_{soft} \neq 0$	45
Fig. 3.8. Cartoon for deriving hard axis loop of a grain by the superposition of hard axis loops of different layers when there is no exchange interaction.	47
Fig. 3.9. Hard axis loops for grains with a quadratic anisotropy profile or a linear anisotropy profile.	50
Fig. 3.10. Effect of the exchange interaction on the anisotropy distribution function of a grain with a linear anisotropy profile.	52
Fig. 3.11. Effect of the demagnetizing field on the anisotropy distribution function.	53
Fig. 3.12. Comparison of anisotropy distribution functions derived by analytical method and numerical method for a grain with a quadratic anisotropy profile.	54
Fig. 3.13. Effect of the strength of the exchange interaction on the anisotropy distribution function of a grain profile when the demagnetizing field is considered.	55
Fig. 3.14. Effect of the demagnetizing field on the distribution function.	55

Fig. 4.1. Models considered.....	59
Fig. 4.2. Unit cell for energy comparison between structures.	59
Fig. 4.3. Formula unit cell of $L1_0$ structure and unit cell used in MCA calculations for model 3, (a); unit cell used in MCA calculations for model 1, (b) ; unit cell used in MCA calculations for model 2, (c).	60
Fig. 4.4. Convergence of the AFM-FM energy difference for FePt and MnPt.	61
Fig. 4.5. Convergence of MCA of FePt and MnPt.	62
Fig. 4.6. Moment configurations.....	64
Fig. 4.7. Total densities of states for the three considered structures of FePt and MnPt.....	66
Fig. 4.8. Comparison of angular momentum projected densities of states of each atom in FePt and MnPt.....	67-68
Fig. 4.9. Comparison of energies of the three structures of FePt at different c/a	70
Fig. 4.10. c/a dependence of the anisotropy energies of FePt.....	70
Fig. 4.11. Moment on each atom in FePt as a function of c/a	72
Fig. 4.12. Dependence of energies of MnPt on c/a	73
Fig. 4.13. Dependence of MCAs of MnPt on c/a	74
Fig. 4.14. Moment on each atom in MnPt as a function of c/a	75
Fig. 4.15. Comparison of PDOSs of each Mn atom in model 1 of MnPt at different c/a	77
Fig. 4.16. Energy bands of MnPt (model 1) near the Fermi energy along [100] and [001] directions.....	79
Fig. 5.1. Magnetron sputtering.....	82
Fig. 5.2. Sputtering system.	83
Fig. 5.3. Dependence of the growth temperature on the applied voltage.	85
Fig. 5.4. Relation between the real growth temperatures and the thermocouple readings.	86
Fig. 5.5. X-ray diffraction.	87

Fig. 5.6. Structure of the X-ray diffractometer	89
Fig. 5.7. Definition of angles: θ , ω , φ and ψ	90
Fig. 5.8. AGM probe and sample position.....	91
Fig. 5.9. Structure of Model 2900 MicroMag™ AGM [73].....	92
Fig. 5.10. Angular relation between the scattering vector and the magnetic interaction vector for magnetic neutron scattering [75].....	94
Fig. 5.11. Scattering geometry of polarized neutron reflectometry.....	97
Fig. 6.1. Structure of samples with a uniform Fe ₅₀ Pt ₅₀ film.	102
Fig. 6.2. X-ray diffraction spectra of samples deposited at different temperatures.....	106
Fig. 6.3. Dependence of the order parameter S and the lattice constant c on the growth temperature T _g	107
Fig. 6.4. (111) pole figures of the Fe ₅₀ Pt ₅₀ film and MgO substrate.....	108
Fig. 6.5. Dependence of FWHM on the growth temperature.	109
Fig. 6.6. Magnetic properties of Fe ₅₀ Pt ₅₀ films deposited at different growth temperatures.....	110
Fig. 6.7. Dependence of magnetic anisotropy on the order parameter.	111
Fig. 6.8. Structure of the sample stacked with 4 Fe ₅₀ Pt ₅₀ layers deposited at different T _g s.	113
Fig. 6.9. X-ray diffraction spectrum and peak analysis.	114
Fig. 6.10. Magnetic properties of the sample with Fe ₅₀ Pt ₅₀ layers deposited at 4 different T _g s.....	115
Fig. 6.11. Structure of the sample stacked with Fe ₅₀ Pt ₅₀ layers deposited at a continuously decreased temperature.....	115
Fig. 6.12. X-ray diffraction spectrum of the sample stacked with Fe ₅₀ Pt ₅₀ layers deposited at a continuously decreased temperature.	116
Fig. 6.13. Magnetic properties of the sample stacked with Fe ₅₀ Pt ₅₀ layers deposited at a continuously decreased temperature.	117
Fig. 7.1. Dependence of sputtering rate on sputtering power.	121

Fig. 7.2. Structure of uniform $\text{Fe}_{100-x}\text{Pt}_x$ ($x \geq 33$) thin films.	122
Fig. 7.3 X-ray diffraction patterns of $\text{Fe}_{100-x}\text{Pt}_x$ films.	123
Fig. 7.4. Dependence of FWHM of (001) peak on the composition of $\text{Fe}_{100-x}\text{Pt}_x$ films.	123
Fig. 7.5. Magnetic properties of $\text{Fe}_{100-x}\text{Pt}_x$ films.	125
Fig. 7.6. X-ray diffraction spectra of $\text{Fe}_{75}\text{Pt}_{25}$ films deposited at 400°C and 600°C.	127
Fig. 7.7. Magnetic properties of $\text{Fe}_{75}\text{Pt}_{25}$ thin films deposited at 400°C and 600°C.	128
Fig. 7.8. Structures for samples with graded compositions.	129
Fig. 7.9. X-ray diffraction spectra and magnetic properties of samples with graded compositions.	130
Fig. 8.1. X-ray diffraction patterns of films deposited at different temperatures.	138
Fig. 8.2. X-ray diffraction spectra of $\text{MgO}/\text{Pt}(4\text{nm})/\text{Cr}(3\text{nm})[\text{FePt}_3(x \text{ nm})(600^\circ\text{C})/\text{FePt}_3(10\text{nm})(400^\circ\text{C})]_5$	140
Fig. 8.3. X-ray diffraction pattern of $\text{MgO}/\text{Pt}(4\text{nm})/\text{Cr}(3\text{nm})[\text{FePt}_3(20 \text{ nm})(600^\circ\text{C})/\text{FePt}_3(10\text{nm})(500^\circ\text{C})]_5$	141
Fig. 8.4. Temperature dependence of the $(\frac{1}{2} \frac{1}{2} 0)$ neutron scattering peak of the fully ordered FePt_3 film.	142
Fig. 8.5. Temperature dependence of (200) and (110) peaks of the fully ordered FePt_3 film.	143
Fig. 8.6. X-ray reflectivity spectrum of a $[\text{FePt}_3/\text{FePt}_3]_n$ superlattice film and its fit.	144
Fig. 8.7. Neutron reflectivity spectra of $\text{MgO}/\text{Cr}(3\text{nm})/\text{Pt}(16\text{nm})/[\text{FePt}_3(20\text{nm})(600^\circ\text{C})/\text{FePt}_3(10 \text{ nm})(400^\circ\text{C})]_5/\text{Pt}(7.5\text{nm})$ at a temperature of 5K and their fits.	145
Fig. 8.8. Scattering length density profile of $\text{MgO}/\text{Cr}(3\text{nm})/\text{Pt}(16\text{nm})/[\text{FePt}_3(20\text{nm})(600^\circ\text{C})/\text{FePt}_3(10 \text{ nm})(400^\circ\text{C})]_5/\text{Pt}(7.5\text{nm})$	146
Fig. 8.9. X-ray diffraction spectrum of $\text{Al}_2\text{O}_3/\text{Pt}(16\text{nm})/[\text{FePt}_3(40\text{nm})(600^\circ\text{C})/\text{FePt}_3(10\text{nm})(400^\circ\text{C})]_5/\text{Pt}(7.5\text{nm})$	147
Fig. 8.10. Neutron scattering intensity of the $(\frac{1}{2} \frac{1}{2} 0)$ peak of $\text{Al}_2\text{O}_3/\text{Pt}(16\text{nm})/[\text{FePt}_3(40 \text{ nm})(600^\circ\text{C})/\text{FePt}_3(10\text{nm})(400^\circ\text{C})]_5/\text{Pt}(7.5\text{nm})$ as a function of temperature.	148
Fig. 8.11. Neutron scattering intensities of (-200) and (110) peaks of $\text{Al}_2\text{O}_3/\text{Pt}(16\text{nm})/[\text{FePt}_3(40\text{nm})(600^\circ\text{C})/\text{FePt}_3(10\text{nm})(400^\circ\text{C})]_5/\text{Pt}(7.5\text{nm})$ as a function of temperature.	149

Fig. 8.12. Neutron reflectivity spectra and the fit of $\text{Al}_2\text{O}_3/\text{Cr}(3\text{nm})/\text{Pt}(12\text{nm})/[\text{FePt}_3(40\text{nm})$ $(600^\circ\text{C})/\text{FePt}_3(10\text{nm})(400^\circ\text{C})]_5/\text{Pt}(7.5\text{nm})$ (at 325K).....	150
Fig. 8.13. Neutron reflectivity spectra of $\text{Al}_2\text{O}_3/\text{Cr}(3\text{nm})/\text{Pt}(16\text{nm})/[\text{FePt}_3(40\text{nm})(600^\circ\text{C})/$ $\text{FePt}_3(10\text{nm})(400^\circ\text{C})]_5/\text{Pt}(7.5\text{nm})$ at different temperatures and the related fits.	151
Fig. 8.14. Magnetization in disordered FePt_3 as a function of temperature (derived by fitting).	152
Fig. 8.15. Asymmetry ratio as a function of scattering angle at different temperatures.....	153
Fig. 8.16. Asymmetry ratio at $\theta = 0.44^\circ$ in disordered FePt_3 as a function of temperature.	154
Fig. 8.17. Hysteresis loops of the $[\text{FePt}_3/\text{FePt}_3]_n$ superlattice film deposited on a MgO substrate.	155
Fig. 8.18. Hysteresis loops of the $[\text{FePt}_3/\text{FePt}_3]_n$ superlattice film deposited on a sapphire substrate.	155
Fig. 8.19. Exchange bias as a function of temperature.	156

CHAPTER 1 INTRODUCTION

1.1 Background of Magnetic Recording Media

Current status and challenge

The hard disk drive (HDD) is a main device for data storage and plays a key role in advanced information technology. The continuing demand for higher recording capacity and smaller HDD size has pushed the HDD industry to keep chasing higher and higher areal density. Fig. 1.1 shows the development of HDDs in the past about fifty years.

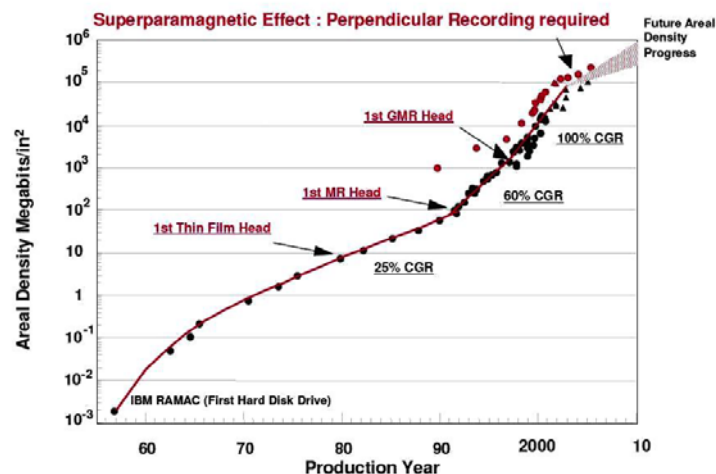


Fig. 1.1. Growth of the areal density of conventional recording media [1].

The decade from 1992 to 2002 was a “golden time” for the HDD industry. During these years, the areal density increased at a rate of 60 to 100% each year [2]. In recent years, the rate of increase of areal density has slowed to 30% due to the limitations arising from the so-called superparamagnetic limit. At the same time, the development of other kinds of recording technologies such as flash drives [3-6] and solid state drives (SSD) [7-9] bring increasing

challenges to the HDD industry. To meet these challenges, improvements are needed in the magnetic recording technology to overcome the superparamagnetic limit and to further increase the areal density.

Areal density of HDD

The areal density is a measure of the number of bits that can be stored in a unit of area. It is usually expressed in bits per square inch. The surface of a disk platter is partitioned into many recording tracks as shown in Fig. 1.2. Information is recorded in each track. Therefore, the areal density is determined by the track density and linear density.

- **Track Density:** This is a measure of how tightly the concentric tracks on the disk are packed. It is a measure of how many tracks can be placed in an inch of radius on a platter.
- **Linear or Recording Density:** This is a measure of how tightly the bits are packed within a length of track. Every track on the surface of a platter is a different length (because they are concentric circles), and not every track is written with the same density. Manufacturers usually quote the maximum linear density used on each drive.

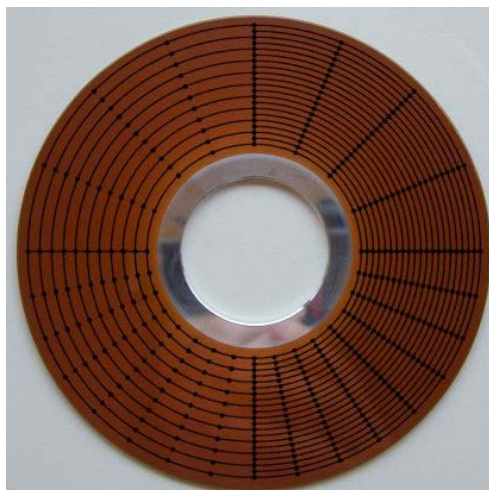


Fig. 1.2. Cartoon for the track structure of a hard disc medium [10].

1.2 Trilemma in Magnetic Recording

Thermal stability and superparamagnetic limit

For binary recording, the “1” and “0” are represented by the two magnetization states (spin up or spin down) of magnetic grains with an energy barrier, ΔE , between them as shown in Fig. 1.3. To switch between two states, enough energy is needed to overcome this energy barrier. Thus, in the normal condition, the state can only be changed by applying a large enough magnetic field. This is how the information can be written and stored. However, if the energy barrier is low, thermal fluctuation may cause the grains to switch between states and lead to the loss of recorded information.

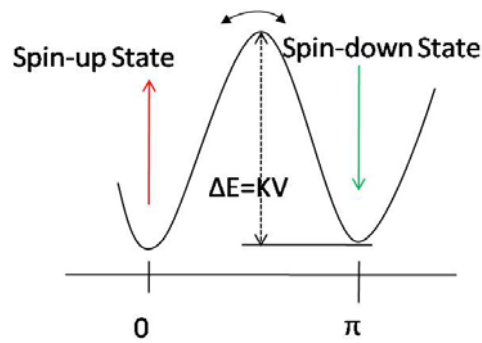


Fig. 1.3. Energy barrier for binary magnetic recording.

The rate of the thermal switching can be expressed by the Néel-Arrhenius equation [11, 12]:

$$\frac{1}{\tau} = f_0 e^{-\Delta E/k_B T} \quad (1.1)$$

where τ is the relaxation time, f_0 is called the attempt frequency, ΔE is the energy barrier between spin up and spin down state, k_B is the Boltzmann constant and T is the temperature.

For a Stoner-Wohlfarth (SW) particle, the energy barrier is proportional to its magnetic anisotropy and can be expressed as

$$\Delta E = K_u V \quad (1.2)$$

where K_u is the magnetic anisotropy of the grain and V is the volume of the grain. Thus, for a given material (K_u is constant), with the decrease of grain size, the energy barrier decreases. At some critical size, the energy barrier becomes comparable to the thermal energy $k_B T$, and the grain becomes thermally unstable. This critical size is called the superparamagnetic limit for the material.

In the current magnetic recording industry, achieving higher recording density is always the goal. Higher recording density means smaller grain size. However, we cannot trade recording density off for thermal stability. To increase recording density and, at the same time, maintain the thermal stability, one must increase the anisotropy of the grain, which means using a magnetically hard material to make the recording media.

Writability

The application of a magnetically hard material (with large anisotropy energy K_u) in magnetic recording media will make the medium thermally stable with a very small grain size. Thus, we can achieve very high recording density without worrying about thermal stability. However, another problem called the “writability problem” can occur when using magnetically hard materials as recording media. For a Stoner-Wohlfarth particle, the switching field H_c is

$$H_c = 2K_u/M_s \quad (1.3)$$

where M_s is the saturation magnetization of the particle. Therefore, a grain of a hard material needs a large magnetic field to switch. Theoretically, the highest value of a magnetic field that can be achieved depends on the M_s of the head material, and is approximately 2.3 T [13]. If a medium is made of a very hard material, the write-head may not be able to provide a field large enough to write it.

Signal-to-noise ratio (SNR)

For conventional thin film media, noise mainly comes from the transition region between two neighboring bits due to the interactions among grains [14, 15]. The SNR of the reproduced signal is proportional to the number of grains in the recording region [16, 17]. Thus as the areal density increases, the size of the grains must decrease in order to maintain the SNR.

Recording trilemma [18]

The thermal stability, writability and signal-to-noise ratio are three very important properties for a magnetic recording medium. Since each puts different requirements on a medium, the concern about them leads to a so-called recording trilemma as shown in Fig. 1.4.

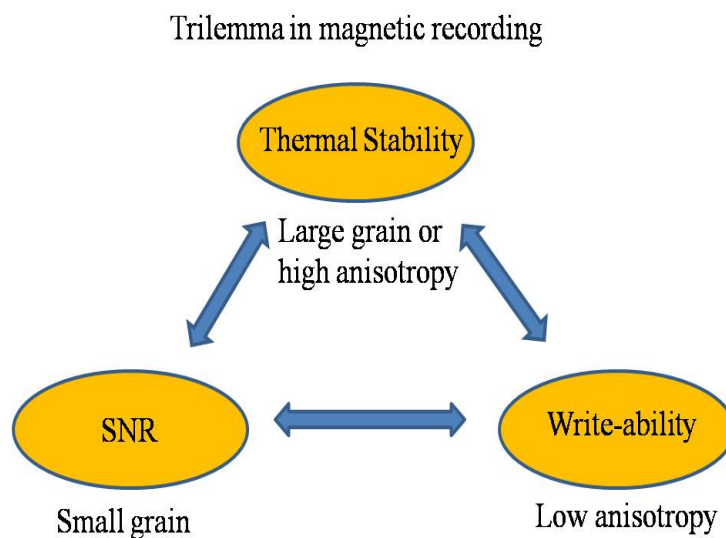


Fig. 1.4. Trilemma in Magnetic recording.

To achieve good thermal stability for a medium, a large grain size or anisotropy is desirable; to achieve good writability, it is better to use materials with a small anisotropy; and to get a high signal-to-noise ratio, a small grain size is better.

1.3 Methods for Escaping the Recording Trilemma

Perpendicular recording and longitudinal recording

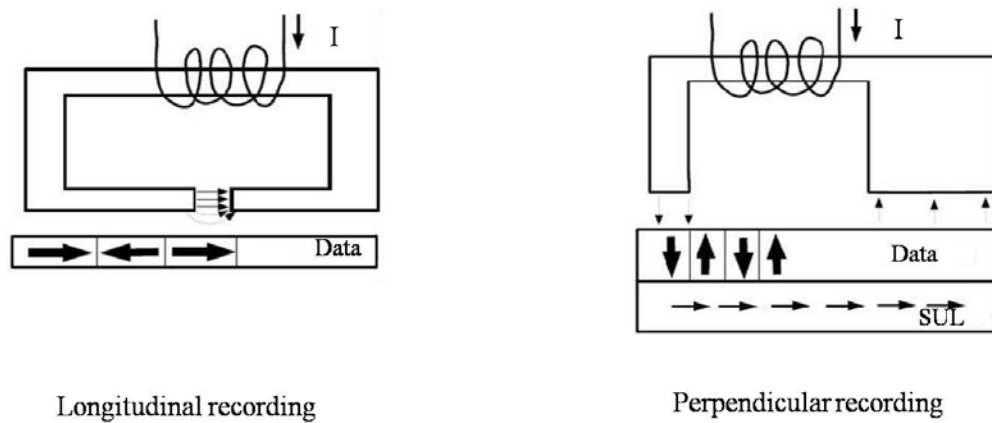


Fig. 1.5. Longitudinal recording and perpendicular recording.

There are two kinds of magnetic recording mode: longitudinal and perpendicular. For the longitudinal magnetic recording mode, the magnetization of each data bit in the magnetic recording medium is aligned parallel to the drive's spinning platter. In perpendicular recording, the magnetization of the bit is aligned vertically or perpendicularly in relation to the disk drive's platter.

Perpendicular recording is believed to be able to obtain higher recording density than longitudinal recording because of the following advantages:

1) Perpendicular recording allows thicker films for recording media because of the decrease of the demagnetizing field.

2) A vertical pole head in a recording media with a soft underlayer can generate twice the field of longitudinal recording head, which allows writing a medium with a higher anisotropy.

3) The read-back signal amplitude from a perpendicular medium with a soft underlayer is larger than that of an equivalent longitudinal medium, improving the signal-to-noise ratio.

4) The track edges in perpendicular medium are less noisy and better defined due to the vertical pole head configuration. Sharp track edges allow a higher track density and a smaller bit aspect ratio.

Replacing longitudinal recording with perpendicular recording is the first step to escape the recording trilemma. From now on, all of our discussions are based on perpendicular recording.

New concepts of magnetic recording media and comparison

To escape the recording trilemma, several new concepts of magnetic recording media have been suggested:

1) Bit patterned media (BPM) [19-22] – large grains with one grain representing one bit. The increase of grain size allows the use of materials with smaller K_u .

2) Energy assisted switching [23-26] (thermal assist or microwave assist) – small grain size, decreasing writing field by external energy.

3) Non-SW switching (exchange coupled composite media [27-31] and graded media [32-34]) – small grain size, decreasing writing field by domain wall motion.

The fabrication of bit patterned media needs new nano-technology such as nano-imprint lithography [35] which is presently under development. No mature technology exists for media fabrication.

Energy assist methods need to add additional devices such as a laser or microwave generator and the waveguide to lead a beam to the bit for writing, which will bring new difficulties in fabrication.

Exchange coupled composite media and graded media which are based on conventional media technologies seem more promising.

1.4 Exchange Coupled Composite (ECC) Media and Graded Media

Figure of merit

To evaluate a medium, we thus need to consider both the thermal stability and the writability. Victora introduced a figure of merit which was expressed as [36]

$$\xi = \frac{2\Delta E}{H_c M_s V} \quad (1.4)$$

where ΔE is the energy barrier, H_c is the coercivity of the medium and M_s is the saturation magnetization of the medium.

For a conventional perpendicular medium, each grain of the medium can be considered as a Stoner-Wohlfarth particle. The switching field is equal to $2K_u/M_s$ and the figure of merit is equal to 1 when a field is applied along the easy axis. However, when a field is applied 45° away from easy axis, the coercivity decreases to K_u/M_s and the figure of merit increases to 2. To realize a figure of merit equal to 2, the easy axis should be 45° from the surface normal – tilted media [37-38]. Although tilted media can yield better writability without decreasing thermal stability leading to a concomitant increase of areal density by a factor of 2, this idea has been found experimentally unfeasible because it would require the anisotropy to be circumferentially (or radially) ordered on the disk, which is difficult to realize in experiment. On the other hand, tilting the easy axis to 45° from the surface normal can only decrease the coercivity by a factor of 2 which might not be enough for the application of materials with ultrahigh anisotropy such as $L1_0$ phase FePt and CoPt in recording media – the coercivity is still too high to write.

Exchange coupled composite (ECC) media

The concept of exchange coupled composite media was proposed in 2004 by Victora *et al.* [39] and Suess *et al.* [40]. A typical ECC medium consists of magnetic grains with a soft/hard

bilayer structure with the magnetic hard layer determining the thermal stability and the magnetic soft layer helping the switching of the hard layer.

Victoria and Shen [36] first used a two-spin model (as shown in Fig. 1.6) to study bilayer ECC media. $K_{us}(K_{uh}), M_{ss}(M_{sh})$ and $t_s(t_h)$ represent the anisotropy, magnetization and thickness of soft layer (hard layer), respectively.

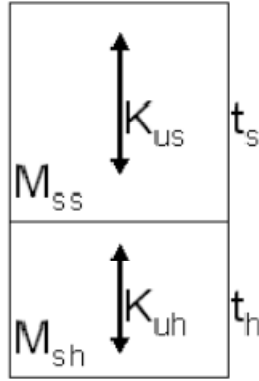


Fig. 1.6. Two-spin model of ECC media.

The two-spin model predicts that the figure of merit of bilayer ECC media depends greatly on the ratio $(M_{ss}t_s)/(M_{sh}t_h)$. The figure of merit approaches 2.0 when $(M_{ss}t_s)/(M_{sh}t_h) \geq 10$.

The two-spin model is a rough model which supposes that the exchange interactions within the soft layer and the hard layer are so strong that the all the spins in each layer rotate coherently. This approximation is only true when the thicknesses of both layers are smaller than the domain wall thickness. The domain wall in the soft layer is infinitely thick when there is no applied field. When a magnetic field is applied, the domain wall thickness will be compressed to approximately [41]

$$\delta_{dw} = \sqrt{2A_{soft}/H_{appl}M_{soft}} \quad (1.5)$$

where H_{appl} , A_{soft} and M_{soft} are the applied field, and exchange stiffness constant and magnetization of soft layer, respectively. For a soft layer with $A_{soft}=10^{-11}$ J/m and $M_{soft}=1.256$ T (~ 1000 emu/cm³ in cgs), when applying a field of 1T, the domain wall width is about 5.4 nm. The domain thickness of the hard layer can be estimated by

$$\delta_{dw} = \pi\sqrt{A_{hard}/K_{hard}} \quad (1.6)$$

where A_{hard} and K_{hard} represent the exchange stiffness constant and anisotropy of the hard layer, respectively. For a hard layer with $A_{hard}=10^{-11}$ J/m, $K_{hard}=6\times 10^6$ J/m³, such as L1₀ FePt, the domain wall thickness is about 4 nm.

For a grain with total thickness t_{tot} ($t_{tot} = t_{soft} + t_{hard}$) larger than 10 nm, the two-spin model cannot give accurate results. To better study the switching behavior in a realistic medium (t_{tot} is 10-20 nm), a more accurate model – the spin-chain model should be used. By using the spin-chain model, H. Krommuller and D. Goll [42] derived a simple analytical formula describing the switching field of a composite system with infinitely thick soft and hard layers exchange coupled to each other

$$H_{sw} = \frac{H_{hard} - \gamma H_{soft}}{(1 + \gamma)^2} \quad (1.7)$$

where $\gamma = \frac{A_{soft}M_{soft}}{A_{hard}M_{hard}}$, H_{hard} and H_{soft} are the switching fields of the hard layer and soft layer.

Micromagnetic simulation [43, 44] of the switching process of the spin chain model shows that in a bilayer composite structure, the switching involves domain wall motion. When a magnetic field is applied, a domain wall first nucleates in the soft end. After nucleation, the domain wall will move to the soft/hard interface and be pinned there. Further increasing the applied field forces the domain wall to penetrate into the hard layer. Once the applied field reaches the critical field, the domain wall depins from the interface and propagates through the

entire hard layer. Since the switching involves domain wall motion, this kind of switching is called domain wall assisted switching.

Based on Eq. 1.7, Dobin and Richter derived the figure of merit to be [41]

$$\xi = \frac{(1 + \gamma)^2}{1 + \sqrt{\gamma}(1 + \sqrt{\gamma/4})} \quad (1.8)$$

Eq. 1.8 predicts a maximum figure of merit $\xi_{max} = 4.25$,and $\xi = 2.6$ for $\gamma = 1.0$. However, this is overestimated because equation 1.7 was derived for a system with infinite thickness, and is not true for system with finite thickness. Suess predicts $\xi = 2$ for $\gamma = 1.0$ [43].

Anisotropy graded media

The figure of merit can be further increased by more gradually changing the anisotropy in a medium and the concept of exchange coupled composite media can be accordingly extended to the multilayer case. If the anisotropy in a medium changes continuously, the medium is called a graded medium. Suess showed that a multilayer structure with a continuously increasing anisotropy from layer to layer can have an arbitrarily small switching field while keeping the energy barrier constant [44]. However, this can only be realized for a system with infinite thickness. For the realistic case, the thickness of a medium is about 10-20 nm. It is more useful to study the increase of the figure of merit in a system with finite thickness and with varying anisotropy distribution.

Experimental study in ECC media

Shen *et al.* [39] fabricated exchange coupled composite media by using granular FeSiO as the soft layer and $(\text{Co/PdSi})_n$ as the hard layer. The exchange interaction between the soft layer and the hard layer was manipulated through a PdSi interlayer. They found that, for a properly chosen interlayer thickness, the coercivity of the media is reduced to 1.75 kOe,

compared to the 4.35 kOe coercivity of the hard layer. If there is no interlayer, the coercivity becomes 2.91 kOe, which is close to the calculated value 2.8 kOe for the strongly coupled case.

So far, the experimental studies of ECC media are still very few and only focused on the bilayer structure, no experimental results on multilayer ECC media and graded media have been reported.

1.5 Reader Head and Exchange Bias

To realize ultrahigh density in magnetic recording, we need to overcome the so-called recording trilemma. To do this, more effort is needed to improve the recording media (increasing areal density at attainable writing field and acceptable thermal stability) and the write head (enhancing the writing field). The importance of the reader head has not been mentioned so far. A HDD with ultrahigh recording density also needs reader heads with better linear resolution and smaller size to read the recorded data. Actually, the increase of areal density of the recording media must be accompanied by the increase of linear resolution of the reader heads and the down-scaling of the size of the reader heads.

Currently, reader heads are made of tunneling magnetoresistive (TMR) devices. The basic structure of a TMR device is in Fig. 1.7. The antiferromagnetic (AFM) layer is used to pin the reference layer by the so-called exchange bias [45-47]. The stability of the reader head depends on the exchange bias due to the AFM layer. The higher the exchange bias, the more stable the head. To further scale down the size of the head, the exchange bias field should be increased. To obtain a stronger exchange bias, the selection of antiferromagnetic materials and a better understanding of the exchange bias are very important.

Capping layer
Free layer
Barrier
SAF
Antiferromagnetic layer
Seed layer
Substrate

Fig. 1.7. Typical Structure of the TMR device used in reader heads.

The reading signal and the background signal of a reader head are as follows:

$$V_{signal} \propto \Delta(RA) \quad (1.9)$$

$$V_{Background} \propto (RA) \quad (1.10)$$

where R is the resistance of the GMR or TGMR device and A is the area of the device.

To increase the resolution of the reader head, RA needs to be decreased. One way to do this is to use a device with small resistivity, much smaller than a TMR device. In recent years, giant magnetoresistive (GMR) devices with current perpendicular to plane (CPP) have shown promise for application in next generation high resolution reader heads [48-50]. In a CPP GMR device, to decrease the resistivity, it is better to use an AFM layer with smaller resistivity.

Exchange bias has been widely studied for years [51, 52]. However, the basic mechanisms leading to exchange bias are not quantitatively understood at this time. In past years, most of the studies on exchange bias were focused on the exchange bias of polycrystalline antiferromagnetic (AF) materials. The interface between a polycrystalline antiferromagnetic layer and a ferromagnetic (FM) layer is structurally complicated. It is helpful to investigate AF/FM interfaces that are structurally as perfect as possible for better understanding the exchange bias.

CHAPTER 2 DOMAIN WALL SWITCHING – ENERGY LANDSCAPE OPTIMIZATION

Introduction

To overcome the trilemma in magnetic recording, it is important to decrease the writing field of a medium, while at the same time, maintaining the thermal stability. One of the important parameters for evaluating recording media from this point of view is the Victora figure of merit which can be expressed as $\xi = \frac{2\Delta E}{H_c M_s V}$. To directly evaluate the figure of merit, two important parameters are needed – the energy barrier ΔE and the coercivity H_c . To easily evaluate a medium and compare different media from the point of view of the figure of merit, it is desirable to develop a new energy landscape in which ΔE and H_c can both be directly visualized. In this chapter, a new energy landscape, $E(m_z)$, which was developed based on a one-dimensional model, is reported. In this new energy landscape, both ΔE and H_c of a medium can be directly obtained and the figure of merit can be easily evaluated. By using this energy landscape, different kinds of media are studied and compared. The main content of this chapter is based on the presentation of reference 53 [53].

2.1 One-Dimensional Model

We consider a one-dimensional model as shown in Fig. 2.1, in which the magnetization $M(z)$ is a function only of one variable z (independent of x and y). We will allow the anisotropy $K(z)$, exchange constant $A(z)$, and saturation magnetization $M_s(z)$ to vary arbitrarily with z . Since we will perform computations with a discrete approximation to this continuum model (which

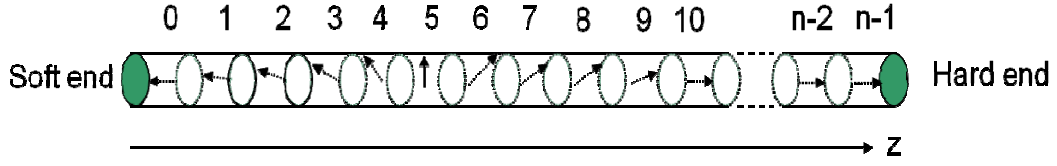


Fig. 2.1. One-dimensional model for the energy landscape calculation.

approaches the continuum model as the cell size goes to 0), we will write the energy in a discrete form. It has cells labeled by i , with magnetization vectors M_i . In the quasistatic energy minima we will consider, these vectors will lie in a plane, so they can be described by giving the angle θ_i of the magnetization relative to the long axis of the grain (the z -axis).

The energy (per unit area in the xy plane) E of our system is then given in terms of the values of K and M at each cell and A between each neighboring pair of cells by:

$$E = \sum_{i=1}^N a_i K_i \sin^2 \theta + \sum_{i=1}^{N-1} a_i \frac{2A_{i,i+1}}{a_{i,i+1}^2} \cos(\theta_{i+1} - \theta_i) + \sum_{i=1}^N a_i \mu_0 M_i H_i \cos \theta_i \quad (2.1)$$

where K_i is the (perpendicular) anisotropy at the center of cell i , a_i is the length of the cell i , $a_{i,i+1}$ is the distance between cells i and $i+1$, $A_{i,i+1}$ is the continuum exchange parameter evaluated between these cells, and H is the external field (assumed along z). For simplicity, we do not consider magnetostatic energy here – in similar systems, micromagnetic simulation has shown that this affects the coercivity by only a few percent.

We consider here quasistatic switching – we assume that we vary H in such a way that the system is always at a relative minimum (with respect to the θ_i s) of the energy. More precisely, we assume H is very slightly above this value, so that the magnetic moment which can be expressed as:

$$m_z = \sum_i^N a_i M_i \cos \theta_i \quad (2.2)$$

increases slowly, and we consider the limit in which the rate of increase approaches zero. Note that this is never true in a real switching event – after a domain wall has traversed most of the sample, it would require reversing H to keep the system quasistatic. However, by this time, it is irrelevant whether the system remains quasistatic (it will finish switching in either case) and in the initial stages, the quasistatic assumption is often reasonable.

It would appear that to find the quasistatic switching trajectory, in which H varies with time, we would need to minimize a function $E(\theta_1, \theta_2, \dots, \theta_N, H)$ of a large number of variables $\theta_1, \theta_2, \dots, \theta_N$, for each of H independently. However, there is a way around this. We can choose some coordinate in the space of θ_i s (we choose the longitudinal component of the magnetic moment m_z) and first minimize $E(\theta_1, \theta_2, \dots, \theta_N, H)$ for fixed m_z , obtaining a function (the constrained minimum energy) $E(m_z, H)$.

To constrain the total moment along z axis, we set $m_z = \text{const}$. Thus, according to Eq. 2.2, the change of m_z can be expressed as:

$$\Delta m_z = - \sum_i^N M_i \sin \theta_i \Delta \theta_i = 0 \quad (2.3)$$

The energy is minimized when the torque on each spin equal to zero, $\frac{\partial E}{\partial \theta_i} = 0$. To find the minimum, we can set,

$$\Delta \theta_i = -\lambda \frac{\partial E}{\partial \theta_i} \quad (2.4)$$

where λ is a constant.

By substituting Eq. 2.4 for $\Delta \theta_i$ in Eq. 2.3, we can get the equation below,

$$\sum_i^N \lambda M_i \sin \theta_i \frac{\partial E}{\partial \theta_i} = 0 \quad (2.5)$$

For simplicity, we only consider the case in which all cells have the same magnetization $M_i=M_s$, the same length $a_i=a$, and the same exchange stiffness constant $A_{ij}=A$. We thus replace energy E in Eq. 2.5 with 2.1 and we get

$$\sum_i^N \lambda M_s \sin \theta_i \left(\sum_i^N K_i \sin 2\theta_i + \sum_i^{N-1} \frac{2A}{a^2} \sin(\theta_{i+1} - \theta_i) - \sum_{i=1}^N \mu_0 M_s H \sin \theta_i \right) = 0 \quad (2.6)$$

where H is a field to keep the system static (constraint field) at certain m_z . It is not a real field.

By using Eq. 2.6, the constraint field H can be calculated for each iteration. And the new set of θ_i s also can be calculated by using

$$\theta_i(\text{new}) = \theta_i(\text{old}) + \Delta\theta_i \quad (2.7)$$

where $\theta_i(\text{new})$ and $\theta_i(\text{old})$ are the angles of the i th spin generated in the current iteration and last iteration respectively.

We thus can use the new set of θ_i s, H and $E(\theta_1, \theta_2, \dots, \theta_N, H)$ as the initial inputs for the new iteration. After this kind of iterative calculation, we can thus get the constrained minimum energy $E(\theta_1, \theta_2, \dots, \theta_N, H)$ for a fixed m_z .

After we get the constrained minimum energy, we can minimize $E(m_z, H)$ with respect to m_z , obtaining the same relative minimum $E(H)$ we would have obtained by unconstrained minimization. [Note that there may be more than one relative minimum, so we should call this $E_j(H)$ where j indexes the minima, but we will omit this index for simplicity.] The advantage of this apparently-circuitous method of finding the minimum is that the configuration minimizing $E(\theta_1, \theta_2, \dots, \theta_N, H)$ is actually independent of H ! This is apparent from Eq. 2.1, since the only dependence on H is the Zeeman term $\mu_0 m_z H$, which is a constant when m_z is held fixed. The result is that we need only to compute the constrained minimum energy at $H = 0$, and it is given at any other field H by

$$E(m_z, H) = E(m_z, 0) - \mu_0 m_z H \quad (2.8)$$

Furthermore, this energy is minimized at particular H by setting $\partial E(m_z, H)/\partial m_z = 0$, so the field necessary to hold m_z constant is given by

$$\mu_0 H = \frac{\partial E(m_z, 0)}{\partial m_z} \quad (2.9)$$

We conclude that everything we need to know about the system (the coercivity and energy barrier) is contained in the function $E(M_z)$, the minimum energy at fixed magnetic moment m_z and zero field. This result is very general.

2.2 Media with a Uniform Perpendicular Magnetic Anisotropy

When a grain is small, the switching of its magnetization will be coherent. Although we motivated our energy landscape by considering domain-wall switching, it describes Stoner-Wohlfarth (SW) switching as well. This is the limit in which K , A , and M_S are uniform and A is large so $M(z)$ is uniform. The SW energy (per unit area, of a grain of length L) is

$$E = KL \sin^2 \theta = KL \left(1 - \frac{m_z^2}{m_s^2} \right) \quad (2.10)$$

Here the saturation moment per unit area is $m_s = M_s L$. The $E(m_z)$ plot is a parabola, as shown in Fig. 2.2 . Note that the maximum slope of the curve which represents the field necessary to switch the grain is exactly the Stoner-Wohlfarth switching field $H_{sw} = 2K/M_s$, as expected.

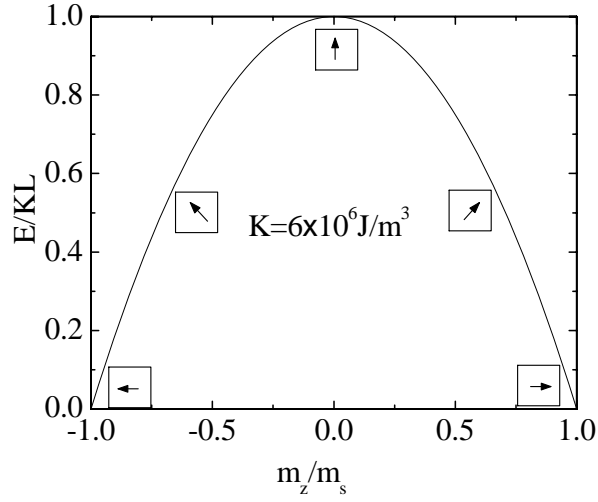


Fig. 2.2. Energy landscape $E(m_z)$ for a Stoner-Wohlfarth particle.

Another virtue of the function $E(m_z)$ is that it has exactly the same interpretation for a particle with a lower exchange constant A as for a SW (high A) particle. The behavior depends only on the dimensionless parameter $x=A/KL^2$, which is the square of the ratio of the exchange length to the particle length L . With low x , switching takes place through domain wall motion and the energy barrier is approximately the domain wall energy. This can be calculated analytically in an infinite system (we will refer to this as the thin-wall approximation, because it is valid when the wall is far from the system boundary and the material properties vary only slightly through the wall), the thin wall energy is:

$$\sigma_w = 4\sqrt{AK} = 4KL\sqrt{x} \quad (2.11)$$

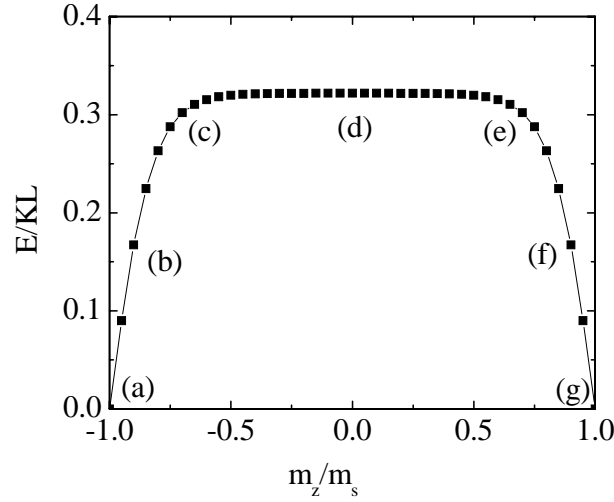


Fig. 2.3. Energy landscape $E(m_z)$ for a particle with a small exchange parameter.

Using our numerical minimization program, we calculated $E(m_z)$ of a grain with uniform magnetic anisotropy [$K(z)=6\times 10^6\text{J/m}^3$] and the result is shown in Fig. 2.3 We supposed the grain length $L=14.8\text{nm}$ and exchange stiffness constant $A=1\times 10^{-11}\text{J/m}$. It can be seen that the energy is indeed constant when m_z is far from its limiting values. The energy barrier which can be obtained from the height of $E(m_z)$ is $3.1\times 10^{-2}\text{J/m}^3$, and is in good agreement with the domain wall energy based on the thin wall approximation $3\times 10^{-2}\text{J/m}^3$. The maximum slope of $E(m_z)$ appears near the negative saturation end ($m_z=-m_s$), which corresponds to the domain wall nucleation field. The nucleation field is equal to $2K/M_s$. After the domain wall is nucleated, the $E(m_z)$ curve becomes flat (has zero slope) which means the domain wall can be pushed through the grain with an infinitesimal field. So, for a long grain with uniform K , the switching field is determined by the nucleation field, which is same as the switching field of a Stoner-Wohlfarth particle. The domain wall motion in a uniform grain will not help it switch by decreasing the switching field.

Fig. 2.4 shows the magnetization profiles (angle vs. position) for the grain whose energy landscape is shown in Fig. 2.3. Labels (a), (b), ... correspond to specific values of m_z shown in

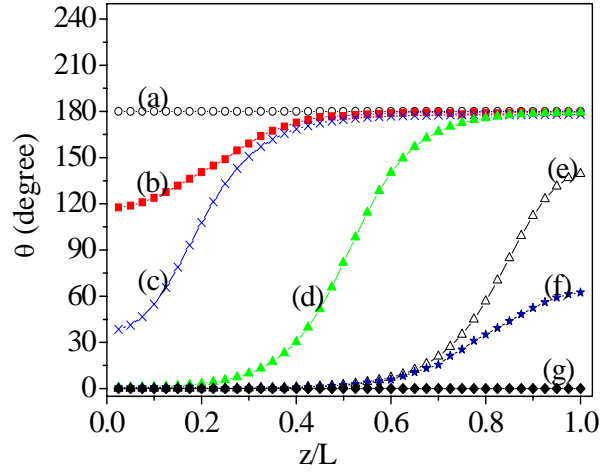


Fig. 2.4. Magnetization profiles for the particle whose energy landscape is shown in Fig. 2.3.

Fig. 2.3. From these profiles, we can see the whole switching process includes the domain wall nucleating at one end (point b), propagating (points c,d, and e) and reaching the other end (f) and completely going out of the grain (point g). The flat part of the $E(m_z)$ curve forms when the grain holds an entire domain wall, for this part, the domain wall can be pushed to either side with an infinitesimal field.

2.3 Theoretical Limit for the Figure of Merit

To solve the writability problem in magnetic recording media, we need to decrease the coercivity of the media while at the same time maintaining the thermal stability, which is determined by the energy barrier. The Victora figure of merit is an important parameter to evaluate media.

As we described above, our energy landscape $E(m_z)$ gives us both coercivity (maximum slope) and energy barrier (height of the curve) information of a one dimension system quite directly, thus we can use it conveniently in evaluating different media based on the Victora figure of merit.

Since the maximum slope of the $E(m_z)$ curve represents the coercivity and the height shows the energy barrier, if we fix the vertical height (KL) and the horizontal extent ($2m_s$), what is the minimum possible coercivity that can be obtained?

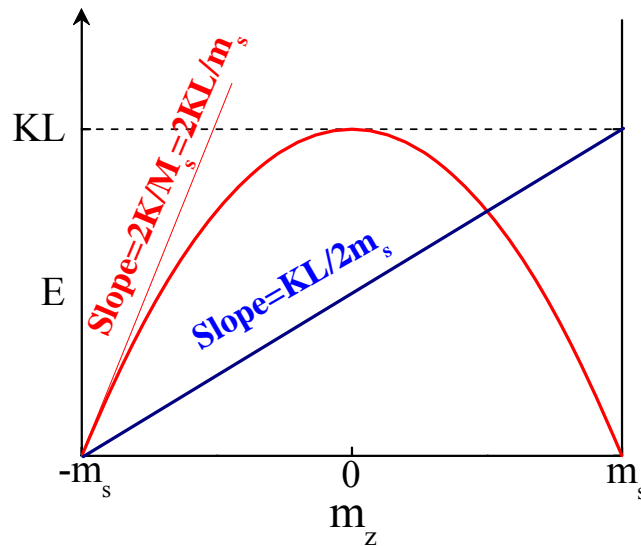


Fig. 2.5. Energy landscape for grains with the same energy barrier and moment.

Our $E(m_z)$ formation allows us to prove a completely general (within the assumptions: 1D, quasistatic) result, which is clear geometrically from the $E(m_z)$ graph shown in Fig. 2.5. With x and y fixed, the minimum slope one can get is the straight line whose slope is $H_c = KL/2m_s$. For an SW particle, if it has the same energy barrier, its coercivity will be $H_c = 2K/M_s = 2KL/m_s$ which is 4 times the minimum coercivity.

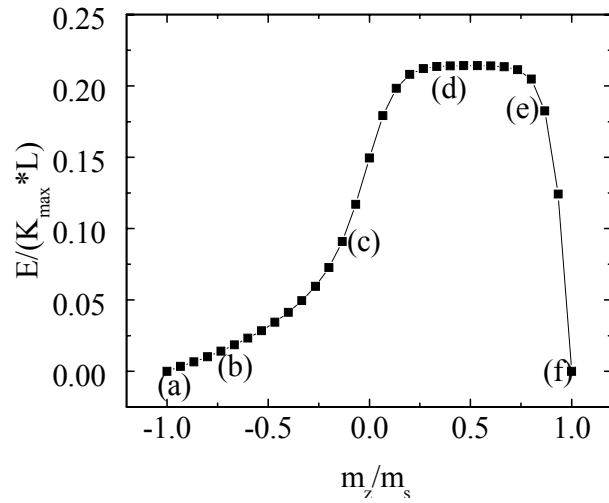
Since an SW particle with perpendicular anisotropy has figure of merit 1 when the field is applied along the easy axis, from the discussion above, the maximum figure of merit ξ is 4.

Another way of stating this result is that the coercivity of any graded medium cannot be less than $1/4$ of the coercivity of a Stoner-Wohlfarth particle of the same magnetic moment and energy barrier.

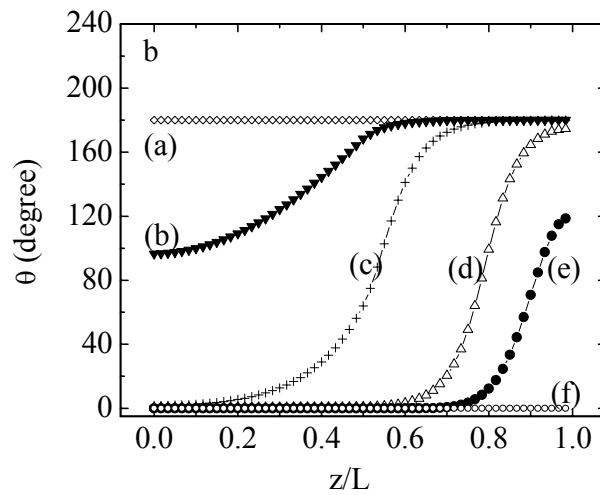
Here, we have only considered the field along the easy axis. Obviously, it is worth considering how a transverse field might be useful in switching. Since it is known that by using a field at 45° from easy axis, the switching field of a Stoner-Wohlfarth particle is decreased by a factor of 2, so the figure of merit ξ becomes 2, it is likely that the nucleation of a domain wall (which initially requires transverse twisting of the magnetization) can be assisted by a transverse field, so that the figure of merit might increase slightly above 4. However, by using LLG simulation, we find that applying a field with an angle from easy axis will not decrease the coercivity for a grain with quadratic anisotropy profile, which means the figure of merit cannot increase above 4. We will discuss this in chapter 3.

2.4 Multilayer Exchange Coupled Composite Media and Graded Media

In the past two years, exchange coupled composite (ECC) media made with a hard layer and a soft layer have been widely studied. Based on a two-spin model, ECC media has a figure of merit equal to 2. However, the two-spin model is a too rough to describe switching behavior involving domain wall motion. By using our energy minimization code, we calculate the energy landscape of an ECC medium made of a 12nm thick soft material with anisotropy equal to 0 and a 12nm thick hard material with anisotropy equal to $6 \times 10^6 \text{J/m}^3$. The soft part and the hard part each include 30 cells. The energy landscape of a grain made with two different anisotropy energies (Fig. 2.6a) shows that the maximum slope happens around the middle part of the curve and give a coercivity of 2.9 Tesla. The figure of merit of this grain is about 0.82 which is even smaller than that of a Stoner-Wohlfarth particle with a uniform perpendicular anisotropy $6 \times 10^6 \text{J/m}^3$.



(a)



(b)

Fig. 2.6. Energy landscape (a) and magnetization profiles (b) for a particle with two different anisotropy energies.

Of course, if we make the difference of these two anisotropies smaller by using harder material in the soft end, we can further decrease the coercivity. In this way, we can increase the figure of merit to a higher value. According to the angle profiles (Fig. 2.6b), maximum slope occurs where the domain wall moves through the soft/hard interface. The interface acts as a barrier and

makes the domain wall compressed and harder to propagate. We can imagine that the bigger the anisotropy difference at an interface, the harder it is for a domain wall to pass through it.

To decrease the maximum slope, we can make the anisotropy change more gradual along the thickness. To do this, we consider two anisotropy profiles. One is a discrete anisotropy profile made of four values of anisotropy with each one spanning 6 nm; the other is the linear anisotropy profile. Fig. 2.7 shows the anisotropy profiles and the corresponding energy landscapes. The energy landscape of a grain with only two values of anisotropy: $K_{soft}=0$ and $K_{hard}=6 \times 10^6 \text{ J/m}^3$ is also put into the figure for easy comparison. Compared with two anisotropy case, a grain with either of these profiles has a smaller coercivity (H_c is about 15 kOe for a 4-anisotropy profile and 16 kOe for linear profile) and almost the same energy barrier. Thus, making the anisotropy gradually change along the length can increase the figure of merit. However, this is not always true. When comparing the four-anisotropy case and the linearly continuous anisotropy case, we can see that the linear anisotropy profile has a lower energy barrier and similar coercivity. The figure of merit is about 1.5 for a grain with a linear anisotropy profile and about 1.7 for a grain with a 4-anisotropy profile. Thus, from the point of view of the figure of merit, a medium with a linear continuous anisotropy profile is not better than one with a 4-anisotropy profile even though the anisotropy changes more gradually in it.

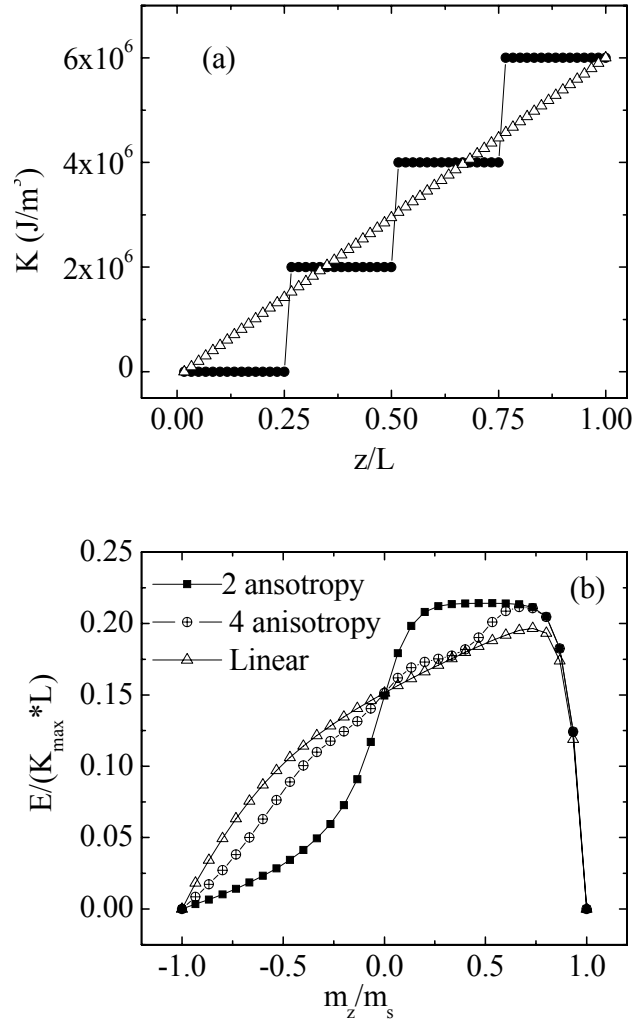


Fig. 2.7. Comparison of energy landscapes among particles with different anisotropy profiles.

Graded media with quadratic anisotropy profile

As we discussed above, for a given energy barrier and saturation moment m_s , the lowest coercivity is achieved by a landscape of constant slope. There is no general way to determine what anisotropy profile $K(z)$ will give a constant slope. However, since the domain wall thickness is of order $(A/K)^{1/2}$, for small exchange (A small), we can use a “thin wall” approximation and assume magnetic anisotropy K is constant in the wall. Thus, we can estimate

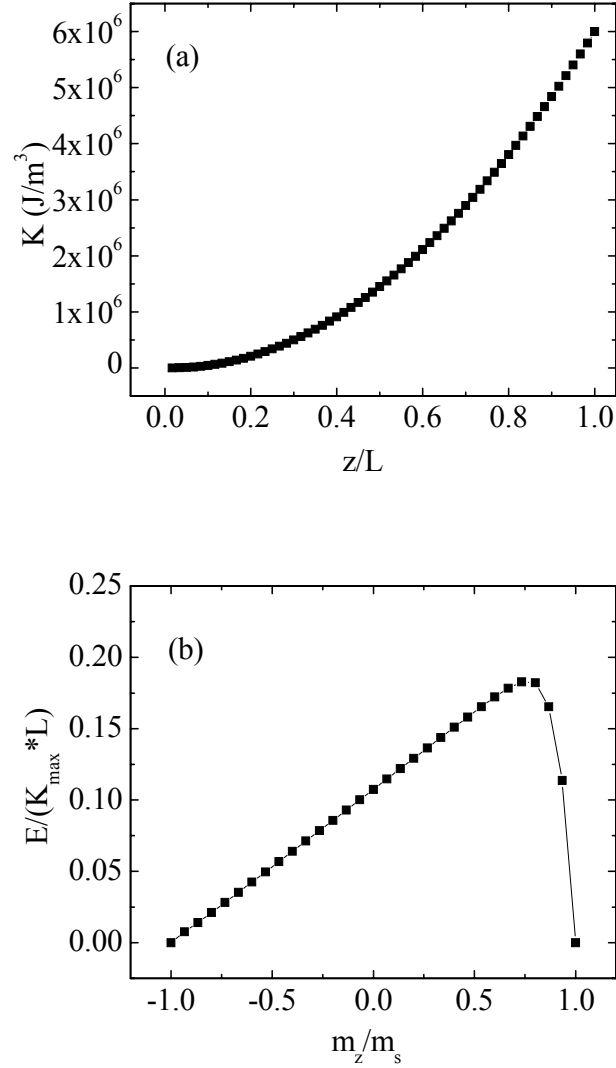


Fig. 2.8. Anisotropy profile (a) and energy landscape (b) of a particle with a quadratic anisotropy distribution.

The energy barrier by using $4(KA)^{1/2}$. In this limit, it can be shown that the constant-slope profile is $K(z) \propto z^2$.

We thus calculate numerically the energy landscape of a grain with a quadratic anisotropy profile. Fig. 2.8 shows the anisotropy profile and the energy landscape of the grain. The energy landscape is quite linear except near the positive m_s end. From the energy landscape,

we find the coercivity for this grain with a quadratic anisotropy profile is about 6.45 kOe and the figure of merit is 3.36.

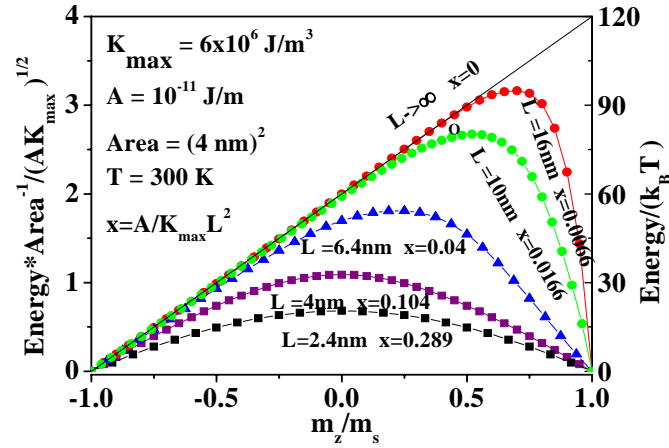


Fig. 2.9. Energy landscapes for grains with different grain lengths.

Based on the thin-wall approximation, we have proved that the linear energy landscape can be achieved for a grain with a quadratic anisotropy profile. However, the thin-wall approximation only holds for large grain length (compared to domain wall width). When the length of a grain is too small to hold a domain wall, the switching will be coherent. The switching will be domain wall switching only when the grain length is larger than domain wall width. In the “thin wall” approximation, the domain wall width ($\delta = \pi\sqrt{A/K}$) is determined by the anisotropy and the exchange stiffness. For a grain with graded anisotropy, the hardest part will give the smallest domain wall thickness ($\delta_{min} = \pi\sqrt{A/K_{max}}$). To hold a domain in a grain with graded anisotropy, the grain length L should at least be larger than the smallest domain wall width. To investigate how large the length should be for a grain with quadratic anisotropy profile to get a linear energy landscape, the energy landscapes as a function grain length are calculated and shown in Fig. 2.9 with the energies scaled by $S\sqrt{AK_{max}}$ (S is the area

of cross section of the grain). The anisotropy of the hard end is $6 \times 10^6 \text{ J/m}^3$ and leads to a small domain wall width of 4.05 nm. As we can see, when L (2.4 nm or 4 nm) is smaller than this value, the energy landscape is quite parabola like, which means that the switching takes place by coherent rotation; when L is larger than the smallest domain width, the switching occurs by domain wall nucleation. The energy landscape becomes more linear as L increases and approaches the thin-wall approximation as $L \rightarrow \infty$ (straight line). In the realistic case, to get linear energy landscape and good thermal stability ($\Delta E \geq 60k_B T$), L should be larger than 10 nm. For a given grain, the scale factor of the energy barrier is defined by $\Delta E / \sqrt{AK_{max}}$ with ΔE representing the energy barrier. In the thin-wall limit, the energy barrier should be $4S\sqrt{AK_{max}}$ and give the scale factor 4. For a grain with small L , the scale factor of the energy barrier is much smaller than 4; with the increase of L , the scale factor of the energy barrier becomes closer and closer to 4. After characterizing such a quadratic profile by its maximum anisotropy K_{max} , we noticed that except for scaling factors, the behavior of the system is completely determined by the dimensionless quantity $x = A/K_{max}L^2$, where L is the length of the grain. In terms of x , the exchange length (a measure of domain wall width) is $x^{1/2}L$. Thus $x^{1/2}$ represents the exchange length relative to the grain length. The switching is coherent in the large exchange length (large x) limit and occurs by domain wall motion for small x . As $x \rightarrow 0$, the energy approaches the thin-wall approximation. The coercivity in the thin-wall limit also scales with $x^{1/2}$: $H_c = x^{1/2}H_{k_{max}}$, where $H_{k_{max}} = 2K_{max}/M_s$ is the Stoner-Wohlfarth coercivity at the hard end. In Fig. 2.9, we show the corresponding x value for each energy landscape. In the limit of small x (infinite L), the coercivity approaches zero. For a more realistic case, such as $L=10$ nm, corresponding to an aspect ratio of 2.5, the coercivity is 15.4 kOe (achievable by conventional heads) and the thermal stability is $75K_B T$.

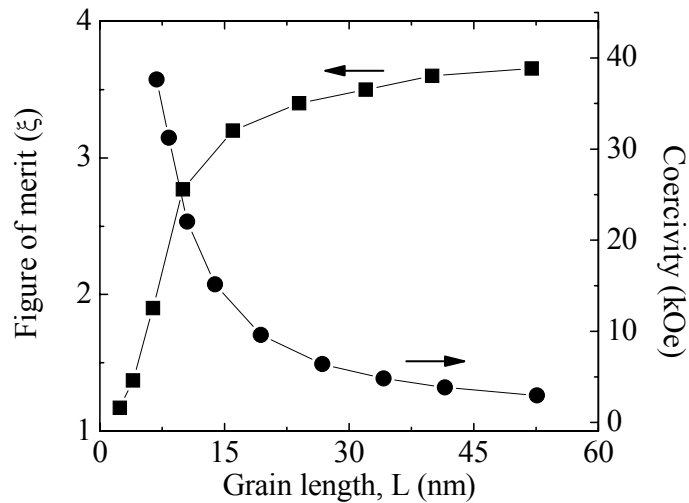


Fig. 2.10. Dependence of the figure of merit and coercivity on grain length.

The dependences of the figure of merit and coercivity on grain length L are shown in Fig. 2.10. With the increase of L , the figure of merit increases rapidly when grain length is very low and increases slowly after $L \geq 16\text{nm}$. The coercivity decreases fast with the increase of L when $L < 16\text{nm}$, and decreases slowly when $L \geq 16\text{nm}$. It is clear, as $L \rightarrow 0$, the figure of merit will reach the maximum value of 4 and the coercivity will reach the minimum value of 0. However, for a real recording medium, the thickness cannot be very large because of the decay of the head field – a reasonable thickness should be 10-20 nm. In this range, the figure of merit will be 2.7-3.3, the coercivity will be 9.6 -15.2 kOe.

Graded media with quadratic anisotropy profile and nonzero anisotropy at soft end

Until now, all the systems we considered have zero anisotropy in the soft end. In reality, we might not be able to find a series of materials with a quadratic anisotropy profile beginning from zero. What happens if the soft end has finite magnetic anisotropy?

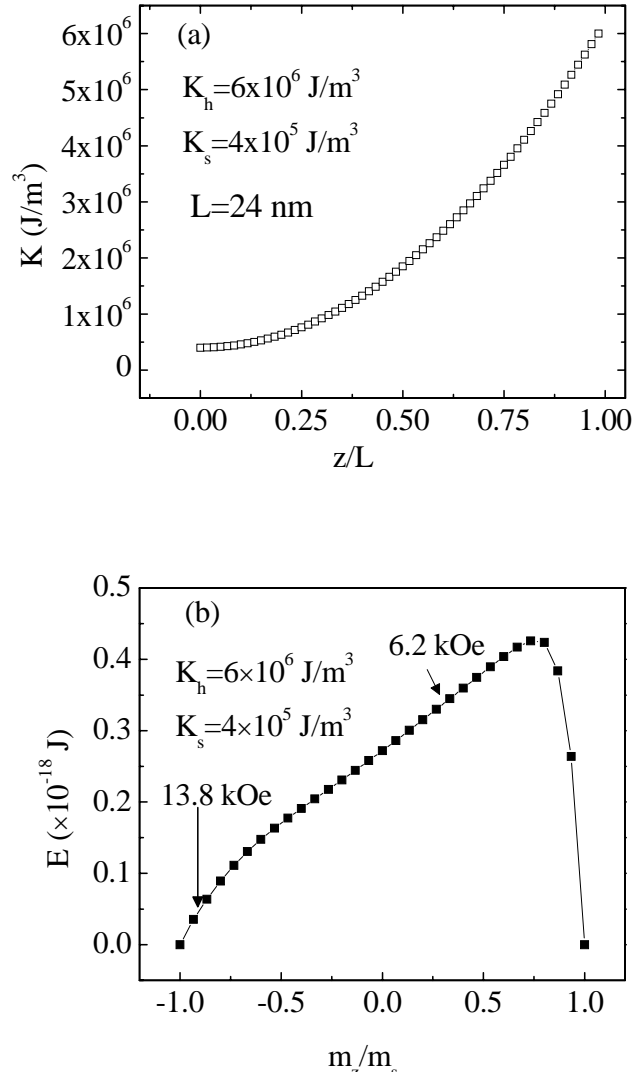


Fig. 2.11. Anisotropy profile (a) and energy landscape (b) for a grain with a finite anisotropy at the soft end.

Fig. 2.11 shows the anisotropy profile and energy landscape of a media with finite K_{soft} . The nonzero K_{soft} will make domain wall nucleation become difficult and require a larger field. The coercivity is determined by the nucleation field, which is equal to 13.8 kOe, and the figure of merit is 1.6.

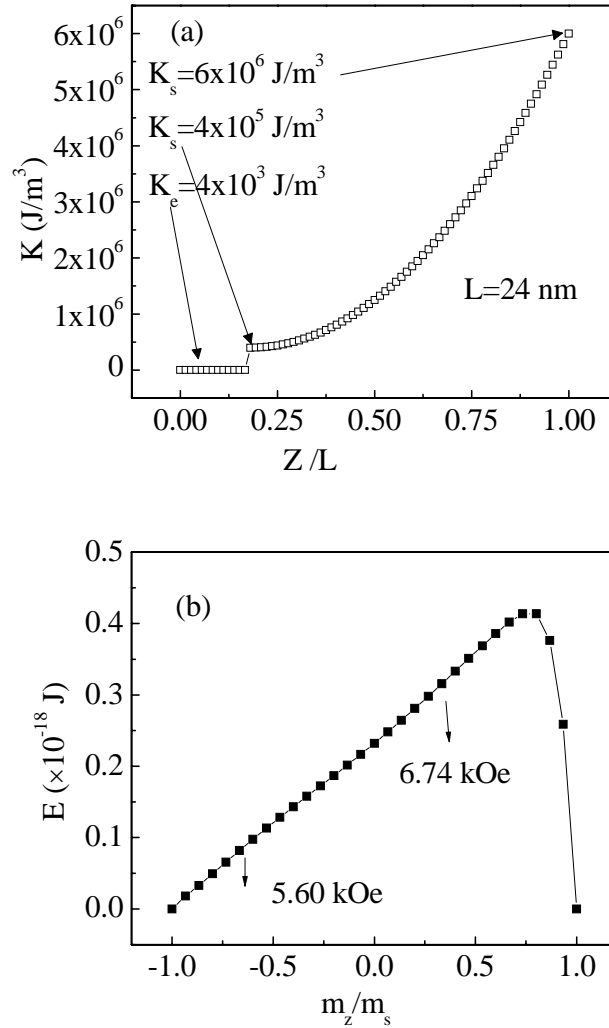


Fig. 2.12. Anisotropy profile (a) and energy landscape (b) for a grain with a soft-tail.

To decrease the nucleation field, we tried adding a soft tail made of a very soft material (small K) to the soft end. The anisotropy profile is shown in Fig 2.12. Since the domain wall is easy to nucleate in the soft tail, the soft tail can help to decrease the coercivity by decreasing the nucleation field. The energy landscape, as we can see, is very close to linear. The coercivity is about 6.74 kOe which is much smaller than without a soft tail; the figure of merit is about 3.18 which is almost 2 times that without a soft tail.

Effect of a hard tail

For switching involving domain motion, the energy barrier can be estimated by the domain wall energy at the hardest end. So, it is expected that by increasing the length of the hardest end (hard tail), one can increase the energy barrier of a magnetic grain. To confirm this

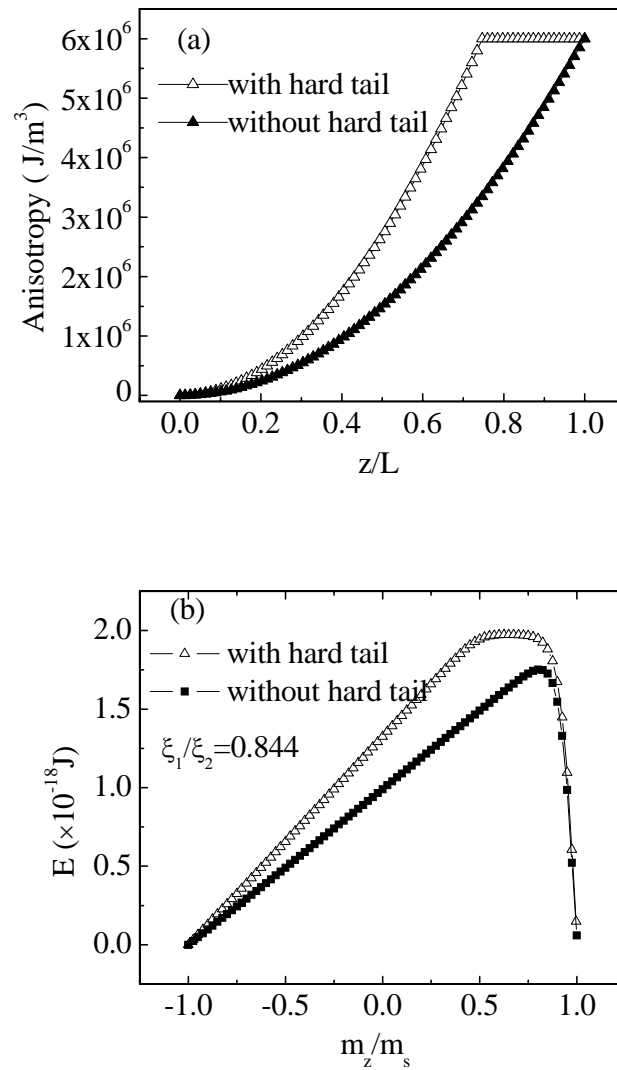


Fig. 2.13. Comparison between energy landscapes of grains with and without a hard tail.

And determine whether a hard tail can increase the figure of merit, we compare the energy landscapes of two grains with and without a hard tail. Both grains have the same soft end and

hard end as well as the same total length ($L=24\text{nm}$). The anisotropy profiles and energy landscapes of both grains are shown in Fig. 2.13. As we expect, the hard tail can increase the energy barrier. However, compared to a grain with quadratic anisotropy profile and having the same length, it has smaller figure of merit because of larger coercivity. Thus adding a hard tail to a medium quadratic anisotropy profile cannot further increase the figure of merit of the medium.

Effect of the strength of exchange

The strength of exchange coupling also affects the switching behavior of the grain. We calculate the energy landscapes for grains with different exchange stiffness constant A . The dependences of coercivity, energy barrier and figure of merit on the strength of exchange are shown in Fig. 2.14. The decrease of exchange interaction can further increase the figure of merit.

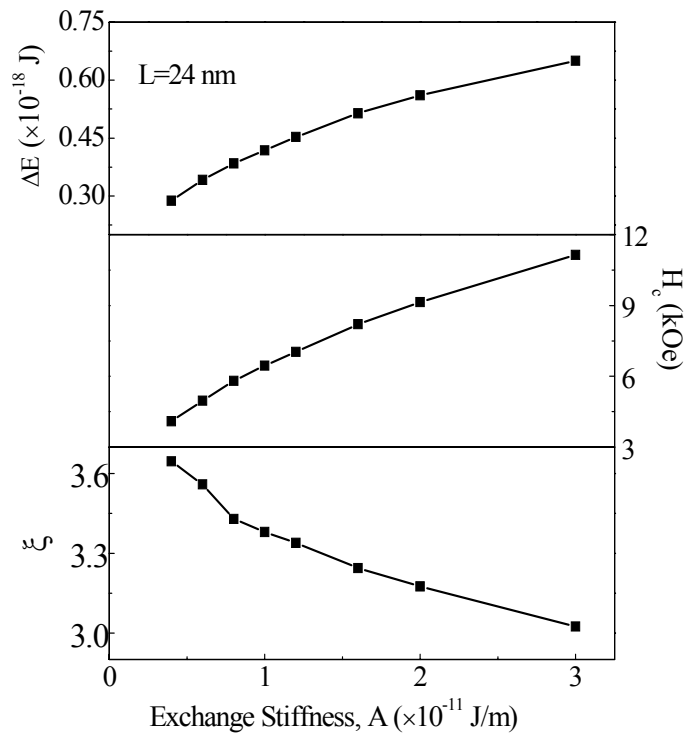


Fig. 2.14. Dependence of Energy barrier, figure of merit and coercivity on the exchange stiffness constant.

Conclusions

The energy landscape $E(m_z)$ is very convenient for studying a medium from the point of view of the figure of merit. By using this method, we have shown a theoretical limit (4) on the figure of merit of a graded medium, and that this limit can be very nearly achieved by $K(z) \propto z^2$. A soft-tail can help to decrease coercivity and increase the figure of merit for a grain with a quadratic anisotropy profile. A hard tail can increase the thermal stability, but at the same time, it also increases coercivity leading to a decrease of the figure of merit. The figure of merit can be further pushed toward the theoretical limit by decreasing the exchange in some range.

CHAPTER 3 ANISOTROPY GRADED MEDIA: MAGNETIC CHARACTERIZATION

Introduction

The Landau-Lifshitz-Gilbert (LLG) equation is an important tool for the study of the magnetic behavior of magnetic materials and devices. By using the LLG equation, one can conveniently simulate the hysteresis loops and dynamic behavior of a magnetic system. So far, I have reported the study of graded media by using a new energy landscape which is obtained by using static simulation. To better study the magnetic properties of a graded medium, it is also necessary to simulate the dynamic behavior in response to an applied field. This can be performed by using the LLG equation.

In experiment, to fabricate a medium with graded anisotropy, controlling the anisotropy of each layer is critical. To do this, a method needs to be found to evaluate the anisotropy of each layer after a medium has been fabricated.

In this chapter, the study of the magnetic properties of graded media by simulating the easy and hard axis hysteresis loops with a commercial Landau-Lifshitz-Gilbert simulator “LLGTM” [54] is reported. Meanwhile, a possible way to study the anisotropy distribution of a medium with graded anisotropy is also studied and reported. In the following sections, we follow the presentation of reference 55 [55].

3.1 LLG Simulation and Convergence

The LLG simulation [56] solves the following equation:

$$\frac{d\vec{M}}{dt} = -\frac{\gamma}{1+\alpha^2}\vec{M} \times \vec{H}_{eff} - \frac{\gamma\alpha}{1+\alpha^2}\vec{M} \times (\vec{M} \times \vec{H}_{eff}) \quad (3.1)$$

Here, M is the moment of the spin considered; H_{eff} is the effective magnetic field on each magnetic moment; γ is the electron gyromagnetic ratio which is determined by a free electron's charge-to-mass ratio and the spectroscopic splitting factor, $g=2$; α is the damping constant. In solving the LLG equation, the gyromagnetic frequency γ , the damping constant and the magnitude of the effective fields determine the time scales of interest.

The effective magnetic field on each magnetic moment is determined from the total system energy E_{tot} by [54]

$$\overrightarrow{H_{eff}} = - \frac{\partial E_{tot}}{\partial (M_s \hat{\alpha})} \quad (3.2)$$

where E_{tot} and M_s represent the total energy and saturation magnetization of the system, $\hat{\alpha}$ is the unit vector along α direction. For the energy, here we only consider uniaxial magnetocrystalline anisotropy energy, exchange energy, magnetostatic energy and Zeeman energy.

Convergence

Before we begin the calculation with the LLG code, we need to determine how large a cell we need to use. The larger the cell size, the smaller the number of cells needed to simulate a system with a certain dimension. Thus, the simulation will cost less time and require less memory. However, if the cell is too large, the results will not be reliable. To determine how large a cell we can choose to keep the simulation results reliable, it is important for us to do a convergence test.

Here, we only consider a three dimensional grain with dimension $8\text{nm} \times 8\text{nm} \times 24.4\text{nm}$ with a quadratic anisotropy profile $K \propto z^2$ and the minimum anisotropy $K_{min}=0$ and maximum anisotropy $K_{max}=6 \times 10^6 \text{ J/m}^3$. The initial state of the system is negatively saturated and a positive magnetic field with value of 12.0 kOe is applied. We simulate the switching behavior of the

same system by splitting the column length to N cells with N=11, 21, 26 and 31. All the cells have the same saturation magnetization $M_s=1000$ emu/cc. In all simulations, the damping constant is set to 1. We can thus compare the change of moment with time during switching in these four cases. For easy comparison, we shift the curves along horizontal axis so that the $m_z=0$ of each curves happens at the same time. Fig. 3.1 shows the change of moment (m_z) as a function of time in all these four cases. The $m_z(t)$ curve with a small number of cells is quite different from those with a large number of cells.

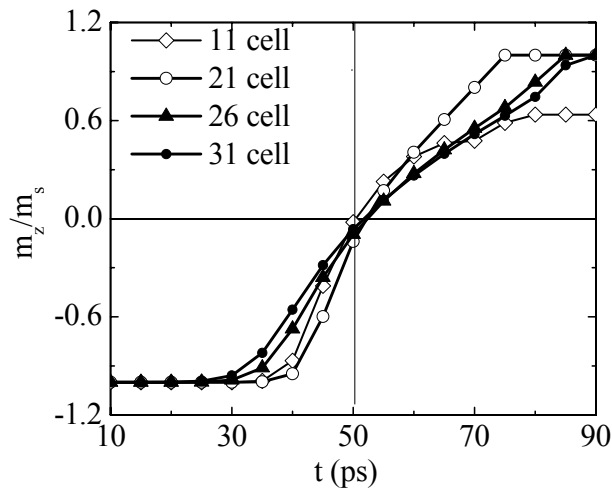


Fig. 3.1. Change of the moment (m_z) as a function of time.

When the system is split into 11 cells (each cell has length 2.22 nm), a 12.00 kOe field is not big enough to make the system switch. This result is not correct. So if we use too big cells in simulation, the results will become unreliable. With the increase of number of cells, $m_z(t)$ curves become more and more similar. The $m_z(t)$ for N=26 is quite close to that for N=31. Thus, it appears that when $N \geq 26$ (cell length 0.94 nm) the simulation will reach convergence with respect to cell size. To confirm this, we simulate easy axis hysteresis loops for N=26 and N=31. The easy axis loops are the same for these two cases as shown in Fig. 3.2. Therefore, to get reliable

simulation results in simulating a system with 24.4 nm in length, the minimum number of cells for splitting along length should be 26, which corresponds to a maximum cell length 0.94 nm.

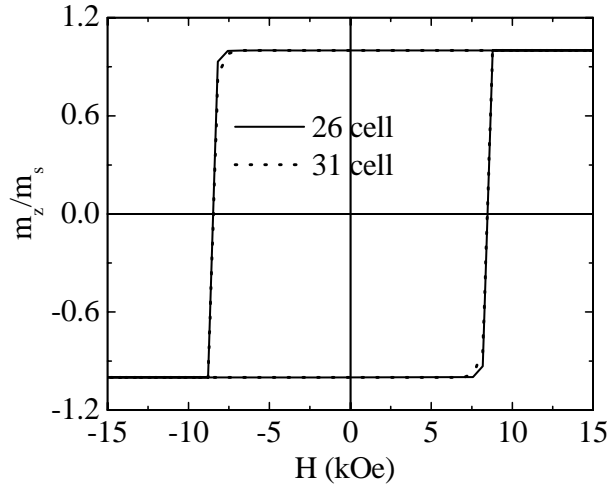


Fig. 3.2. Comparison of the simulated easy axis loops when a grain is separated into 26 cells and 31 cells.

In the following part of this section, all the grains we simulate have the same total length $L=24.8\text{nm}$ with an aspect ratio 3.1, and are divided into 31 $8\times 8\times 0.8\text{ nm}^3$ computational cells with $M_s=10^6\text{ A/m}=1000\text{ emu/cc}$ for each cell. The damping constant is set to 1.

3.2 Easy Axis Loops of Graded Media

By using the LLG method, we can simulate the easy axis loop of a magnetic material. From the easy axis loop, we can easily find the coercivity of the material. As we discussed before, by using the energy landscape, we can estimate the coercivity of a medium by the maximum slope. In our energy landscape, we did not consider the effect of magnetostatic interaction. In LLG simulation, we will take this effect into account and study how it affects the magnetic properties of the graded media.

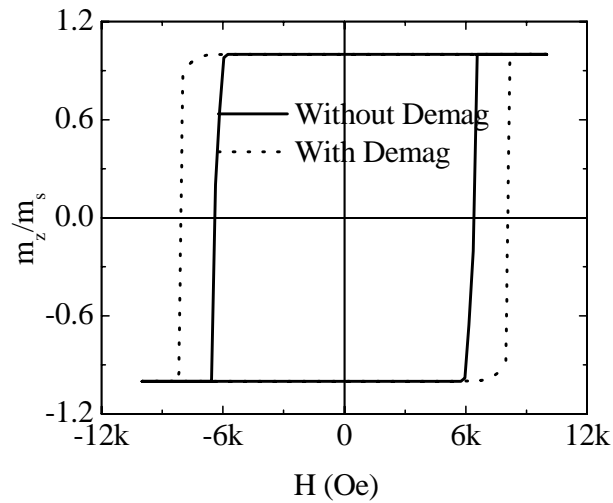


Fig. 3.3. Comparison of the simulated easy axis loops of a grain with and without the demagnetizing field being considered. The grain has a quadratic anisotropy profile.

Fig. 3.3 shows the easy axis hysteresis loops for a 24.4 nm grain with a quadratic anisotropy profile with and without the demagnetizing field being considered. The softest end has $K_{min}=0$ and the hardest end has $K_{max}=6 \times 10^6$ J/m³. Without considering the demagnetizing field, the coercivity is about 6.4 kOe, which is in very good agreement with what we got from the energy landscape ($H_c=6.46$ kOe). When taking magnetostatic effect into account, the grain becomes more difficult to switch and the coercivity increases to about 8.20 kOe. Carefully comparing the loops, we find that in both loops, the moment begins to change almost at the same field, which means the moment of the softest end begins to twist at the same field. However, with magnetostatic effect, a larger field is needed to nucleate a domain wall. Therefore, the magnetostatic effect increases the coercivity by preventing domain wall nucleation. To overcome this magnetostatic effect, a lateral field component may be helpful.

As we discussed before, when a grain has a linear anisotropy profile or has a quadratic anisotropy profile with non-zero anisotropy at the soft end, a large field is needed to nucleate a

domain wall. After the domain wall is formed, a much smaller field is enough to push the domain wall through the grain. In these two cases, the coercivity will be determined by the nucleation field. We used the LLG code to simulate the easy axis hysteresis loops of these two cases. For both cases, the hardest end has anisotropy $6 \times 10^6 \text{ J/m}^3$. For a quadratic anisotropy profile, the anisotropy of the softest end is $1.2 \times 10^6 \text{ J/m}^3$; for the linear anisotropy profile, the softest end has anisotropy equal to zero. The corresponding hysteresis loops (with and without magnetostatic interaction) are shown Fig. 3.4. Without taking the magnetostatic interaction into account, the coercivity is about 15.6 kOe for linear anisotropy profile and is about 34.0 kOe for a quadratic profile with the soft end having non-zero anisotropy. Both values are in quite good agreement with the results we obtained from the corresponding energy landscapes. The magnetostatic interaction increases the coercivity to about 16.5 kOe for a linear anisotropy profile and to about 35.0 KOe for a quadratic profile with a non-zero anisotropy at the soft end.

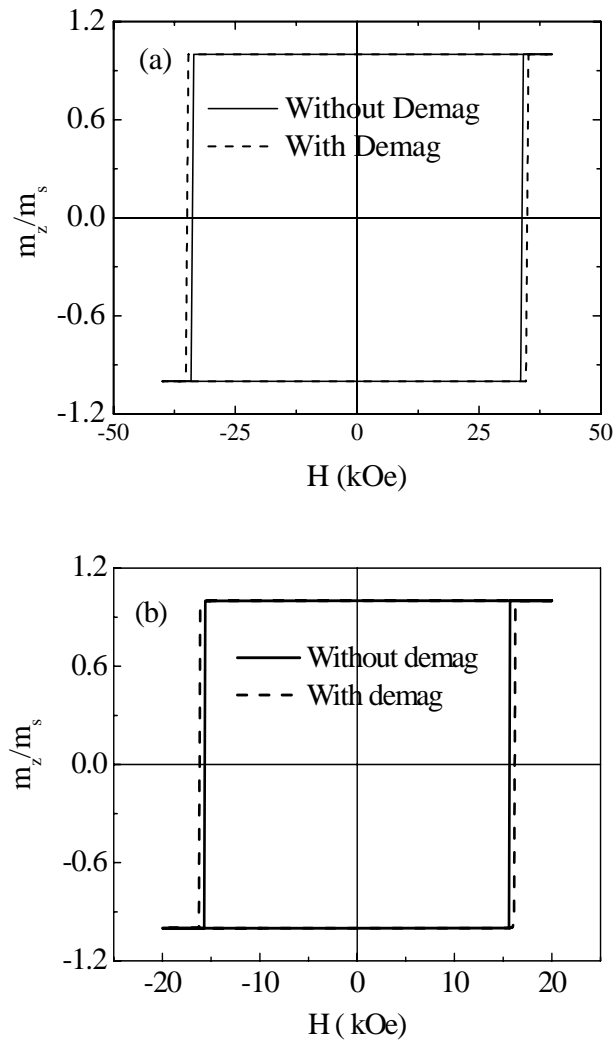


Fig. 3.4. Easy axis loops of a grain with a quadratic anisotropy profile and a nonzero anisotropy in the soft-end (a) and a grain with a linear anisotropy profile (b).

3.3 Effects of a Lateral Field

So far, we have only considered fields applied along easy axis. It is known, for Stoner-Wohlfarth particles, when the field is applied at 45° from easy axis, the switching field is decreased by a factor of 2. Obviously, it is worth considering how transverse fields might be useful in a switching involving domain wall motion.

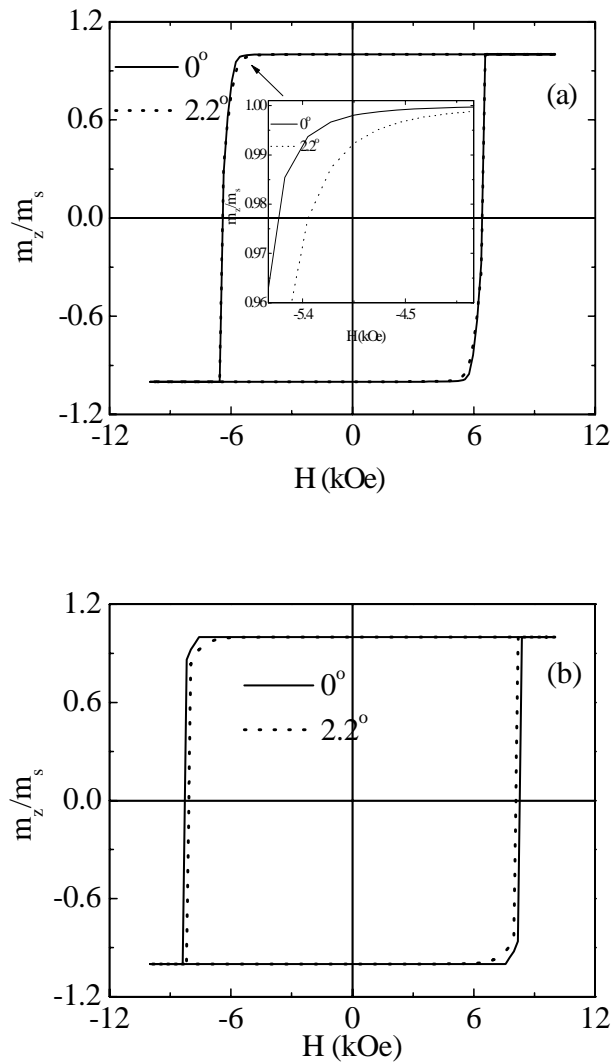


Fig. 3.5. Effect of a lateral field on the hysteresis loops of a grain with a quadratic anisotropy profile: a) Demagnetizing field not considered (the insert shows the part of curves corresponding to domain wall nucleation); b) Demagnetizing field considered.

First, we consider applying a field slightly tilted from the easy axis to a grain with a quadratic anisotropy profile. The hysteresis loops are shown in Fig. 3.5. When magnetostatic interaction is not considered, a small lateral field decreases the nucleation field (as shown in the insert) by twisting the soft end but doesn't help to decrease the coercivity. However, when magnetostatic interaction is considered, a small lateral field can slightly decrease the coercivity.

When applying a field 2.2° from the easy axis, the coercivity decreases from 8.3 kOe to about 8.0 kOe. As we have seen, the magnetostatic interaction opposes the domain formation. A small lateral field assists domain wall formation by cancelling the effect of magnetostatic interaction. To cancel the effect of magnetostatic interaction, a small lateral field (several hundred Oe) is enough. As shown in Fig. 3.6, when there is no magnetostatic interaction, increase of a lateral field will increase the coercivity. When magnetostatic interaction is considered, applying field about 5° from easy axis will give the smallest coercivity (about 7.75 kOe). At this angle, during switching the lateral field is about 500-700 Oe. Further increasing the lateral field by applying a field at larger angle will increase the coercivity.

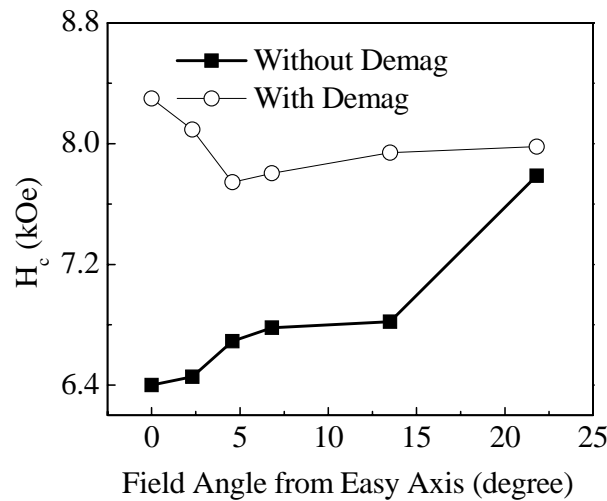


Fig. 3.6. Dependence of H_c on the applied field direction for a grain with a quadratic anisotropy profile and $K_{soft}=0$.

Now, we consider a grain with a quadratic anisotropy profile but having nonzero anisotropy in the soft end ($K_{min}=1.2 \times 10^6 \text{ J/m}^3$). As we discussed before, the coercivity of the grain is determined by the nucleation field. Here, we again consider two cases – with and without magnetostatic interaction. Since we are interested in the switching behavior of the grain, we

only simulate the part of the loop near switching. Fig. 3.7 shows the dependence of the coercivity on the field angle. The results shown in Fig. 3.7 include the effect of magnetostatic interaction. The coercivity decreases significantly with field angle and reaches a minimum value when the applied field is 45° from easy axis.

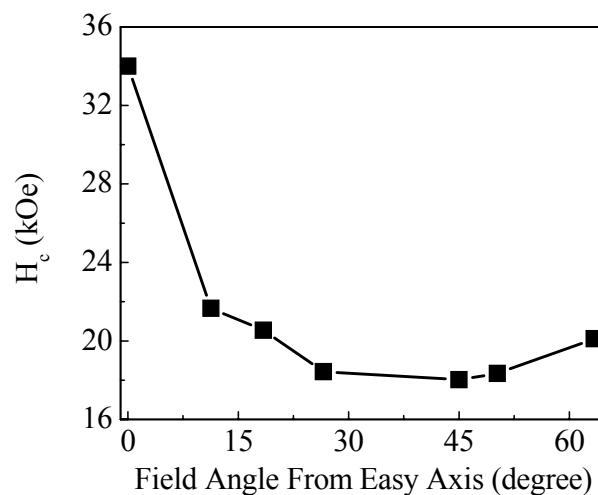


Fig. 3.7. Dependence of H_c on the applied field direction for a grain with a quadratic anisotropy profile and $K_{soft} \neq 0$.

The same thing also happens to a grain with a linear anisotropy profile. When the applied field is 45° from the easy axis, the coercivity is about 14.7 kOe when the demagnetizing field is considered and 12.2 kOe when it is not considered. This may be compared with the coercivity (16.6 kOe and 15.0 kOe, respectively) when applied field is along the easy axis. In both case, the coercivity is significantly decreased by the lateral field

In general, when the switching field is determined by the nucleation field, 45° from the easy axis is the best direction for an applied field. In this direction, the smallest field is needed to switch the moment of a grain. On the other hand, when a field required for a domain wall to nucleate is not larger than the field to keep domain wall propagating, the switching field cannot

be decreased by applying a large lateral field. In this case, a small lateral field can decrease the switching field by a small amount.

3.4 Hard Axis Loops of Graded Media and the Anisotropy Distribution Function

Although our ultimate interest is of course in the easy axis switching behavior of an anisotropy graded grain, which determines its usefulness as a recording medium, the easy axis loop is not sufficient to characterize such a grain. This is because the easy axis loop involves a sudden irreversible switching – when the field reaches the nucleation value, the rest of the energy landscape has lower slope and so the magnetization jumps immediately to positive saturation. The hard axis loop (with field perpendicular to the axis of the grain) is reversible. At low field, only the soft end twists away from the easy axis; as the field increases, the onset of twisting moves toward the hard end, which twists gradually until it is saturated in the hard direction. We know the hard axis loop exactly for a uniform Stoner-Waohlfarth particle – it is saturated for $H < -H_k$, increases linearly and is saturated again for $H > H_k$. Thus, the anisotropy field H_k is marked by a sharp bend in $M(H)$, and we can focus on it by taking two derivatives: dM/dH is piecewise constant and the d^2M/dH^2 is zero except for the delta functions at $H = \pm H_k$. If there is no exchange or magnetostatic coupling, the delta functions from different parts of the grain superimpose, so the anisotropy distribution can be extracted from the hysteresis curve [57].

Theory

Let us suppose a grain is stacked with layers with different values of magnetic anisotropy but all having an easy axis along the grain axis. If there is no exchange interaction between layers, each layer can be taken as a Stoner-Wohlfarth particle and reacts to an applied field completely independent of the other layers. Thus, the hard axis loop of the grain will be a

superposition of the hard axis loops of all the layers as shown in Fig. 3.8. In this way, we can derive the $m(H)$ of a grain analytically.

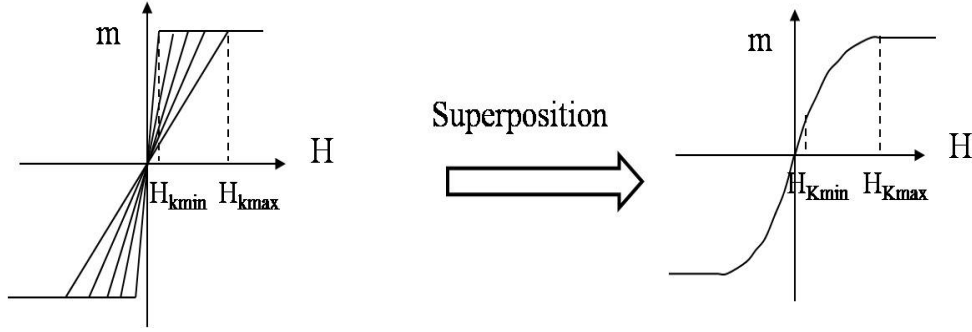


Fig. 3.8. Cartoon for deriving hard axis loop of a grain by the superposition of hard axis loops of different layers when there is no exchange interaction.

Suppose all layers have the same saturation magnetization M_s . When we apply a field along hard axis, the magnetization of a layer will be:

$$M(H, H_K) = M_s \left(\frac{H}{H_{K_i}} \right) \quad \text{for } H < H_K \quad (3.3)$$

And

$$M(H, H_K) = M_s \quad \text{for } H = H_K \quad (3.4)$$

Thus, if we define $f(H_k)$ as the distribution function of one given H_k in the whole grain, the total moment along hard axis will be:

$$\langle m(H) \rangle = \int_0^H f(H_k) dH_k + H \int_H^\infty (f(H_k)/H_k) dH_k \quad (3.5)$$

After taking the second derivative in Eq. 3.5, the distribution function of the perpendicular magnetic anisotropy can be derived from the hard axis loop [57]:

$$f(H) = -H d^2 M / dH^2 \quad (3.6)$$

By using the method described above, we can analytically calculate the distribution function for two special anisotropy profiles – linear anisotropy profile and quadratic profile.

a) For a linear anisotropy profile, $K(z) = az$, without exchange interaction, each layer of the grain will switch independently and satisfy the Stoner-Wohlfarth equation:

$$H_K = (2k_u)/M_s = 2az/M_s \quad (3.7)$$

When we apply a magnetic field $H=2az_0/M_s$, the total moment can be expressed as:

$$m_z = z_0 M_s + M_s \int_{z_0}^L (z_0/z) dz \quad (3.8)$$

After integration, and using the relation $z_0 = HM_s/2a$, we can get an analytical expression for the total moment:

$$m_z = HM_s C + HM_s C (\ln (H_{kmax}/H) - \ln C) \quad (3.9)$$

where C is a constant equal to $M_s/2a$ and H_{kmax} is the maximum H_k which corresponds to the maximum anisotropy.

Thus, we can derive the distribution function for a linear anisotropy profile as following

$$f(H_k) = -H_k \times \frac{d^2 m_z}{dH_k^2} = M_s C = \text{constant} \quad (3.10)$$

b) For a quadratic profile $K(z) \propto Bz^2$, when we apply a magnetic field $H=2B(z_0)^2/M_s$, the total moment can be expressed as

$$m_z = z_0 \times M_s + M_s \int_{z_0}^L (z_0^2/z^2) dz \quad (3.11)$$

After integration, and using

$$z_0 = \sqrt{M_s/2B} \times \sqrt{H} \quad (3.12)$$

The moment can be expressed as:

$$m_z = M_s C_1^2 H + 2M_s C_1 \sqrt{H} \quad (3.13)$$

where C_l is a constant equal to $\sqrt{M_s/2B}$. Therefore, the derived distribution function for a quadratic profile is:

$$f(H_k) = \frac{C_1}{\sqrt{H_k}} \quad (3.14)$$

In principle, by using this method, we can also derive the anisotropy distribution function for a grain with any kind of anisotropy profile. However, we should note that in this method, we suppose each layer is completely independent from others and there is no interaction among layers. In a realistic case, this cannot be true because there is an exchange interaction between adjacent layers and a magnetostatic interaction within the whole grain. How will these interactions affect the distribution function? Will the distribution function still give useful information for an anisotropy distribution when interactions are involved? To answer these questions, we need to use a numerical method.

Simulation of hard axis loops

In a real magnetic grain stacked with layers with different magnetic anisotropy, exchange interaction and magnetostatic interaction always exist. When considering these interactions, the hard axis loop of the grain will not be a simple superposition of the hard axis loops of independent layers. In this condition, it is hard to derive an analytical expression of total moment as a function of applied field $m(H)$. We thus numerically simulate the hard axis loop of a grain by using the commercial Landau-Lifshitz-Gilbert simulator “LLGTM,” because it allows one to automatically sweep out a hysteresis loop.

Still, we only consider two magnetic anisotropy profiles:

- 1) The linear profile $K(z) \propto z$
- 2) The quadratic profile $K(z) \propto z^2$

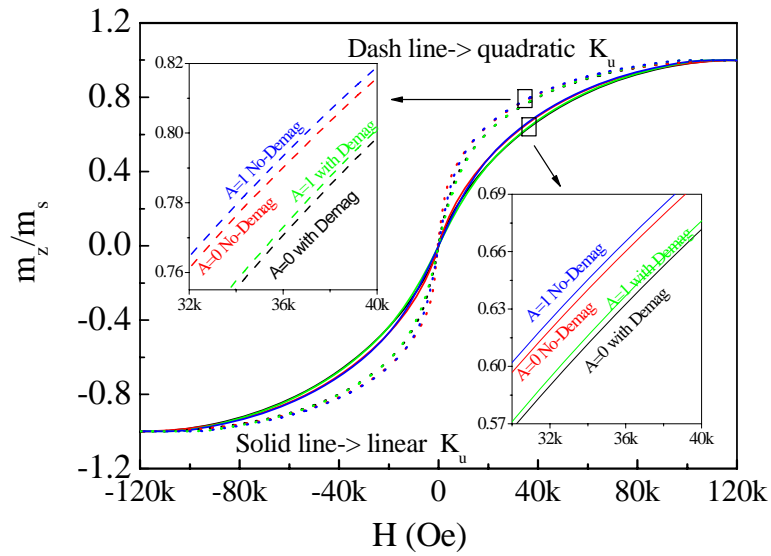


Fig. 3.9. Hard axis loops for grains with a quadratic anisotropy profile or a linear anisotropy profile.

Hard axis loops for both anisotropy profiles are shown in Fig. 3.9. It seems that the hard axis loop mainly depends on the anisotropy profile. Magnetic exchange and magnetostatic interactions have small effect on the hard axis loop. When studying carefully the high field end of the loops, we can see that without magnetostatic and exchange interactions, the maximum switching field is 120 kOe which is exactly equal to the H_k of the hardest end. Magnetostatic interactions decrease the maximum switching field H_{kmax} of the grain by a small amount. The exchange interaction decreases H_{kmax} much more apparently.

When comparing the saturated ends of loops of both anisotropy profiles, with exchange and magnetostatic interaction, the grain with quadratic profile has smaller H_{kmax} , which means that the quadratic profile is more effective in decreasing the switching field of the grain. In a realistic case, when using the same material in the hard end ($K_{max} = \text{constant}$), by comparing the

H_{kmax} of media with different unknown anisotropy profiles, one can decide which is the best anisotropy profile for decreasing switching field.

Anisotropy distribution function

When calculating the anisotropy distribution function, we cannot directly calculate the derivatives from our numerical data by a simple finite-difference scheme because small fluctuations or errors in the $M(H)$ data produce a very large amount of noise in the first and second derivatives. A method that simultaneously smoothes and differentiates the data is the Savitzky-Golay method [58], in which we fit the data locally (two points on each side of each data point, with a field interval $\Delta H = 1200 \text{ Oe}$) to a quadratic, whose curvature gives the required second derivative. We have found this method to work better than trying to find a global fit to the data. Thus, all the anisotropy distributions will be calculated by this method.

The anisotropy distributions evaluated from hard axis loops of a grain with linear anisotropy profile are shown in Fig. 3.10. For easy comparison, the analytical distribution function for the same anisotropy is also shown in Fig. 3.10 (dash line). When there are no exchange and magnetostatic interactions, as we discussed before, for a continuum system (the anisotropy changes continuously) for a linear anisotropy profile, the anisotropy distribution function should be a constant. By using Eq. 3.10, we can calculate the constant. The constant is about $0.78 \times 10^{-5} \text{ emu}^2/\text{Oe}$. However, in our simulation, the system is discrete. Therefore, without any interaction, all computational cells should switch independently and thus gives a series of delta functions in Eq. 3.6. These are seen in Fig. 3.10. Except for this discretization artifact, the distribution function exactly oscillates around a constant about $0.78 \times 10^{-5} \text{ emu}^2/\text{Oe}$, which is the same value we obtained by the analytical method.

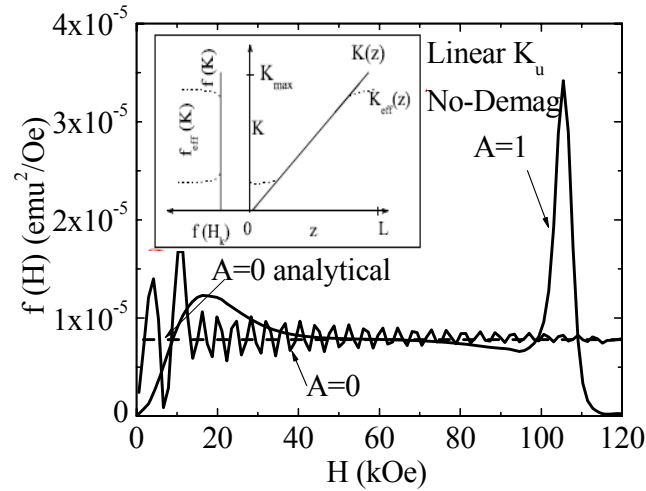


Fig. 3.10. Effect of the exchange interaction on the anisotropy distribution function of a grain with a linear anisotropy profile.

It can be seen that the magnetic exchange interaction couples the cells strongly enough to eliminate this discretization artifact. The exchange interaction also produces peaks in the extracted distribution function at both the highest and lowest anisotropy. This can be understood qualitatively in term of an effective coarse-grained anisotropy profile (inset) K_{eff} (average over an exchange length). The anisotropy does not change near the center because the values both above and below K are averaged in. Near the hard end, all or most of the values are below K , so K_{eff} becomes smaller than K . On the other hand, the situation near the soft end is the opposite – all or most values are above K , thus the K_{eff} becomes larger than K .

The effect of the magnetostatic field is shown in Fig. 3.11. The main effect is to increase the height of the peak at high H_k and decrease the peak at low H_k .

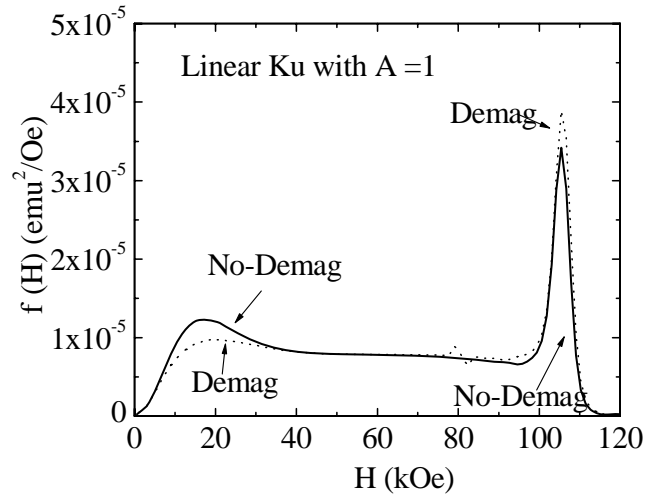


Fig. 3.11. Effect of the demagnetizing field on the anisotropy distribution function.

For a grain with quadratic anisotropy profile $K(z) \propto z^2$, when there is no exchange or magnetostatic interaction, the distribution function is proportional to $1/\sqrt{H}$ as we derived analytically before (Eq. 3.14). We can also extract the anisotropy from the hard axis loop obtained by a numerical simulation. Fig. 3.12 shows the comparison of anisotropy distributions obtained by analytical and numerical methods. These two results are in good agreement except for the oscillations caused by the discretization and the peak near $H=0$. As $H \rightarrow 0$, the distribution function diverges and the simulation results become unreliable in this region.

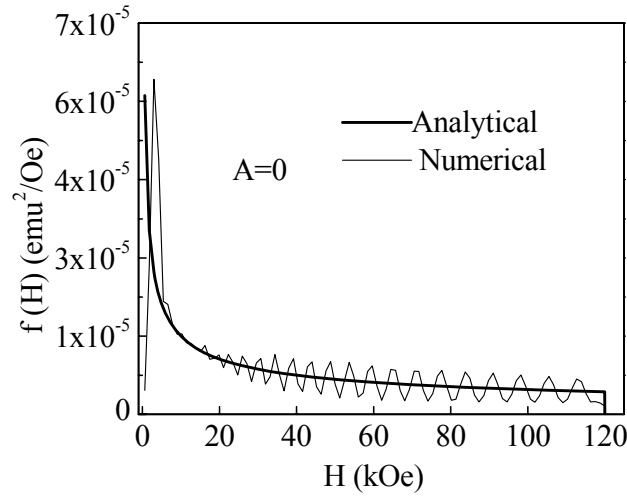


Fig. 3.12. Comparison of anisotropy distribution functions derived by analytical method and numerical method for a grain with a quadratic anisotropy profile.

Fig. 3.13 shows the extracted anisotropy distribution for the case of a quadratic profile when exchange and magnetostatic interactions are considered. The figure shows that magnetostatic interactions can also couple cells strongly enough to eliminate the discretization artifact. Even with magnetostatic interactions and non-zero exchange, the divergence of the distribution function is qualitatively preserved. In addition, the effect of exchange is similar to that for a linear profile: increasing exchange raises the high- H_k peak and shifts it inward. It has a similar effect on the low- H_k peak, although this is entangled with the effect of the $H^{1/2}$ singularity.

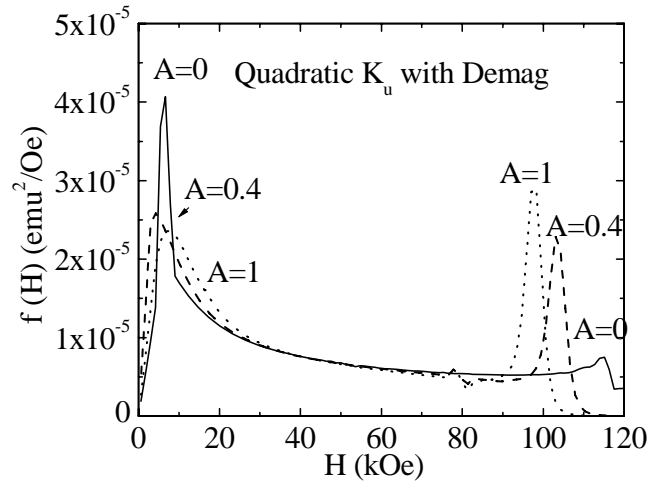


Fig. 3.13. Effect of the strength of the exchange interaction on the anisotropy distribution function of a grain profile when the demagnetizing field is considered.

In a grain with a quadratic anisotropy profile, the magnetostatic field has a significant effect at the soft end (Fig. 3.14): the peak at low H_k (10-15 kOe) is decreased; and in the same time, the distribution function at higher H_k (15-60 kOe) increases. The magnetostatic field does not affect the hard end much.

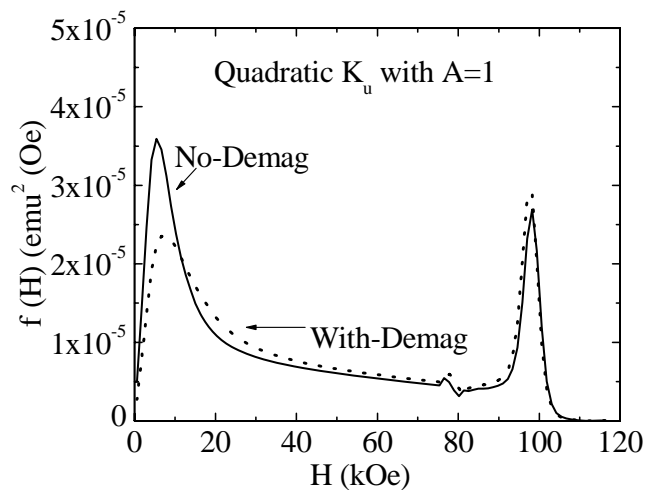


Fig. 3.14. Effect of the demagnetizing field on the distribution function.

Conclusions

Without considering magnetostatic interaction, the coercivity of a grain obtained by LLG simulation is in very good agreement with what is estimated from the energy landscape. Magnetostatic interaction will increase coercivity. Applying a field at 45° from the easy axis will decrease the coercivity of a graded medium with a soft end having nonzero anisotropy. It is possible to determine the anisotropy distribution of an anisotropy graded medium by analyzing its hard axis loop.

CHAPTER 4 FIRST PRINCIPLES STUDY OF MAGNETIC AND ELECTRONIC STRUCTURES OF $L1_0$ MPt (M=Fe AND Mn)

Introduction

In recent years, FePt and MnPt have been widely studied. The ferromagnet, FePt, is a promising medium material for high density recording because its high magnetocrystalline anisotropy (MCA) (7×10^6 J/m³) suppresses superparamagnetism [59]. The antiferromagnet, MnPt, is important both to the magnetic recording industry and for other spintronic applications such as magnetic random access memory because it can be used as a pinning layer in giant magnetoresistive (GMR) and tunneling magnetoresistive (TMR) devices [60, 61].

Both FePt and MnPt have the layered CuAu-type ($L1_0$ phase) crystal structure. This crystal structure can be visualized as the usual cubic (4-atom) fcc unit cell, but with one species occupying the sites at the corners and the top and bottom face centers of the cube with the other species occupying the layer consisting of the remaining 4 face center sites. This leads to a layered structure in which layers of one species alternate with layers of the other species along the [001] direction. $L1_0$ phases typically show a small tetragonal distortion from cubic with the c lattice constant along [001] being different from the a [100] and b [010] lattice constants.

At room temperature, the ground state of ordered MnPt is antiferromagnetic with antiferromagnetic coupling between adjacent Mn atoms in the (001) plane at distance $a/\sqrt{2}$, and ferromagnetic coupling between two adjacent Mn atoms in the (100) plane at distance c [62, 63]. However, in quenched MnPt samples [64] in which Mn and Pt atoms are only partially ordered, and sputtered disordered samples [65], ferromagnetic phases were found.

Most previous studies of MnPt have been experimental and have mainly focused on the phenomenon of exchange bias in which a MnPt layer is used to shift the hysteresis curve of an adjacent ferromagnetic layer. To our knowledge, a theoretical study of the magnetic properties of MnPt and of possible phase competition in MnPt is still lacking.

Experimentally, FePt is well known to be ferromagnetic at room temperature with a very large perpendicular (to the atomic planes of Pt and Fe) anisotropy energy. However, G. Brown *et al.* claim, based on an extensive series of calculations, that there is a competition between ferromagnetism and antiferromagnetism in FePt and that ferromagnetism is observed in experiment only because of imperfect long-range ordering in experimental samples [66].

Since FePt and MnPt both have $L1_0$ structures, the only chemical difference between them is that Fe atoms have one more electron than Mn atoms. However, FePt has a ferromagnetic ground state while MnPt has an antiferromagnetic ground state. Studying and comparing the magnetic and electronic properties of different phases of MnPt and FePt may help us understand the reasons behind their very different magnetic properties. In this chapter, we report a systematic study of the magnetic and electronic properties of FePt and MnPt with three different spin configurations.

4.1 Calculation Method

We only consider fully ordered equiatomic MnPt and FePt. Three kinds of moment configurations (as shown in Fig. 4.1) are considered: 1) An antiferromagnetic phase with antiferromagnetic configuration along the [100] direction and ferromagnetic configuration along the [001] direction; 2) An antiferromagnetic phase with antiferromagnetic configuration along the [001] direction and ferromagnetic configuration along the [100] direction; 3) A ferromagnetic

configuration along all directions (Ferromagnetic phase). In all cases, the arrows indicate only the relative direction of moments.

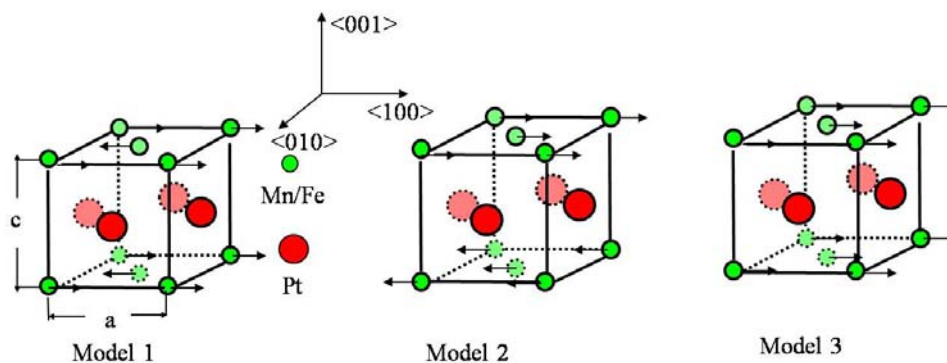


Fig. 4.1. Models considered.

Since these three models have different symmetry, their primitive unit cells are different. However, in order to compare the energies of the models more precisely, it is better to use the same unit cell for all three models. In our calculations, we used unit cells with 4 Fe or Mn atoms and 4 Pt atoms as shown in Fig. 4.2 for all three models for the purpose of energy comparison among the models.

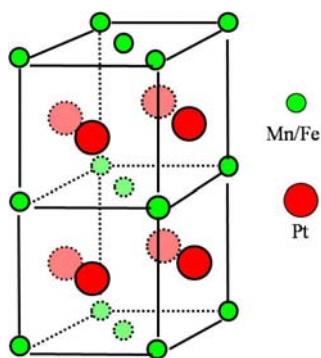


Fig. 4.2. Unit cell for energy comparison between structures.

In calculations of anisotropy and band structure, on the other hand, we used unit cells containing 2 Mn or Fe atoms and 2 Pt atoms for model 1 (Fig. 4.3 (b)) and model 2 (Fig. 4.3 (c)). For model 3, we used the formula unit cell which has 1 Mn or Fe atom and 1 Pt atom as shown

in Fig. 4.3 (a). In this Chapter, no matter what kind of unit cells was used in the calculation, the final energies were converted so that they were with respect to energy per formula unit with units eV/f.u..

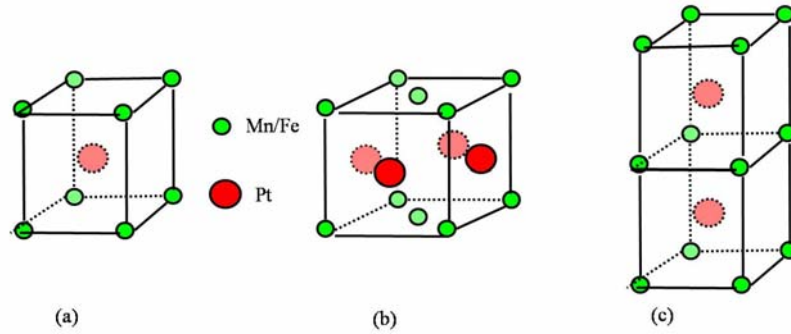


Fig. 4.3. Formula unit cell of $L1_0$ structure and unit cell used in MCA calculations for model 3, (a); unit cell used in MCA calculations for model 1, (b) ; unit cell used in MCA calculations for model 2, (c).

In all of the calculations, density functional theory (DFT) with the generalized gradient approximation (GGA) for the exchange correlation functional was used. Our calculations were based on the VASP code [67].

Convergence

In evaluating small energy differences between atomic configurations and (typically) even smaller differences between magnetic configurations, it is important to use enough k-points to sample the Brillouin Zone with sufficient accuracy and to verify the sufficiency of the k-point sampling. Fig. 4.4 shows the convergence of the energy difference between different phases for FePt and MnPt. For MnPt, since the energy difference between the three different models, is on the order of 0.1eV/f.u. or higher, 1000-2000 k-points in the full Brillouin zone are sufficient for energy comparison. For FePt, however, the energy difference between the ferromagnetic phase

(model 3) and the antiferromagnetic phase (model 2) is unusually small. According to our results, 2000 k-points are enough for energy comparison.

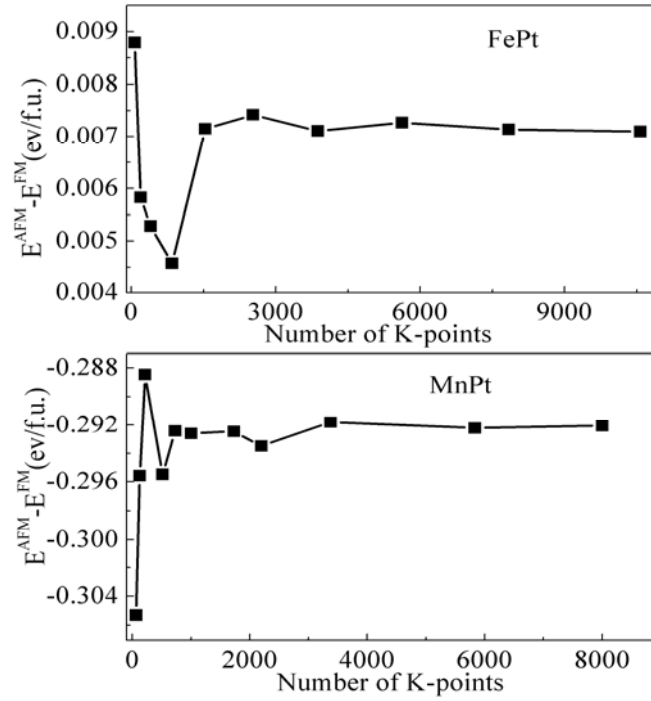


Fig. 4.4. Convergence of the AFM-FM energy difference for FePt and MnPt.

Typical changes of energy with magnetization direction, are much smaller however, often being on the order of 10^{-6} eV. Therefore, a much larger number of k-points is needed to make the energy difference converge to the required accuracy. Fig. 4.5 shows the convergence of the magnetocrystalline anisotropy energy (MCA) of MnPt and FePt in their ground state phases as a function of k-point sampling. According to our test, 5000-10000 k-points are needed to calculate the MCA energy of MnPt and more than 3000 k-points are needed for FePt. We also performed tests on the convergence of the MCA of other phases of MnPt and FePt, and found 5000-10000 k-points are enough for the three models of MnPt and 3000 k-points are sufficient for FePt.

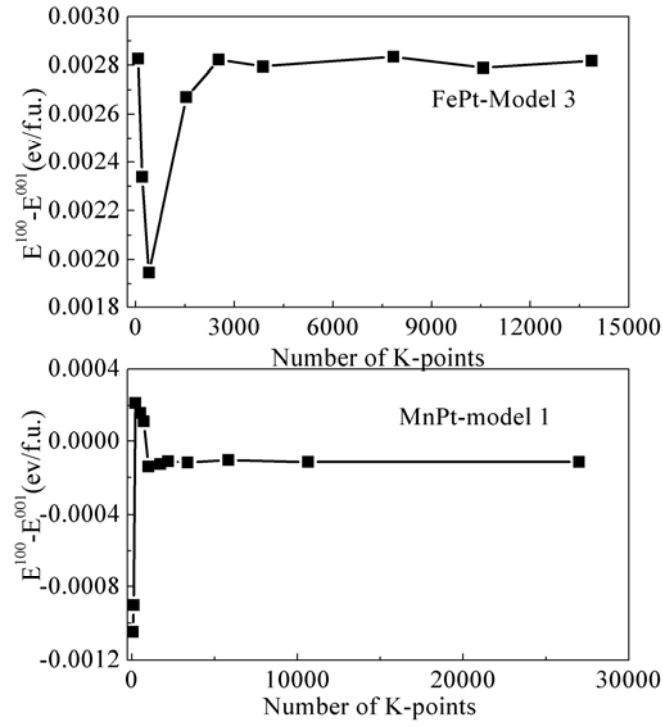


Fig. 4.5. Convergence of MCA of FePt and MnPt.

4.2 Ground State of FePt and MnPt

For each structure, to find the equilibrium state, in our calculation, we totally relaxed the system (moment, ion position, shape and volume of unit cell). In these calculations, we did not consider spin-orbit coupling. The equilibrium state parameters for each structure are shown in Table 4.1.

Table 4.1. Calculated and experimental lattice constants, magnetic moments and relative energies of the three possible magnetic structures (shown in Fig. 4.1) of MnPt and FePt (energies are given relative to the most stable phases).

	FePt				MnPt			
	Model 1	Model 2	Model 3	Exp. ⁵⁶	Model 1	Model 2	Model 3	Exp.
a (Å)	3.96	3.897	3.848	3.847	3.987	4.095	4.166	3.97
c (Å)	3.596	3.664	3.771	3.715	3.70	3.576	3.48	3.66
c/a	0.908	0.94	0.98	0.966	0.928	0.873	0.835	0.92
$\mu_{\text{Mn or Fe}}$ (μ_{B})	2.835	2.937	2.917	2.85	3.798	3.885	3.935	4 \pm 0.4
μ_{Pt} (μ_{B})	0	0	0.332		0	0	0.389	
E(ev/f.u)	0.2762	0.00716	0		0	0.2751	0.330	

In the completely relaxed state, model 3 has the lowest calculated total energy for FePt and model 1 has lowest calculated energy for MnPt. Both results are in agreement with experimental observation. The lattice constants for FePt (model 3) and MnPt (model 1) are also in good agreement with the corresponding experimental values. For both MnPt and FePt, in model 3, the Pt atoms have a small moment; while in model 1 and model 2, Pt atoms do not have a moment.

4.3 Magnetocrystalline Anisotropy (MCA)

When studying the magnetocrystalline anisotropy, we consider three cases as shown in Fig. 4.6. The first has moments along the [001] direction, the second has moments along [100] and the third case has moments along the [110] direction.

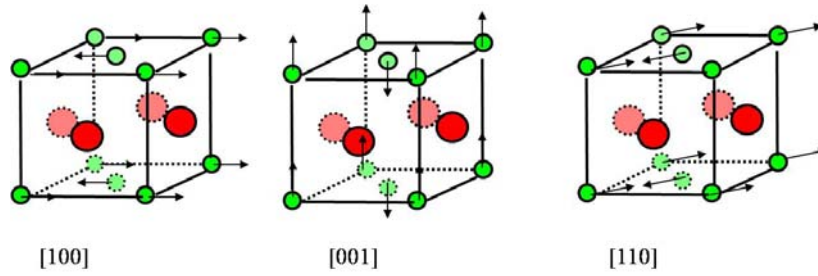


Fig. 4.6. Moment configurations.

Magnetocrystalline anisotropy of FePt

Table 4.2 shows the energies and moments in each model of FePt. We define the magnetocrystalline anisotropy energy to be the energy difference between systems with moments in the [001] and [100] directions ($\Delta E = E^{001} - E^{100}$).

Model 1 has strong out of plane anisotropy with a MCA energy of approximately 2.46 meV/f.u.

Table 4.2. Energies (relative to [100]) and atomic magnetic moments of FePt.

	Model 1			Model 2			Model 3		
	[001]	[100]	[110]	[001]	[100]	[110]	[001]	[100]	[110]
E (ev/f.u.)	-2.46×10^{-3}	0	-6.55×10^{-4}	2.8×10^{-4}	0	3×10^{-6}	-2.9×10^{-3}	0	9×10^{-5}
μ_{Fe} (μ_B)	2.817	2.815	2.814	2.935	2.937	2.934	2.912	2.915	2.913
μ_{Pt} (μ_B)	0.00	0.00	0.00	0.00	0.00	0.00	0.337	0.337	0.336

For model 2, the moments tend to lie in the (100) plane with a MCA energy about 0.28 meV/f.u. For Model 3, FePt has strong out of plane anisotropy with a MCA energy about 2.9 meV/f.u. The calculated MCA energy of the ferromagnetic phase of FePt is in very good agreement with that reported by P. Ravindran *et al.* [68].

As for the anisotropy in the (001) plane, model 1 prefers the [110] direction over the [100] direction with an in-plane anisotropy energy of about 0.65 meV/f.u and model 3 prefers the

[100] direction over the [110] direction with in-plane anisotropy energy of approximately 0.09meV. For model 2, the calculated energy difference between [100] and [110] directions is too small ($3\mu\text{eV/f.u.}$) to provide a reliable value.

Magnetocrystalline anisotropy of MnPt

The energies and moment for each atom in the three models of MnPt are shown in Table 4.3. For model 1 and model 3, the energy differences for moments along [100] and [110] are very small ($<0.01\text{meV}$). Our calculations probably do not have sufficient accuracy to resolve such a small difference, so it is difficult for us to determine which direction is preferred. For model 2, the in-plane anisotropy energy is about 0.02meV/f.u. and the preferred direction is [100]. This energy difference is also small and near the limits of our accuracy.

Table 4.3. Energies (relative to [100]) and atomic magnetic moments of MnPt.

	Model 1			Model 2			Model 3		
	[001]	[100]	[110]	[001]	[100]	[110]	[001]	[100]	[110]
E (ev/f.u.)	1.14×10^{-4}	0	1×10^{-6}	2.5×10^{-4}	0	1.93×10^{-5}	-2.35×10^{-3}	0	5×10^{-6}
μ_{Mn} (μ_B)	3.778	3.778	3.778	3.885	3.885	3.885	3.935	3.935	3.935
μ_{Pt} (μ_B)	0.00	0.00	0.00	0	0	0	0.389	0.389	0.389

Our calculations predict that model 1 has in-plane anisotropy. This result is in good agreement with results of C. S. Severin *et al.* from neutron diffraction [65]. The MCA energy of model 1 is small, about 0.114 meV/f.u. Model 2 also has its easy axis in the (100) plane but with a larger anisotropy. Model 3 has very large out of plane anisotropy and its moment prefers to be perpendicular to the (001) plane. According to our results, the Pt atom has no moment in model 1 and model 2.

4.4 Electronic Structure – Density of States

The spin-polarized total densities of states (TDOS) for FePt and MnPt are shown in Fig. 4.7. An obvious characteristic of the DOS of model 1 of both FePt and MnPt is an extremely deep minimum in the DOS near the Fermi energy. For FePt, the minimum is below the Fermi energy, while, for MnPt, the minimum is right at Fermi energy.

For model 2, the TDOS curves for both FePt and MnPt also have minima near the Fermi energy. However, the minima are not as deep as in model 1.

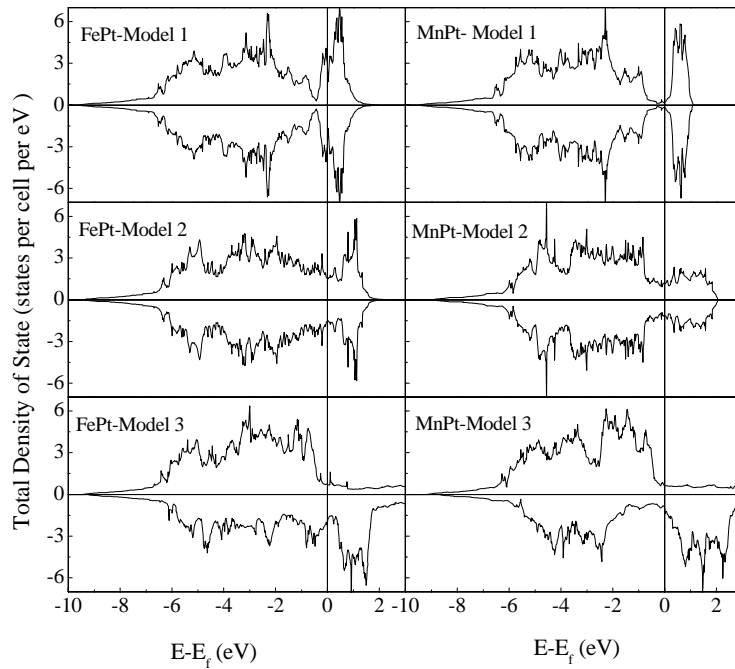
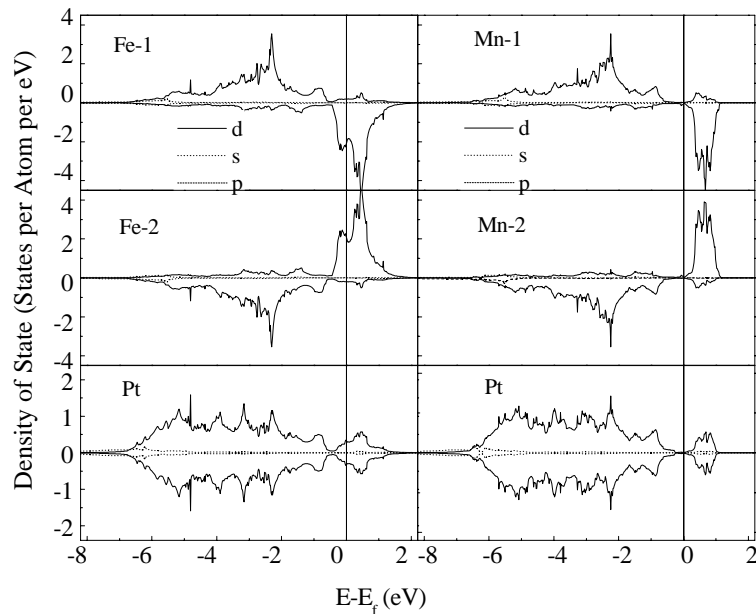


Fig. 4.7. Total densities of states for the three considered structures of FePt and MnPt.

Model 3 is the ferromagnetic phase. A characteristic of ferromagnetic phases in transition metal alloys is that the majority band is narrower than the minority band due to magnetic exchange splitting. The TDOS of model 3 of FePt and MnPt shows that the majority d-band is almost completely occupied while there are still some empty d-states in the minority band.

The TDOS of FePt and MnPt are similar for all three models. However, the Fe atom has one more electron than the Mn atom and this difference is reflected in the location of the Fermi energy.

In order to understand the role of hybridization between Fe/Mn and Pt atoms in the electronic structure of all three models, we also calculate the angular momentum projected densities of states (PDOS) of each atom for all three models shown in Fig. 4.8. Comparing with the TDOS shown above, we find that the valence band consists mainly of d states with only tiny contributions from s and p. In all three models of both FePt and MnPt, the majority of the density of states of d band (d-DOS) of Fe/Mn and d-DOS of Pt are quite broad and energetically degenerate over the entire valence-band range, which indicates a strong hybridization between the 3d states of Fe/Mn and the 5d states of Pt. Comparing the PDOS with the TDOS, we find that the TDOS near the Fermi energy comes mainly from the 3d states of Fe/Mn,



Model 1

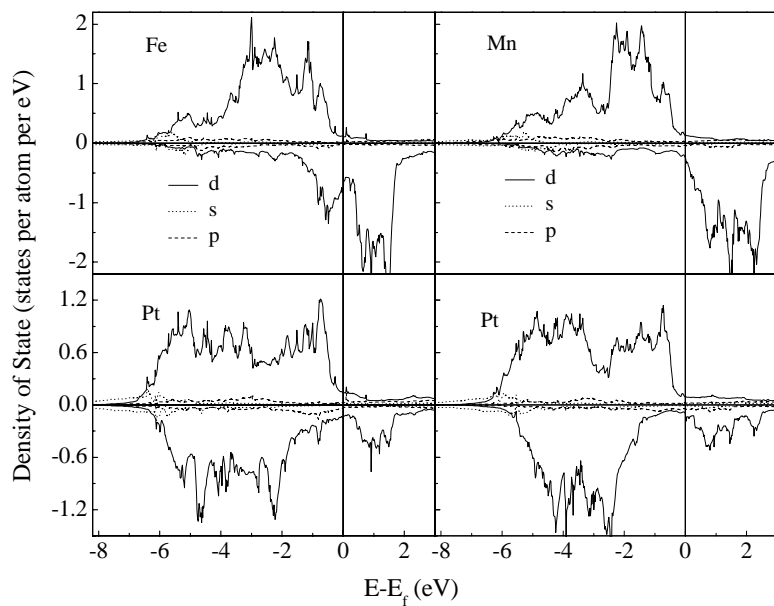
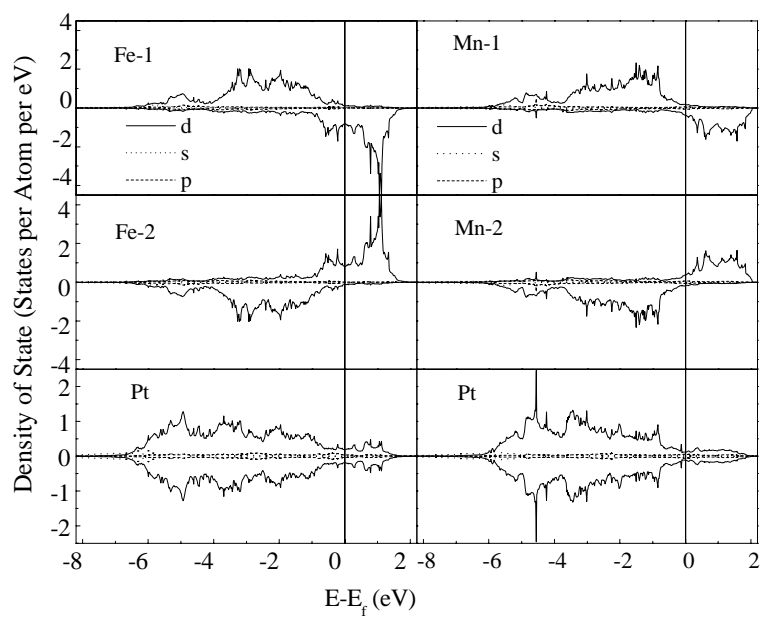


Fig. 4.8. Comparison of angular momentum projected densities of states of each atom in FePt and MnPt.

For both FePt and MnPt, the majority and minority DOS of Pt in model 2 are completely symmetric and almost fully occupied, so it is not strange that there is no moment on Pt for model 2. There are some empty minority d states in model 3 (FM phase) which leads to small moments on the Pt atoms. In model 1, both majority and minority d bands are not completely filled.

4.5 Effects of c/a Value on Magnetic and Electronic Properties

To study the effects of c/a on the magnetic and electronic properties of FePt and MnPt, we fixed the c/a ratio and minimized the energy with respect to unit cell volume.

Effects of c/a value on magnetic and electronic properties of FePt

1) Phase

Fig. 4.9 shows the c/a dependence of the total energy (a) for the three different structures of FePt. From our result, the ground state is model 3 (ferromagnetic phase). The absolute energy minimum is for model 3 at $c/a = 0.98$ which is taken as the reference energy. There are also additional local minima (at $c/a = 0.6$ for all structures and at $c/a = 0.94$ for model 1 and model 2). These local minima correspond to metastable states. The energy of model 2 is lower than that of model 3 for c/a in range of 0.52-0.948. The effect of spin-orbit coupling is small compared to the energy differences of Fig. 4.9.

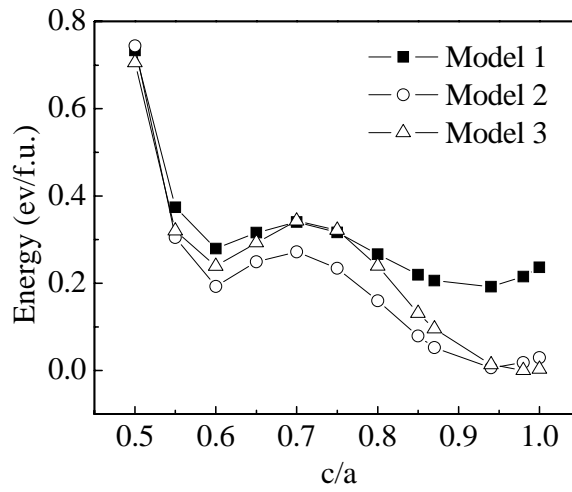


Fig. 4.9. Comparison of energies of the three structures of FePt at different c/a .

2) Anisotropy

As shown in Fig. 4.10, Model 1 has anisotropy perpendicular to the (001) plane when $c/a > 0.8$ and anisotropy in the (001) plane when $c/a < 0.8$. In its equilibrium state ($c/a = 0.908$), the anisotropy energy is quite high and comparable to that of model 3 which is well known for its large perpendicular anisotropy energy.

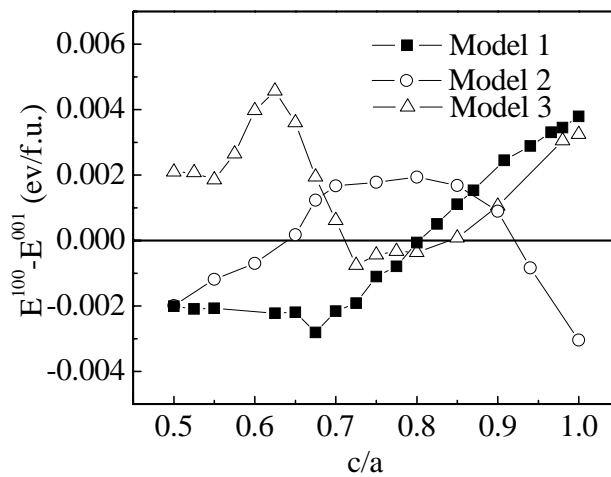


Fig. 4.10. c/a dependence of the anisotropy energies of FePt.

For model 2, the easy axis is in the [100] direction when c/a is large and switches to the [001] direction when c/a decreases. However, when c/a decreases further and becomes smaller than 0.65, its easy axis goes back to the [100] direction.

As for Model 3, at its ground state, the easy axis is perpendicular to the (001) plane and the anisotropy energy is high as is well known. However, according to our results, the easy axis could lie in the (001) plane if c/a were in the range of 0.7-0.8.

3) Moment on atoms

The effect of c/a on the moment of the atoms is shown in Fig. 4.11. The moment of Fe in model 1 and model 3 increases almost linearly with the decrease of c/a . In model 2, when c/a decreases to less than 0.6, the moment of Fe will decrease. There is no moment on Pt for model 1 and model 2, while there is a significant moment on Pt for model 3 (0.1 to $0.5\mu_B$). The moment of Pt in model 3 decreases with c/a after it reaches its maximum at $c/a = 0.85$.

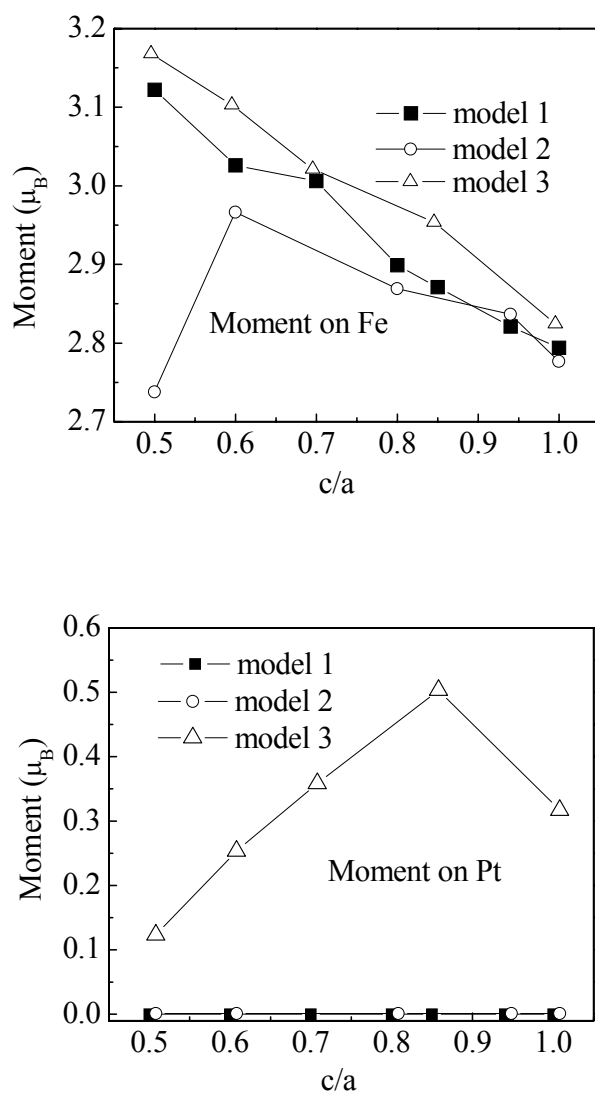


Fig. 4.11. Moment on each atom in FePt as a function of c/a .

Effects of c/a value on magnetic and electronic properties of MnPt

1) Phase

Fig. 4.12 shows the dependence of the energy of all three models of MnPt on c/a . Here, we set the ground state (model 1 with $c/a=0.928$) as reference. All the energy values are reported with respect to this reference. We include the results for spin-orbit coupling considered (LS) and

not considered (Non-LS). It seems that spin-orbit coupling has only a very tiny effect on the energy difference.

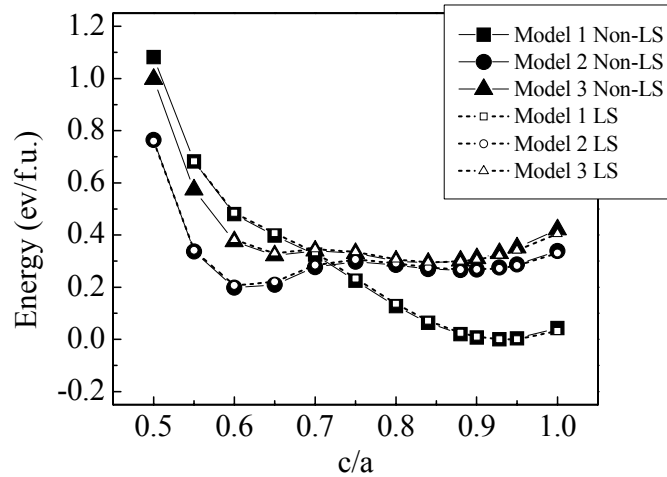


Fig. 4.12. Dependence of energies of MnPt on c/a .

For large c/a , model 1 is the most stable phase. With the decrease of c/a , the energy difference decreases and for $c/a < 0.7$, model 2 and model 3 have lower energy than model 1. However, model 3 always has higher energy than model 2. So, when $c/a < 0.7$, model 2 is the most stable phase. Model 3 is not stable at any c/a .

2) Anisotropy

Fig. 4.13 shows the dependence of the magnetocrystalline anisotropy energy on c/a . Model 1 always has in-plane anisotropy except when $c/a=1$. The MCA energy increases with the decrease of c/a . Model 3 has a large perpendicular MCA energy when c/a is big and the MCA energy decreases with the decrease of c/a and the easy axis will prefer to be in-plane for small c/a . As to model 2, the direction of its easy axis is dependent on c/a and switches between in-plane and out-of-plane with the change of c/a .

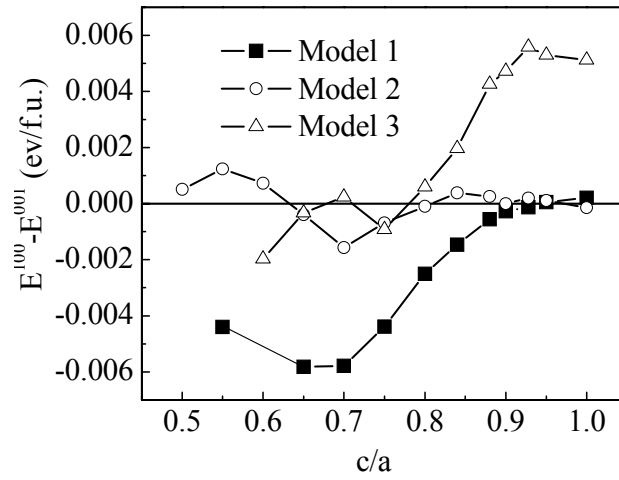


Fig. 4.13. Dependence of MCAs of MnPt on c/a .

3) Moment on atoms

According to our calculation, the magnitude of moment of Mn and Pt atoms do not change with the direction of the moments.

Fig. 4.14 shows the change of magnitude of atom moment with c/a . With c/a decrease, the moments of Mn atoms in all three model increase at the beginning and decrease with further decrease of c/a .

There is no moment on Pt atoms in model 1 and model 2. In model 3, the moments of Pt atoms change with c/a almost in the same way as those of Mn atoms.

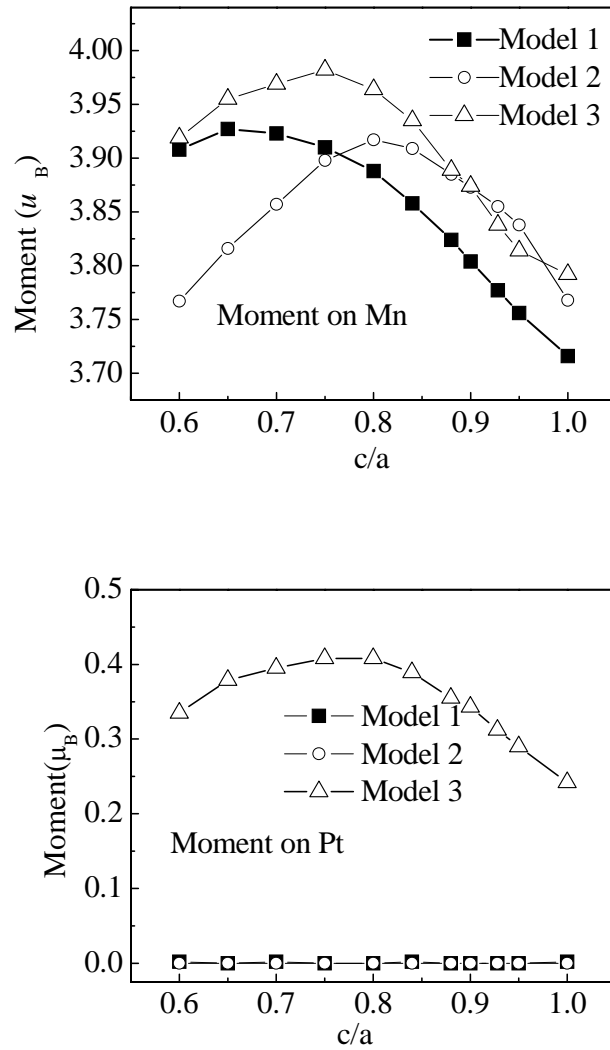


Fig. 4.14. Moment on each atom in MnPt as a function of c/a .

4.6 Discussion Based on Electronic Structures of FePt and MnPt

With the change of c/a , the distances between atoms are changed and the interactions between atoms change accordingly. Since the magnetic configuration is determined by the relative direction of the moments on adjacent 3d transition metal atoms, studying the change of PDOS of Fe/Mn with c/a may help us understand why MnPt and FePt prefer different phases.

Since, in all three models, the PDOS of the transition metal atoms change similarly, we use the PDOS of the Mn atom in model 1 of MnPt as an example. Table 4.4 shows the lattice constants at each c/a , the nearest Mn-Mn distance in the (001) plane and the nearest Mn-Pt distance. With the decrease of c/a , the Mn-Mn distance increases rapidly while the distance between Mn and Pt does not change much.

Table 4.4. Lattice constants and distances between atoms at different c/a .

c/a	1	0.8	0.5
a (Å)	3.890	4.309	5.057
c (Å)	3.890	3.367	2.528
$d_{\text{Mn-Mn}}$ (Å)	2.751	3.047	3.576
$d_{\text{Mn-Pt}}$ (Å)	2.751	2.720	2.827

The PDOS of Mn atoms in MnPt are shown in Fig. 4.15. The hybridization of the d states of each Mn atom with near Mn atoms and Pt atoms broadens its d bands. When the Mn-Mn distance is close to the Mn-Pt distance, we can expect that the hybridization among Mn atoms is much stronger than that between Mn and Pt. This can be seen when comparing the PDOS of Mn at $c/a=1$ with that at $c/a=0.8$. Mn is a transition atom with its 3d shell half filled which makes it favor antiferromagnetic coupling. However, according to the Bethe-Slater curve [69], with the increase of the distance between two atoms, ferromagnetic coupling will have lower exchange energy. With the decrease of c/a , Mn-Mn distance in the (001) plane increases and leads to ferromagnetic coupling in the (001) plane. In Fig. 4.12, we can clearly see when $c/a < 0.7$, model 2 and model 3 of MnPt have lower energy than model 1.

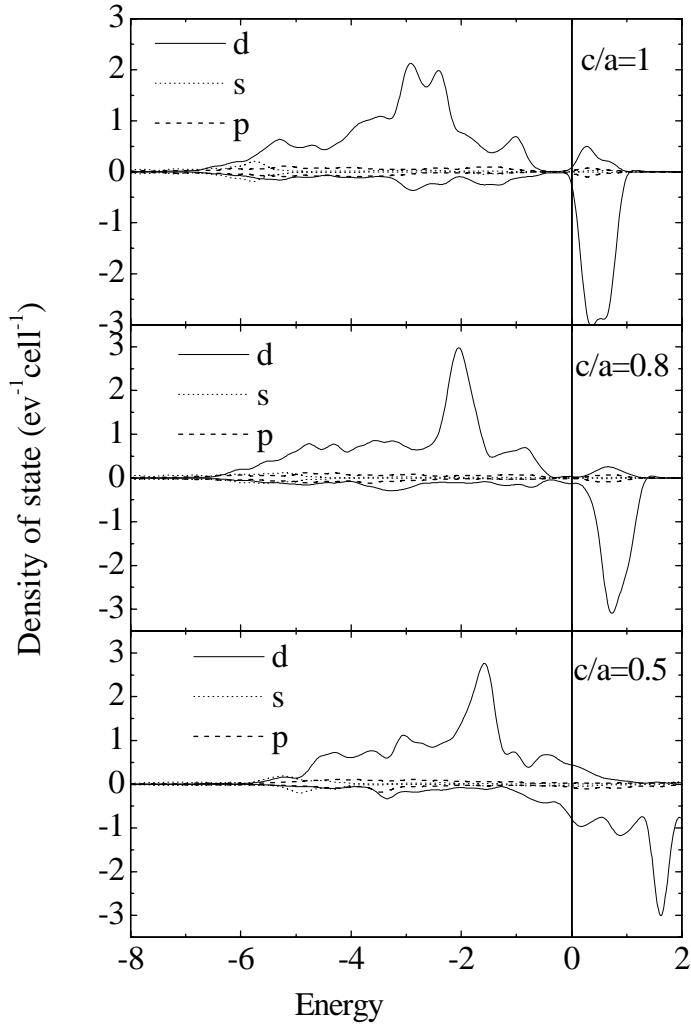


Fig. 4.15. Comparison of PDOSs of each Mn atom in model 1 of MnPt at different c/a .

As to FePt, since the d shell of Fe atom is more than half filled, it favors ferromagnetic coupling. The decrease of c/a leads to an increase of Fe-Fe distance in the (001) plane and will keep FM coupling between adjacent Fe atoms.

In the (100) planes of MnPt and FePt, the interaction between two the nearest 3d atoms is more complicated because of the Pt atom in the middle. However, from the results in Fig. 4.9 and Fig. 4.12, it seems that after ferromagnetic coupling is realized in the (001) plane, for a fairly large range of c , 3-d atoms in two adjacent (001) planes favor antiferromagnetic coupling.

Ferromagnetic coupling may be favored if c is small enough (see Fig. 4.10). Similar results were also obtained by J. T. Wang *et al.* in the MnAu system [70].

When c/a goes to 0.5, the adjacent Mn atoms in the [001] direction become very close and their interaction will again broaden the d state on a Mn site, which can explain why the Mn moment decreases when c/a decreases further.

4.7 Band Structure of MnPt near the Fermi Energy

In magnetoresistive spin-valves and magnetic tunnel junction devices, a highly conductive antiferromagnetic layer is desirable for high performance, especially for CPP devices. Low resistivity ($\sim 20\mu\Omega\text{cm}$) has been reported in $L1_0$ MnPt at room temperature and even lower resistivity (about $3\mu\Omega\text{cm}$) has been reported at 4.2 K [71].

In a cubic system, the conductivity of a metal per spin channel can be expressed as:

$$\sigma = \frac{e^2\tau}{3\hbar(2\pi)^2} \int_{S_k} dS_k \frac{v^2(k)}{|v(k)|} \quad (4.1)$$

In this expression, e is the charge of a electron, τ is the average collision time and $v(k)$ is the electron velocity.

From the band structure of MnPt model 1 (Fig. 4.16), the dispersion of a band near the Fermi energy is large which will make the electrons near the Fermi surface have large velocities. Thus, it is possible for MnPt to have a large conductivity even though the DOS at the Fermi Energy is very small.

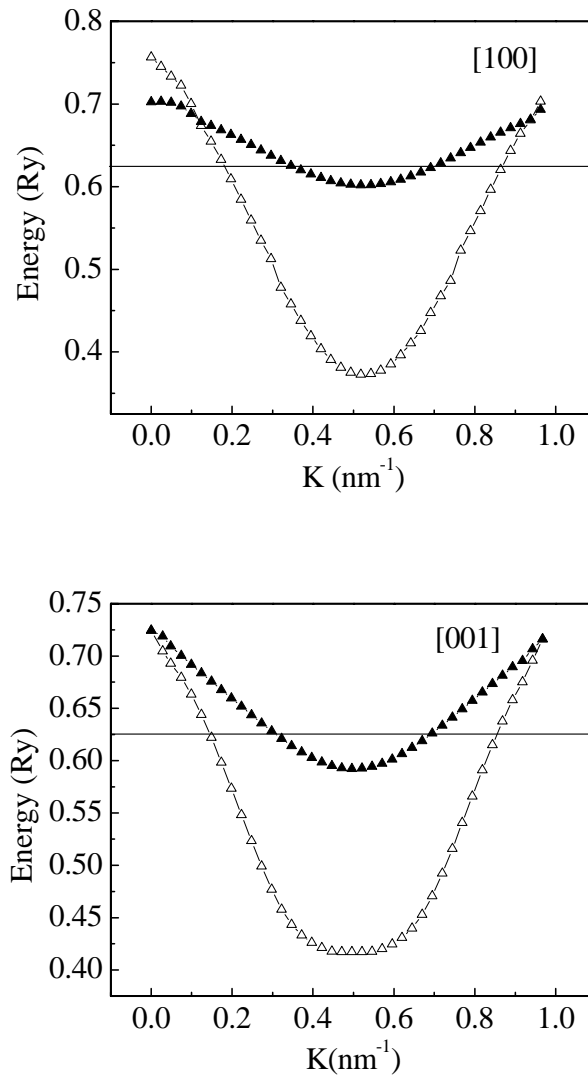


Fig. 4.16. Energy bands of MnPt (model 1) near the Fermi energy along [100] and [001] directions.

Conclusions

By using first principles method, the magnetic and electronic structures of three different spin configurations of $L1_0$ phase FePt and MnPt were studied. It was found that:

- 1) The most stable spin configuration of FePt is model 3 (ferromagnetic configuration) with c/a about 0.98. With the change of c/a , there is a phase competition between model 3 and

model 2. In the equilibrium state, both model 1 and model 3 have very large MCA with the easy axis along the [001] direction, while model 2 has a large MCA with the easy axis along the [100] direction.

2) The most stable phase of MnPt is model 1 – an antiferromagnetic phase with antiferromagnetic configuration along the [100] direction (model 1) and a c/a value of 0.92. Both model 1 and model 2, at their equilibrium states, have an easy axis along the [100] direction. As for model 3, a large MCA was found with easy axis along the [001] direction.

3) The c/a value has a strong effect on the magnetic structure and magnetic properties of both FePt and MnPt.

4) An energy band of ground state of MnPt (model 1) has large dispersion at Fermi energy, which leads to a large velocity for electrons at Fermi energy. This might be one of the reasons for MnPt to have smaller resistivity than other antiferromagnetic materials.

CHAPTER 5 EXPERIMENTAL TECHNIQUES AND EQUIPMENT

5.1 Sample Fabrication – Sputtering System

Sputtering is a very important technology in thin film fabrication and is widely used in industrial manufacturing and academic research. In my research, all the samples were fabricated by using DC sputtering.

Principle of Sputtering

When a negative voltage is applied between target (cathode) and substrate (anode), the free electrons will immediately be accelerated away from the target. When these accelerated electrons collide with the neutral gas atoms in their path, they will transfer some kinetic energy to the outer shell electrons of those gas atoms and make them flee away from the neutral gas atoms. Thus, the neutral gas atoms are ionized and become positively charged ions (e.g. Ar^+).

The positively charged ions are accelerated by the electric field and move toward the target. When they strike the surface, they transfer energy to the atoms of the target material and eject them from its surface. Some of the atoms will reach the surface of the substrate and deposit on it to form a film. However, some of the Ar^+ ions will combine with free electrons to form neutral Ar atoms and release photons – plasma forms. The striking of Ar^+ ions on the target surface creates a large amount of free electrons, which in turn feed the ion formation and sustain the plasma. This process is called “diode sputtering.”

Although "diode sputtering" has been proven to be a useful technique in the deposition of thin films, it has two major problems – the deposition rate is slow, and the electron bombardment

of the substrate is extensive and can cause overheating and structural damage. Therefore, today, most sputtering systems use so-called magnetron sputtering instead of “diode sputtering”. Fig. 5.1 shows how a magnetron sputtering system works. By using magnets behind the target to trap the free electrons in a magnetic field directly above the target surface, both of the problems for

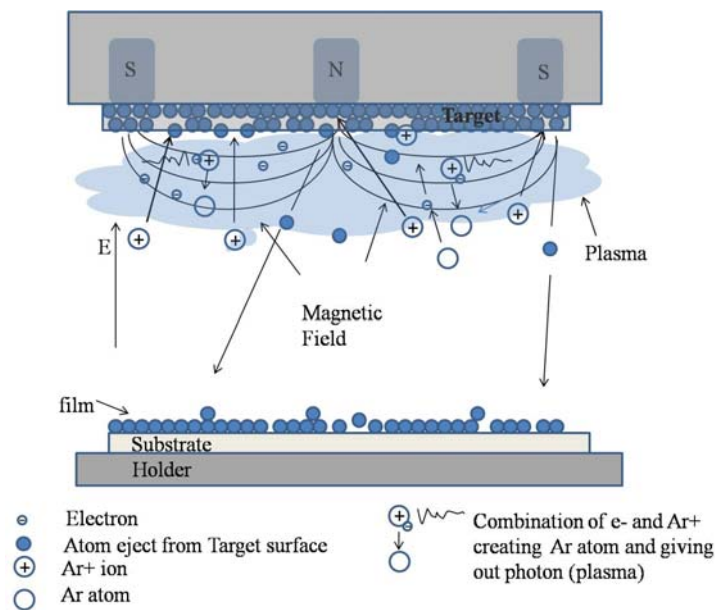


Fig. 5.1. Magnetron sputtering.

“diode sputtering” can be simultaneously solved. Constrained by the magnetic field, the electrons are not as free to bombard the substrate as with diode sputtering. At the same time, the extensive, circuitous path followed by these electrons when trapped in the magnetic field enhances their probability of ionizing a neutral gas molecule by several orders of magnitude. The increase in available ions significantly increases the rate at which target material is eroded and subsequently deposited onto the substrate.

Sputtering system description

The sputter deposition of the films is carried out in the ADAM sputtering chamber as shown in Fig. 5.2. The deposition and characterization are performed in the main chamber, which is evacuated using a CTI cryogenics Cryotorr 10 cryopump. A load lock chamber is used to transfer samples to and from the main chamber quickly. The load lock is pumped using a 260 l/s Balzers Turbo pump, which is backed by a GE rotary vane pump. The base pressure of the main vacuum chamber is less than 1×10^{-8} mbar as measured with a Kurt J. Lesker model IG200 ionization gauge. During sputtering, the Ar gas flow rate is adjusted using a 10 SCCM

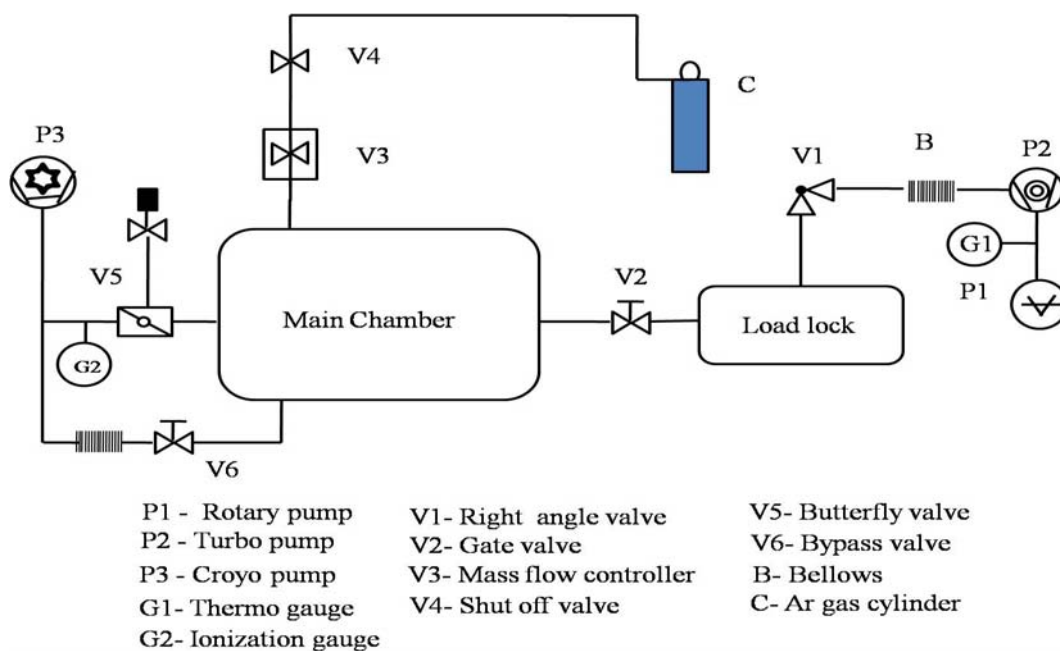


Fig. 5.2. Sputtering system.

MKS flow controller to keep the Ar pressure constant with the main valve to the cryopump closed and the bypass valve open, In this configuration the ion gauge reading of 4.5×10^{-5} mbar is approximately 100 times lower than the chamber pressure, which requires a few millitorr to maintain a stable plasma discharge from the magnetron guns. The MgO and sapphire substrates

obtained from Princeton Scientific are mounted on a custom-built sample plate made of pure titanium. The substrates are attached to the plate using thin Ta wires that are spot-welded across the corners. Six filaments from 500 W halogen light bulbs are used to make the sample heater element. The samples can be routinely heated to temperatures $> 750^{\circ}\text{C}$ with this setup.

Two models of sputtering guns from AJA International Inc. are used to deposit the films. The A300 series sputter gun uses a 1.5" target and requires a 4.5" conflat (CF) flange to hold the assembly. The A310-XP gun utilizes a 1" target and can be attached to a 2.75" CF flange, making it very useful to sputter precious metals. The ADAM system is equipped with four 1.5" sputter guns arranged in a square cluster, each directed at a 45° angle to the surface normal of the substrate at a working distance of 6". A single 1" gun in the center of the four-gun cluster is directed normal to the surface at a working distance of 5". All the guns are arranged such that the substrate is at the focus of the cluster. The sample thickness variation was within 5% over a 1" \times 1" area. The samples used in the experiments are smaller (1 cm x 1 cm), so sample uniformity is not an issue.

The sputter guns are operated using an Advanced Energy MDX 500 power source. The output of the power supply is connected to the sputter gun using an RG-8U coaxial cable. The target is negatively biased to about 300-500 V, and a plasma composed of Ar^+ ions and electrons is generated in the presence of a strong magnetic field produced by permanent magnet pole pieces attached to the copper cooling block adjoining the target. Targets of the pure elements are obtained from ACI Alloys Inc. The new targets are pre-sputtered for a few minutes to remove the surface contamination.

Temperature calibration

The sample heater is made of 6 filaments from halogen light bulbs with a maximum designed power of about 1500W. The heater holder is made of a Ta sheet and a thermocouple is mounted on it.

During the sputtering, the temperature is controlled by varying the applied voltage and

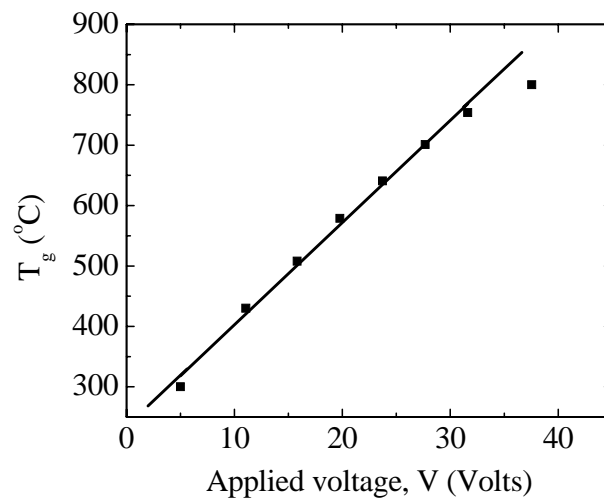


Fig. 5.3. Dependence of the growth temperature on the applied voltage.

is monitored by the reading of the thermocouple on the heater holder. Since we cannot directly measure the growth temperature of the sample during sputtering, temperature calibration must be carried out to determine the temperature of the sample as a function of the reading on the thermocouple and as a function of applied voltage. To do this, another thermocouple is mounted onto a sample plate and the temperatures of both the heater holder and sample plate were measured at the same time. The dependence of sample temperature on applied voltage is shown in Fig. 5.3. The growth temperature (T_g) of the sample depends almost linearly on applied voltage for temperatures up to 750°C. In the experiment, the highest growth temperature is 720°C.

Therefore, we can obtain the growth temperature from the applied voltage by using the linear equation

$$T_g = 16.9V + 233 \quad (5.1)$$

in which V is the applied voltage.

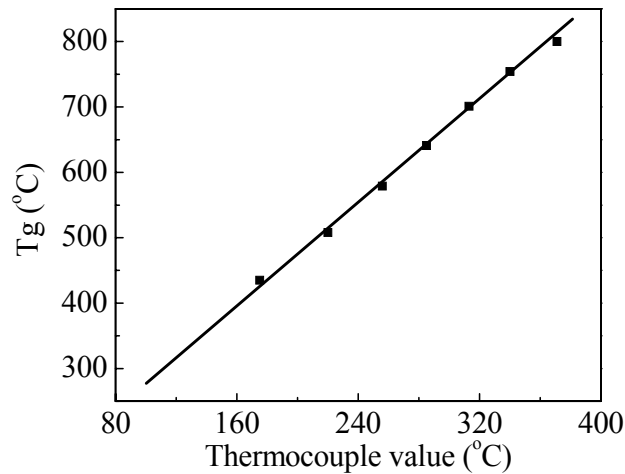


Fig. 5.4. Relation between the real growth temperatures and the thermocouple readings.

T_g depends linearly on the temperature given by the thermocouple as shown in Fig. 5.4. By using linear fitting, we can calculate the sample temperature from the temperature of heater holder.

$$T_g = 2.02T_m + 64.8 \quad (5.2)$$

where T_m is the temperature of the thermocouple.

Characterizations

For sample characterization, a Philips X' Pert multipurpose X-ray diffractometer is used to study the crystal structure and orientation, and a model 2900 MicroMagTM alternating

gradient magnetometer made by The Princeton Measurements Corp. is used to measure magnetic properties of samples.

5.2 Crystal Structure Characterizations – X-ray Diffractometry

Diffraction and the Bragg equation

X-ray diffraction is an important non-destructive analytical technique that reveals information about the crystallographic structure and physical properties of materials and thin films. This technique is based on observing the scattered intensity of an X-ray beam hitting a sample as a function of the incident and the scattered angle. Diffraction of an X-ray beam striking a crystal occurs because the wavelength λ of the X-ray beam is similar to the spacing of atoms in the lattice (1-10 Å). When an X-ray beam encounters the regular, 3-D arrangement of atoms in a crystal, most of the X-rays will destructively interfere with each other, but, in some specific directions they constructively interfere and reinforce one another. It is these reinforced (diffracted) X-rays that produce the characteristic X-ray diffraction patterns that are used to determine the structure of a material.

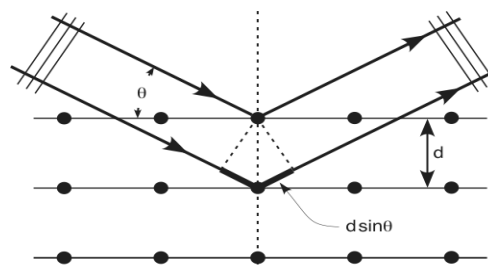


Fig. 5.5. X-ray diffraction.

In the early 1900's, L. Bragg [72] showed that diffracted X-rays act as if they were "reflected" from a family of planes within crystals as shown in Fig. 5.5. Bragg's planes are the rows of atoms that make up the crystal structure. These "reflections" were shown to only occur under certain conditions that satisfy the equation:

$$2d \sin \theta = n\lambda \quad (\text{Bragg equation}) \quad (5.3)$$

where n is an integer (1, 2, 3, ...), λ is the wavelength, d is the distance between atomic planes, and θ is the angle of incidence between the X-ray beam and the atomic planes. $2d\sin\theta$ is the path length difference between two incident X-ray beams where one X-ray beam takes a longer (but parallel) path because it "reflects" off an adjacent atomic plane. This path length difference must be equal to an integer value times the wavelength of the incident X-ray beam for constructive interference to occur.

Phillip X'Pert X-ray diffractometer

The Philips X'pert unit is a four-axis diffractometer made specifically for the analysis of crystalline materials. It is equipped with four different pieces of optics for the incident beam and diffracted beam optics. By combining these optics components, a number of different types of analysis can be performed. The structure of the diffractometer is shown in Fig. 5.6. The X-ray source used in the X'pert is a ceramic filament tube with a Cu target. The filament is made of tungsten and it is normally operated at 40 kV and 45 mA. Cu gives a K_{α} with a wavelength of 1.542 Å (average of $K_{\alpha 1}$ with wavelength 1.540 Å and $K_{\alpha 2}$ with wavelength 1.544 Å) and K_{β} with wavelength of 1.3922 Å. The focal spot is 12 mm × 0.4 mm. The tube can have either a point focus or a line focus. In our measurements, line focus is used.

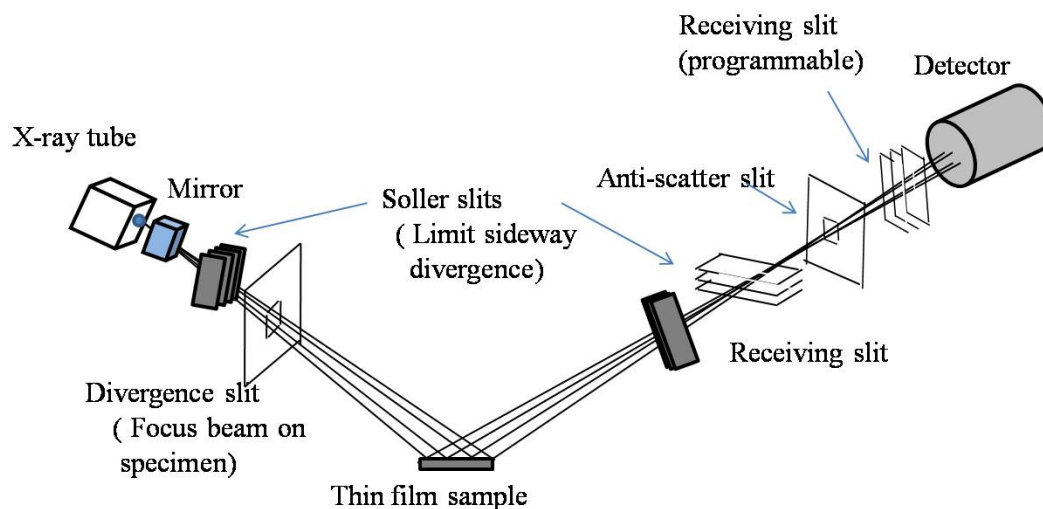


Fig. 5.6. Structure of the X-ray diffractometer.

The X-ray Mirror eliminates the K_{β} radiation giving a dichromatic beam of $K_{\alpha 1}$ and $K_{\alpha 2}$ and it makes the incident beams quasi-parallel with a horizontal divergence of only 0.05° .

When using a line source, radiation will emerge in directions both above and beneath the plane of incidence. To remove the out-of-plane radiation, Soller slits are used. They consist of a set of closely spaced, thin metal plates parallel to the plane of the diffractometer circle. The X'pert diffractometer is equipped with 0.04 rad Soller slits to limit the divergence to the diffractometer plane.

The divergence slit defines the angular divergence of the incident beam on the sample. It must be chosen to accommodate the necessary 2θ range and the size of the sample. The X'pert has divergence slits ranging from 1/32" to 1".

An antiscatter slit is usually used together with a programmable receiving slit. Its main function is to reduce the amount of scatter that enters the programmable receiving slit.

The goniometer

The goniometer is a four-axis system with 2θ , ω , ϕ and ψ as the variables. Fig. 5.7 shows the definition of these angles. 2θ is the angle between the incident beam and the diffracted beam. ω is the angle between the incident beam and the sample surface and should be equal to θ . However, it can be varied independently of 2θ . ϕ is the rotation angle about the sample normal and ψ is the tilt angle about a horizontal and centered line in the sample surface.

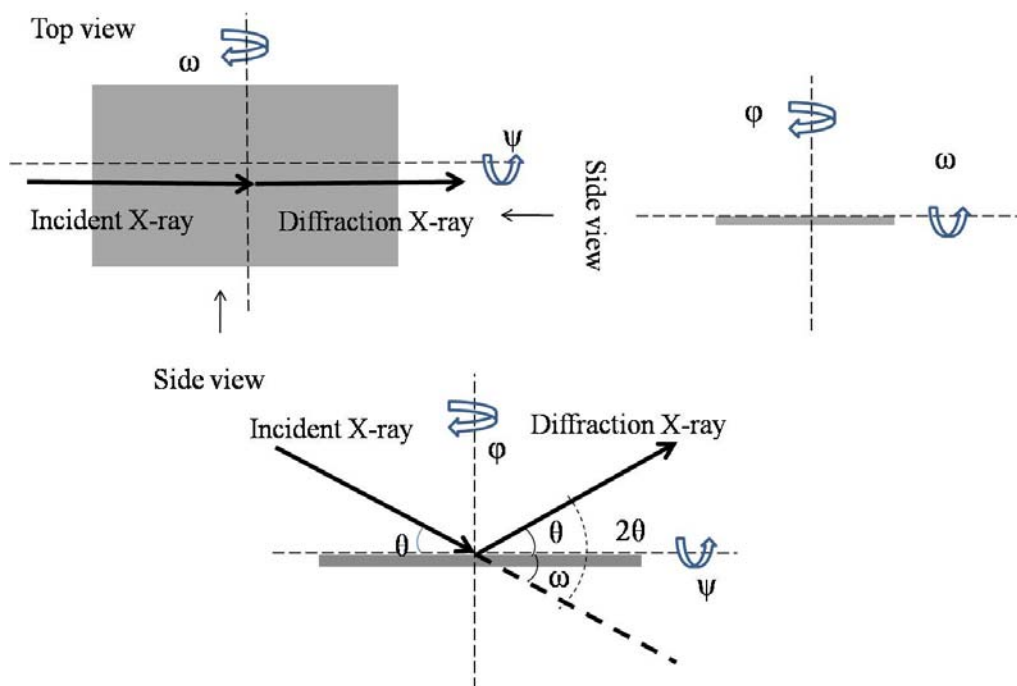


Fig. 5.7. Definition of angles: θ , ω , ϕ and ψ .

5.3 Magnetic Characterizations – Alternating Gradient Magnetometry

The Princeton Measurements Corp. Model 2900 MicroMagTM Alternating Gradient Magnetometer (AGM) is a highly-sensitive, compact, computer controlled susceptibility measurement system. It is capable of measuring the magnetic properties of a wide range of sample materials.

Principle

The Model 2900 MicroMag™ Alternating Gradient Magnetometer (AGM) uses an alternating gradient field to produce a periodic force on a sample placed in a variable or static D.C field. The sample is mounted on an extension rod attached to a piezoelectric element as shown in Fig. 5.8. The magnets apply a variable or static DC magnetic field H to change the

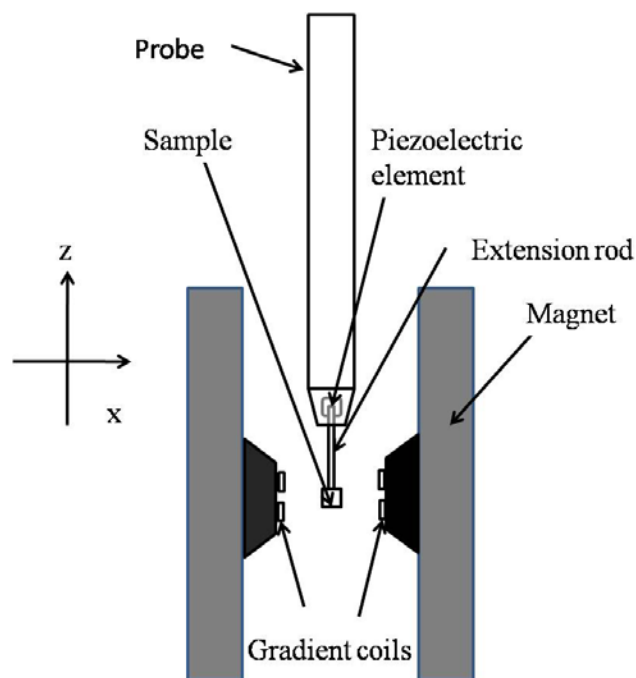


Fig. 5.8. AGM probe and sample position.

magnetization of the sample. At the center of the cores, there are four gradient coils which generate an alternating field, $h = h_0 \sin \omega t$. The alternating field gradient exerts an alternating force on the sample proportional to the magnitude of the gradient field and the magnetic moment of the sample, and can be expressed as:

$$F_x = m_x dh/dx \quad (5.4)$$

The resulting deflection of the extension is transmitted to the piezoelectric sensing element. The output signal from the piezoelectric element is synchronously detected at the operating frequency of the gradient field. The signal developed by the piezoelectric element is greatly enhanced by operating at or near the mechanical resonant frequency of the assembly. A built-in software function automatically determines mechanical resonance and sets the appropriate operating frequency for the sample under study.

Sample alignment

AGM measurement is automatic and computer controlled. The only manual operation is the sample alignment. Good alignment of the sample is very important for the equipment to find the correct resonant frequency. The Model 2900 MicroMagTM AGM has a manual alignment system for one to adjust the sample position along the x, y, and z direction as shown in Fig. 5.9. The correct alignment is achieved when the sample is placed at the center of the magnets.

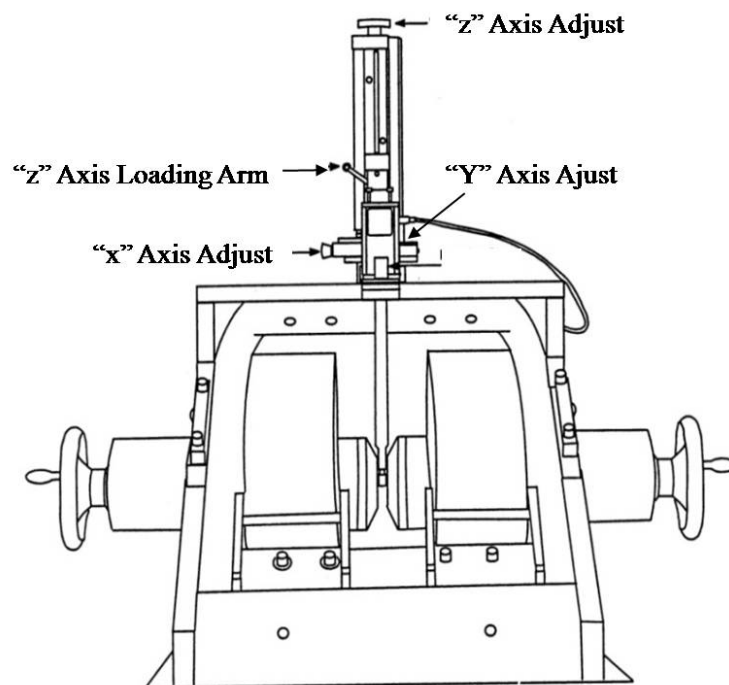


Fig. 5.9. Structure of Model 2900 MicroMagTM AGM [73].

5.4 Characterization of Magnetic Structures – Neutron Scattering and Polarized Neutron Reflectometry

Neutron diffraction is a powerful tool for studying magnetic materials. The magnetic scattering of neutrons results from the dipole-dipole interaction between the neutron and the magnetic moment of an atom. A neutron has a spin of $\frac{1}{2}$ and generates a magnetic moment of $1.91 \mu_N$, where $\mu_N = 5.05 \times 10^{-27} \text{ J/T}$. The cross section for magnetic scattering is sensitive to the relative orientation of the neutron's magnetic moment, the atomic magnetic moment, and the scattering vector. This allows the magnetic structure to be determined from the intensities of magnetic diffraction peaks, in much the same way that crystal structures are determined from the intensities of X-ray diffraction peaks. Small-angle neutron scattering and polarized neutron reflectometry can yield magnetic information over a range of length scales, and can be applied to magnetic nano-particles, spin glasses, and magnetic multilayers.

Magnetic Neutron Scattering

The amplitude of magnetic neutron scattering from a magnetic atom was first determined by Halpern and Johnson[74] as:

$$\alpha_M = pf(\mathbf{Q})\mu_{\perp} \quad (5.5)$$

where p here is a constant related to the magnetic moment of neutrons, f is the magnetic structure factor, \mathbf{Q} is the scattering vector and μ_{\perp} is the component of the atomic magnetic moment in the diffraction plane and perpendicular to \mathbf{Q} . Fig. 5.10 shows the relation between the direction of \mathbf{Q} and that of $\boldsymbol{\mu}$.

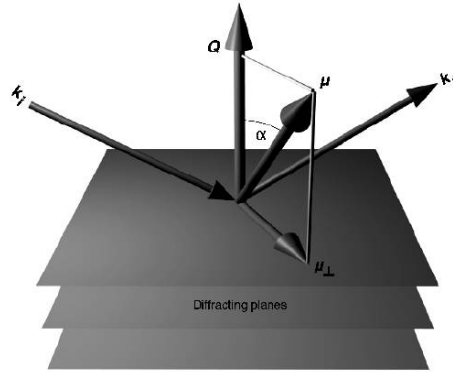


Fig. 5.10. Angular relation between the scattering vector and the magnetic interaction vector for magnetic neutron scattering [75].

The constant p is defined as

$$p = \frac{\mu_N}{2} \left(\frac{e^2}{mc^2} \right) = 0.2696 \times 10^{-12} cm$$

where μ_N is the magnetic moment of the neutron in nuclear magnetons, e is the electron charge, m is the electron mass and c is the speed of light. The term in parentheses is equivalent to the classical electron radius ($r_e = 0.282 \times 10^{-12} cm$).

The perpendicular component of the atomic moment μ_{\perp} can be expressed as

$$\mu_{\perp} = \hat{Q} \times \mu \times \hat{Q} \quad (5.6)$$

where \hat{Q} is a unit vector of parallel to Q

According to Eq. 5.5, we can see that magnetic neutron scattering is only determined by μ_{\perp} . The magnetic contribution will be zero if the moments are normal to the diffraction planes or parallel to the diffraction vector. To have a component in the diffraction plane is one of the basic requirements that allow magnetic structures to be determined from neutron diffraction.

Neutrons are scattered by the magnetization density of an atom. Since the magnetic moment originates from the electrons, interference between neutrons scattered from different

parts of the electron cloud causes the amplitude of magnetic scattering to decrease with an increase in magnitude of \mathbf{Q} . This decrease is described by the atomic magnetic form factor $f(\mathbf{Q})$ which can be expressed as [76]:

$$f(\mathbf{Q}) = \frac{1}{\mu} \int \rho_M(\mathbf{r}) e^{i\mathbf{Q}\cdot\mathbf{r}} dV \quad (5.7)$$

where μ is the magnetic moment of an atom, $\rho_M(\mathbf{r})$ is the unpaired spin density of the atom at position \mathbf{r} in the volume of an atom.

According to Rodriguez-Carvajal [77], the magnetic structure factor, $F_M(\mathbf{Q})$, can be defined as:

$$F_M(\mathbf{Q}) = p \sum_{j=1}^{n_m} f_j(\mathbf{Q}) \boldsymbol{\mu}_j e^{i\mathbf{Q}\cdot\mathbf{r}_j} \quad (5.8)$$

with $f_j(\mathbf{Q})$, $\boldsymbol{\mu}_j$ and \mathbf{r}_j representing the atomic magnetic form factor, magnetic moment and the position of the j^{th} atom in the crystallographic unit cell. n_m represents the number of magnetic atoms in the unit cell.

The intensity of the Bragg diffraction peak is determined by the component of $F_M(\mathbf{Q})$ perpendicular to \mathbf{Q} , and can be expressed as

$$I_M(\mathbf{Q}) = F_{M\perp}(\mathbf{Q}) \cdot F_{M\perp}^*(\mathbf{Q}) \quad (5.9)$$

where $F_{M\perp}(\mathbf{Q})$ and $F_{M\perp}^*(\mathbf{Q})$ represent the perpendicular component of $F_M(\mathbf{Q})$ and its complex conjugate.

For a collinear magnetic structure, the intensity of magnetic neutron scattering can be written in the form:

$$F_{M\perp}^2(\mathbf{Q}) = \sin^2 \alpha F_M^2(\mathbf{Q}) \quad (5.10)$$

where α is the angle between the magnetic structure factor and the scattering vector as shown in Fig. 5.10.

So far, we have only considered the contribution of magnetic scattering to the Bragg peak. However, nonmagnetic scattering is always present. This arises from the scattering of neutrons by the atomic nuclei. The nuclear contribution to the Bragg intensity can be expressed as

$$I_N = F_N(\mathbf{Q}) \cdot F_N^*(\mathbf{Q}) \quad (5.11)$$

where $F_N(\mathbf{Q})$ and $F_N^*(\mathbf{Q})$ are the nuclear structure factor and its complex conjugate.

As we know, the diffraction peak appears when the Bragg condition is satisfied. The nonmagnetic neutron scattering probes the lattice structure of a crystal. To satisfy the Bragg condition, its scattering vector should be selected among a set of reciprocal lattice vectors \mathbf{H} ,

$$\mathbf{Q} = 2\pi\mathbf{H} \quad (5.12)$$

When the periodicity of the magnetic structure is equal to that of the nuclear structure, the Bragg peak is the sum of the contributions of nuclear scattering and magnetic scattering.

$$I_{tot} = F_N(\mathbf{Q}) \cdot F_N^*(\mathbf{Q}) + F_{M\perp}(\mathbf{Q}) \cdot F_{M\perp}^*(\mathbf{Q}) \quad (5.13)$$

Since the moment of a magnetic atom changes with the temperature as demonstrated, by the temperature dependent neutron scattering measurements, the contribution from magnetic scattering can be determined.

In general, the periodicity of the magnetic structure is not the same as that of the nuclear structure. This can be clearly seen from what we have shown in chapter 4 – in the antiferromagnetic phase (phase 1) of a material with $L1_0$ structure, the periodicity of the magnetic structure is 2 times of that of nuclear structure. In this case, the scattering vectors take the form:

$$\mathbf{Q} = 2\pi(\mathbf{H} + \mathbf{k}) \quad (5.14)$$

with \mathbf{k} referring to the propagation vector of a magnetic structure. Since the magnetic scattering and nuclear scattering satisfy different Bragg conditions, they will have different Bragg peaks.

Polarized neutron reflectometry

Polarized neutron reflectometry (PNR) is a very important technique for studying magnetic surfaces, thin films, interfaces, and multilayer systems [78,79].

Fig. 5.11 shows the scattering geometry in PNR experiments. The magnetic field is usually applied within the sample plane. The applied field direction also defines the polarization axis of the neutron beam. Four different cross-sections can be measured as functions of the scattering vector \mathbf{Q} . The scattering vector can be scanned either by varying the scattering angle with a fixed neutron wavelength or by varying the neutron wavelength with a fixed scattering angle, depending on the type of neutron source.

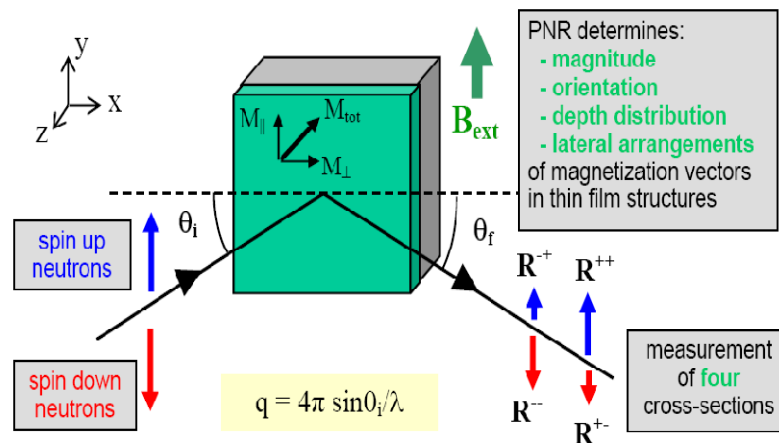


Fig. 5.11. Scattering geometry of polarized neutron reflectometry.

For a flat and homogenous surface, the scattering is specular with the diffraction angle θ_f equal to the incident angle θ_i . In this case, reflectometry measures the chemical and magnetic

depth profile along the z axis. According to first approximation of Born, the diffraction intensity can be expressed as

$$I \propto \frac{1}{Q_z^4} \int \frac{dV(z)}{dz} e^{-iQ_z z} dz \quad (5.15)$$

where Q_z is the z component of a neutron scattering vector, z is the distance from the film surface, and $V(z)$ is the potential acting on the neutron at a depth z inside the film. This means that the intensity of a specular reflection is proportional to the square of the Fourier transformation of the gradient of the potential profile perpendicular to the surface. For a homogeneous layer consisting of a pure element and with all its magnetic moments aligned parallel to B_{ext} , $V(z)$ is constant throughout its depth and is given by

$$V(z) = \frac{2\pi\hbar n}{m_n} (p_n \pm p_m) \quad (5.16)$$

where n is the number density, m_n is the neutron mass, \hbar is the reduced Planck constant, p_n is the nuclear scattering length and p_m is the magnetic scattering length. The positive sign represents the potential for a neutron spin parallel to the applied field (spin up) and the negative sign gives the potential for spin antiparallel to the applied field (spin down).

When there is no perpendicular component of the magnetic moment, spin orientation does not change before and after reflection, with R^{++} representing the reflectivity of reflection from a spin-up state to a spin-up state, and R^{--} representing the reflectivity of reflection from a spin-down state to a spin-down state. When only perpendicular components of the magnetic moment exist, spin-flip scattering will occur and the spin orientation changes after reflection with R^{+-} and R^{-+} representing the reflectivity of reflection from a spin-up state to a spin-down state and the reflectivity of reflection from a spin-down state to spin-up state, respectively. In most cases, both non spin-flip and spin-flip reflection exist, R^{++} , R^{--} , R^{+-} , and R^{-+} together will determine the direction and magnitude of the magnetization vector of a thin film. In contrast to

the diffraction regime, reflectivity is measured at low momentum transfer, and therefore, $V(z)$ is a locally averaged potential. When the material consists of different atomic species, $V(z)$ is the summation of the contributions from all species. For a sequence of layers, $V(z)$ changes continuously along the depth of the film. Therefore, PNR can give information about the depth distribution of the magnetization vectors of a multilayer film.

CHAPTER 6 MAGNETIC PROPERTIES OF Fe₅₀Pt₅₀ FILMS WITH GRADED ORDER PARAMETERS

Introduction

Fully ordered L₁₀ phase equiatomic FePt alloys have extremely large crystalline anisotropy up to 7×10^6 J/m³ with the anisotropy direction along [001] direction. If equiatomic FePt films with [001] orientation can be applied in fabricating perpendicular magnetic recording media, the grain size can be reduced to several nanometers without losing acceptable thermal stability. With this kind of small grain size, the areal density can approach to 10Tb/in² [80]. Thus, L₁₀ phase equiatomic FePt alloy is believed to be one of the most promising candidates for ultrahigh density magnetic recording. However, in the past decade, although L₁₀ phase equiatomic FePt alloy films were widely studied, challenges remain that prevent them from being applied in the fabrication of magnetic recording media. One of the biggest challenges is the writability problem.

According to our calculations shown in chapter 2 and chapter 3, the coercivity of a fully ordered equiatomic FePt film can be drastically decreased if we can use it as the hardest end of a multilayered structure whose anisotropy decreases gradually along the thickness. An important technical challenge for enabling this concept is developing the ability to control the magnetic anisotropy of each magnetic layer so that the anisotropy profile of the multilayered structure can be designed.

Previous studies [81, 82] showed that the anisotropy of an equiatomic FePt alloy depends

on its chemical order parameter. It is possible to build a multilayered structure stacked with FePt films with different order parameters.

In this chapter, we study the dependence of the magnetic properties of epitaxial FePt films on order parameter S , and demonstrate that the magnetic anisotropy can be tuned by controlling the chemical order parameter S . Based on this result, we build multilayered structures with anisotropy monotonically changing along the thickness and confirm that these kinds of multilayered structures can help to solve the writability problem of fully ordered equiatomic FePt.

6.1 Sample Fabrication and Order Parameter Determination

Degassing substrate

After the MgO substrate is loaded into the chamber, it must be degassed. The temperature for degassing is about 50-100°C above the deposition temperature. Degassing proceeds until the pressure in the chamber returns back to about 4×10^{-8} torr. The higher the deposition temperature, the longer time it will take for degassing. For a deposition temperature of 300-400°C, the degassing time is about 10-20 minutes. For a deposition temperature $>700^\circ\text{C}$, the degassing time is more than 30 minutes.

Deposition

After degassing is finished, the temperature is set to a designed growth temperature. Deposition begins when the temperature becomes stable around the setting temperature. The base pressure is now about 4×10^{-8} torr. High purity Ar gas is backfilled into the chamber by adjusting the flow controller until the pressure shown in the gauge is 3.6×10^{-5} torr. The structure of the films is shown in Fig. 6.1. A 4 nm Cr layer is deposited on the MgO substrate first with a DC power of 60 W at a sputtering rate of about 0.25 Å/s. A 12nm Pt layer is deposited on the

top of the Cr layer with a 25 W DC power and a sputtering rate of about 0.46 Å/s. Before the Fe₅₀Pt₅₀ film is deposited, the DC power is turned on with a setting value of 20 W, the shutter is closed, and the Ar pressure is increased by adjusting the gas flow controller. When the plasma is on, the Ar pressure is decreased back to 3.6×10⁻⁵ torr. After the plasma becomes stable, the shutter is opened. The sputtering rate of Fe₅₀Pt₅₀ is 0.64 Å/s. After the deposition of the Fe₅₀Pt₅₀ layer is finished, the Ar flow is closed, the heater is turned off, and the gate valve is opened. The substrate is cooled down in a vacuum around 4×10⁻⁸ torr. It takes about half an hour for the temperature to go below 100°C. After the temperature drops below 100°C, a 5nm Pt capping

Pt (5nm)
Fe₅₀Pt₅₀ (30nm or 50nm)
Pt (12nm)
Cr (4nm)
MgO (substrate)

Fig. 6.1. Structure of samples with a uniform Fe₅₀Pt₅₀ film.

layer is deposited on the top of the Fe₅₀Pt₅₀ layer. The deposition pressure and power are still 3.6×10⁻⁶ torr and 25 W.

Determination of order parameter

The X-ray data contains quantitative information about the chemical ordering of the epitaxial films. It is possible to estimate the chemical order parameter of the films by integrating the intensity of (00*l*) (*l*=1 and 2) and using the following formula [82]:

$$S^2 = \frac{(I_{001}/I_{002})_{exp}}{(I_{001}/I_{002})_{S=1}} \quad (6.1)$$

here I_{002} and I_{001} are the integrated intensities of the fundamental (002) peak and the superlattice (001) peaks of $\text{Fe}_{50}\text{Pt}_{50}$, and $(I_{001}/I_{002})_{exp}$ and $(I_{001}/I_{002})_{S=1}$ are the experimental ratio and calculated peak intensity ratio for perfect chemical order, respectively. The calculated intensity ratio for perfect chemical order of the (001) and (002) peaks can be computed by considering atomic fractions, atomic scattering factors, Debye-Waller corrections, and Lorentz polarization factors.

Calculation of peak intensity ratio for perfectly chemical ordered FePt thin films

The area of a peak can be expressed by equation [83]:

$$I \propto (LP)FF^* \quad (6.2)$$

where LP is the Lorentz polarization factor for a single crystal and F and F^* are the structure factors and its complex conjugate.

For epitaxial films, the Lorentz polarization factor can be expressed as [83]:

$$LP = \frac{1+\cos^2(2\theta)}{\sin(\theta)\cos(\theta)} \quad (6.3)$$

For a fully ordered equiatomic FePt film, the structure factor F is given by

$$F = 2f_{Fe} + 2f_{Pt}, \quad \text{fundamental peak, } hkl \text{ unmixed} \quad (6.4)$$

$$F = (2f_{Fe} - 2f_{Pt}), \quad \text{superlattice peak, } hkl \text{ mixed} \quad (6.5)$$

where $f_{Fe/Pt}$ is the atomic scattering factor of a Fe/Pt atom.

When considering the Debye-Waller correction [84], the structure factor will be

$$F = 2f_{Fe}e^{-W_{Fe}} + 2f_{Pt}e^{-W_{Pt}} \quad (6.6)$$

And

$$F = (2f_{Fe}e^{-W_{Fe}} - 2f_{Pt}e^{-W_{Pt}}) \quad (6.7)$$

where $e^{-W_{Fe(Pt)}}$ represents the Debye-Waller correction for Fe (Pt) atoms.

Thus, we have

$$FF^* = 4[(r_{Fe}e^{-W_{Fe}} + r_{Pt}e^{-W_{Pt}})^2 + (\Delta_{Fe}e^{-W_{Fe}} + \Delta_{Pt}e^{-W_{Pt}})^2] - \text{fundamental} \quad (6.8)$$

$$FF^* = 4[(r_{Pt}e^{-W_{Pt}} - r_{Fe}e^{-W_{Fe}})^2 + (\Delta_{Pt}e^{-W_{Pt}} - \Delta_{Fe}e^{-W_{Fe}})^2] - \text{superlattice} \quad (6.9)$$

In these equations, $r_{Fe(Pt)}$ and $\Delta_{Fe(Pt)}$ represent the real and imaginary parts of the atomic scattering factors.

In our research, all the samples are thin films with thickness <150 nm. For thin films, X-ray diffraction intensity also significantly depends on film thickness. Therefore, we need to consider the film thickness factor G_t , which can be expressed as [85]:

$$G_t = 1 - \exp\left(-\frac{2\mu t}{\sin \theta}\right) \quad (6.10)$$

where μ is the linear absorption coefficient and t is the film thickness.

To calculate the linear absorption coefficient of $Fe_{50}Pt_{50}$, we first calculate the mass absorption coefficient of it by using the following equation

$$\left(\frac{\mu}{\rho}\right)_{FePt} = w_{Fe} \left(\frac{\mu}{\rho}\right)_{Fe} + w_{Pt} \left(\frac{\mu}{\rho}\right)_{Pt} \quad (6.11)$$

where $(\mu/\rho)_{FePt}$, $(\mu/\rho)_{Fe}$ and $(\mu/\rho)_{Pt}$ are the mass absorption coefficients of Fe, Pt and FePt respectively. w_{Fe} and w_{Pt} are the weight fractions of Fe and Pt in $Fe_{50}Pt_{50}$ alloy. The mass absorption coefficients of Fe and Pt can be obtained from the website of the National Institute of Standards and Technology (<http://physics.nist.gov/PhysRefData/XrayMassCoef/chap2.html>).

After we obtain the mass absorption coefficient of the $Fe_{50}Pt_{50}$ alloy, the linear absorption coefficient can now be easily calculated by using

$$\mu = \left(\frac{\mu}{\rho}\right)_{FePt} \times \rho_{FePt} \quad (6.12)$$

After considering the thickness factor, the diffraction intensity of a peak can thus be expressed as

$$I = (LP)G_tFF^* \quad (6.13)$$

All the parameters [86] needed for calculation of peak intensity of fully chemical ordered $\text{Fe}_{50}\text{Pt}_{50}$ are shown in Table 6.1.

Table 6.1. Parameters for the calculations of (001) and (002) peak intensities.

Peak	2θ	LP	W_{Fe}	r_{Fe}	Δ_{Fe}	W_{Pt}	r_{Pt}	Δ_{Pt}	G_t
(001)	23.7	4.57	0.0054	21.01	3.4	0.0054	64.43	8	0.167
(002)	48.6	1.916	0.020	16.93	3.3	0.019	45.81	7	0.077

Based on the parameters shown in Table 6.1, we can calculate the intensity ratio of the (002) and (001) peaks of fully ordered $\text{Fe}_{50}\text{Pt}_{50}$ films. The ratio is 1.93 for epitaxial $\text{Fe}_{50}\text{Pt}_{50}$ films with a thickness of 50 nm and 1.95 for epitaxial $\text{Fe}_{50}\text{Pt}_{50}$ films with a thickness of 30 nm.

For the experimental peak intensity ratio, we use the Lorentz function to fit each peak to accurately find the integrated intensity.

6.2 Crystal Structures and Magnetic Properties of Uniform $\text{Fe}_{50}\text{Pt}_{50}$ Films

Crystal Structure

Fig. 6.2 shows XRD patterns of $\text{Fe}_{50}\text{Pt}_{50}$ films on MgO (100) substrates as a function of growth temperature (T_g), ranging from 300-720°C. For the film deposited at 300°C, a (200) diffraction peak corresponding to epitaxial, chemically-disordered $\text{Fe}_{50}\text{Pt}_{50}$ is observed at a scattering angle of 47.5°. For the film deposited at 400°C, a small (001) superlattice peak appears at a scattering angle of 23.5°, which indicates that the chemical ordering of the Fe and Pt atoms on the fcc lattice sites begins to occur at a growth temperature of 400°C. Compared with $\text{Fe}_{50}\text{Pt}_{50}$ films deposited directly on the MgO(100) substrate [86], the (001) peak that corresponds to long-range chemical order begins to appear at a lower temperature when the film is deposited on a Cr/Pt seed layer. With an increase in substrate temperature, the (001) peak increases further in

intensity relative to the intensity of the (002) peak. In addition, the peak position of (002) plane shifts to a higher angle with an increase in T_g , which corresponds to a decrease of the c-axis lattice parameter due to the formation of the chemically-ordered $L1_0$ structure.

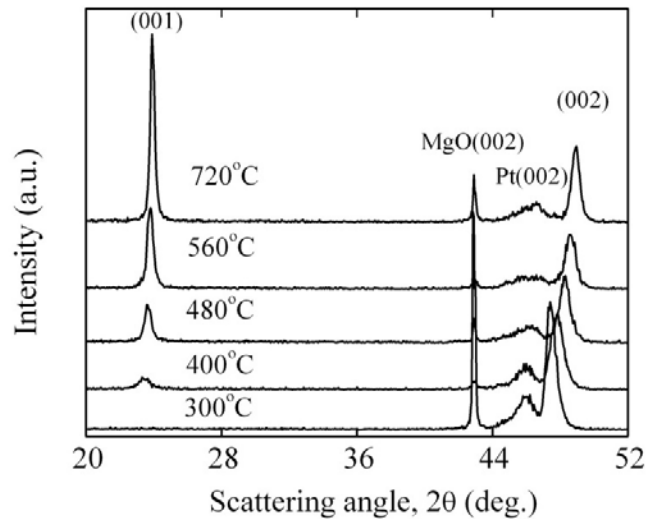


Fig. 6.2. X-ray diffraction spectra of samples deposited at different temperatures.

Fig. 6.3 shows the dependence of the order parameter S and the lattice constant c on growth temperature, T_g . With an increase in T_g , the order parameter increases. At 300°C, the film is chemically disordered and epitaxial. The maximum growth temperature of 700°C is a limit imposed by the sample heater in the deposition system. It is possible that the films may undergo an order-disorder transition at even higher temperatures which would be accompanied by a decrease in chemical order parameter. The c-axis lattice parameter is reduced as the $Fe_{50}Pt_{50}$ transforms from the chemically disordered fcc phase to the chemically-ordered $L1_0$ phase.

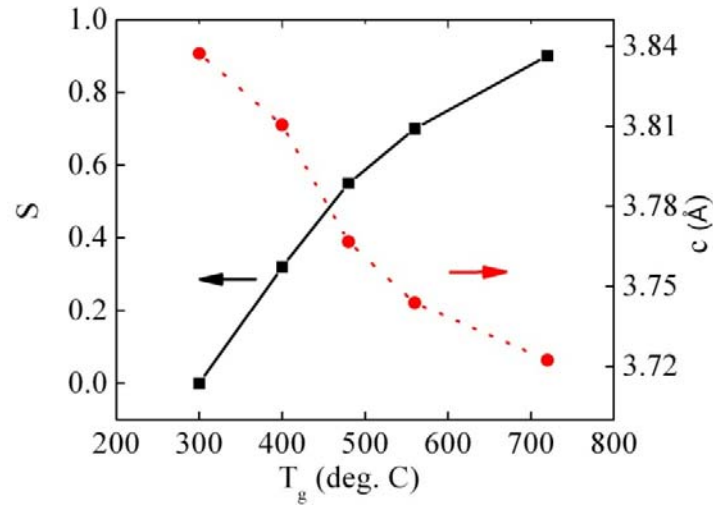


Fig. 6.3. Dependence of the order parameter S and the lattice constant c on the growth temperature T_g .

Epitaxial films

To confirm that all films were epitaxially grown on MgO substrates, (111) pole figures of the films were measured. Both MgO and FePt have four-fold symmetry and a similar lattice constant a , so if the FePt film epitaxially grows on the MgO (100) substrate, the (111) peaks should appear at exactly the same ϕ angle when we do a ϕ scan.

Fig. 6.4 shows the ϕ scans for a MgO substrate and a Fe₅₀Pt₅₀ film with $S=0.9$. From the pole figures, we confirm that both MgO and Fe₅₀Pt₅₀ have four-fold symmetry. The peaks of the film appear exactly at the same ϕ angle as those of the MgO substrate.

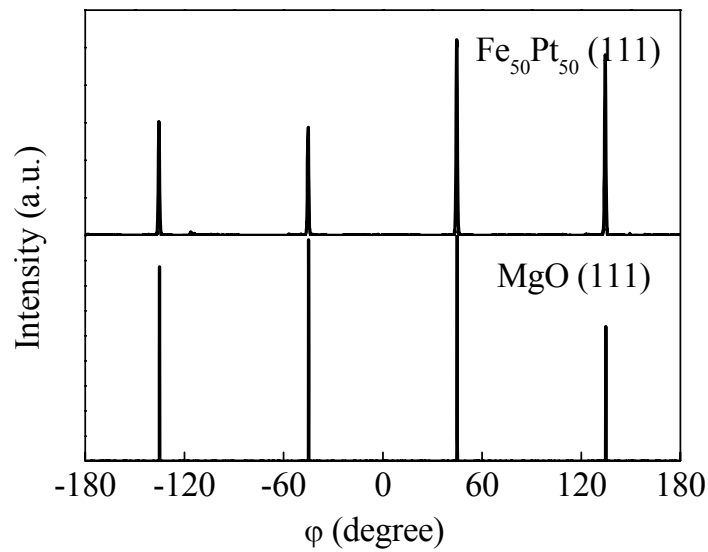


Fig. 6.4. (111) pole figures of the Fe₅₀Pt₅₀ film and MgO substrate.

Rocking curve dependence on growth temperature

Ordered Fe₅₀Pt₅₀ has an easy axis along the (001) direction, therefore, for application in perpendicular magnetic recording, the dispersion of easy axes is mainly determined by the dispersion of the crystal orientation. To check the dispersion of a c-axis in the films, we measure the rocking curve of the (001) peak of the film and determine the dispersion of the orientation by measuring the full width at half maximum (FWHM). The dependence of FWHM on growth temperature is shown in Fig. 6.5. The FWHM of the films is at a range of 1-2°, which means that our films have very good (001) orientation. The FWHM increases with an increase of temperature. This is mainly due to the enhancement of diffusion at the interface with the increase of temperature.

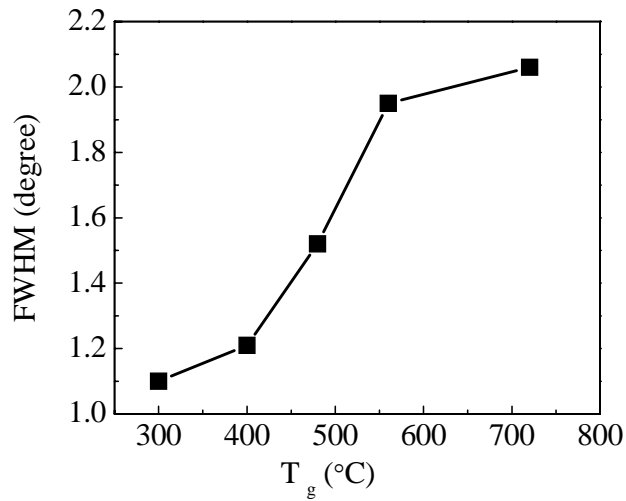


Fig. 6.5. Dependence of FWHM on the growth temperature.

Magnetic properties

The magnetic properties change with changes in the order parameter S . The easy and hard axis loops of each film are shown in Fig. 6.6. The magnetization M_s of all the films is near $1100 \pm 100 \text{ emu/cc}$, which coincides with the value of bulk $L1_0$ phase $\text{Fe}_{50}\text{Pt}_{50}$ [87]. The change in S does not lead to significant changes in M_s . This property is quite important for us because the linear energy landscape is obtained on the condition that M_s remains constant in all the layers. The films with $S > 0.3$ have an out-of-plane easy axis and the bow-type easy axis loops indicating that domain wall motion is involved in the switching due to the relatively large thickness. The hard axis loop of these films has a small coercivity that is likely to be caused by the mixture of ordered and disordered phases. By comparing the hard axis loops of the films with $S > 0.3$, we find that, with the increase of S , the hard axis loops require a larger applied magnetic field to be saturated. The maximum 1.8 T magnetic field is not high enough to saturate the hard axis loops of films with $S > 0.5$. Although we cannot derive the switching field H_k directly from unsaturated

hard axis loops, we can estimate H_k by extrapolation. The estimated H_k values of films with $S=0.9, 0.7, 0.5$ and 0.32 are equal to $70 \text{ kOe}, 46 \text{ kOe}, 27 \text{ kOe}$ and 17.8 kOe , respectively.

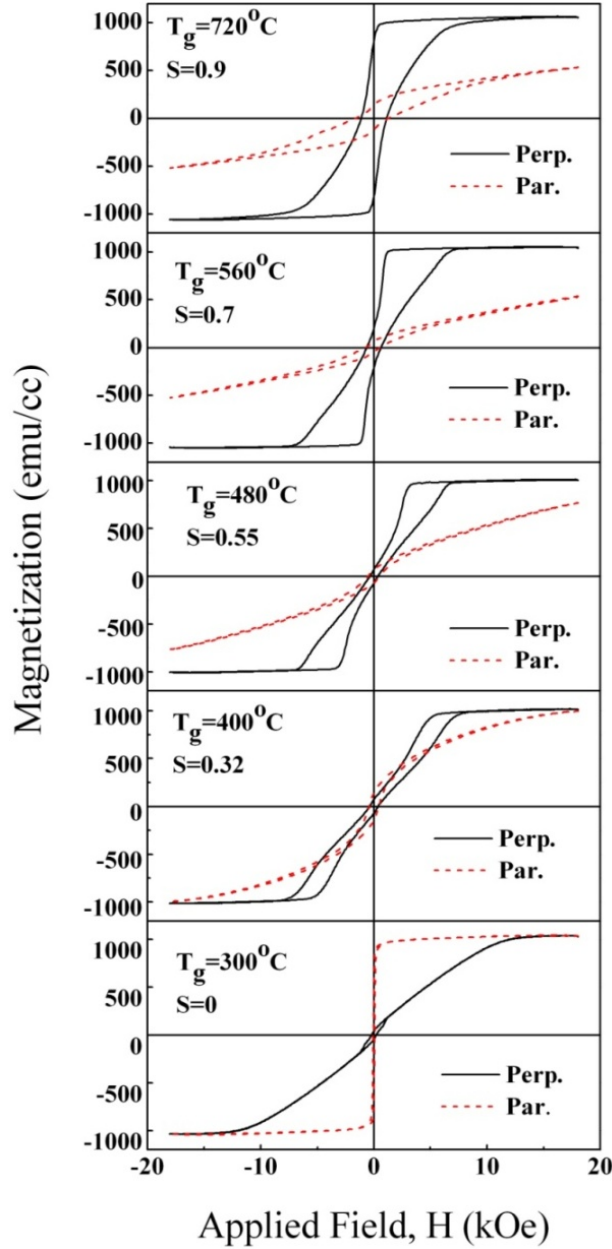


Fig. 6.6. Magnetic properties of $\text{Fe}_{50}\text{Pt}_{50}$ films deposited at different growth temperatures.

After taking the demagnetizing field into account, the anisotropy of films can be roughly estimated by $K_u = \frac{1}{2} M_s H_k + 2\pi M_s^2$. So K_u for the films with $S=0.9, 0.7, 0.5$ and 0.32 are

$4.6 \times 10^6 \text{ J/m}^3$, $3.3 \times 10^6 \text{ J/m}^3$, $2.2 \times 10^6 \text{ J/m}^3$ and J/m^3 , respectively. With the decrease of S , magnetic anisotropy of $\text{Fe}_{50}\text{Pt}_{50}$ thin film decreases. Fig. 6.7 shows the change of anisotropy with the chemical order parameter S .

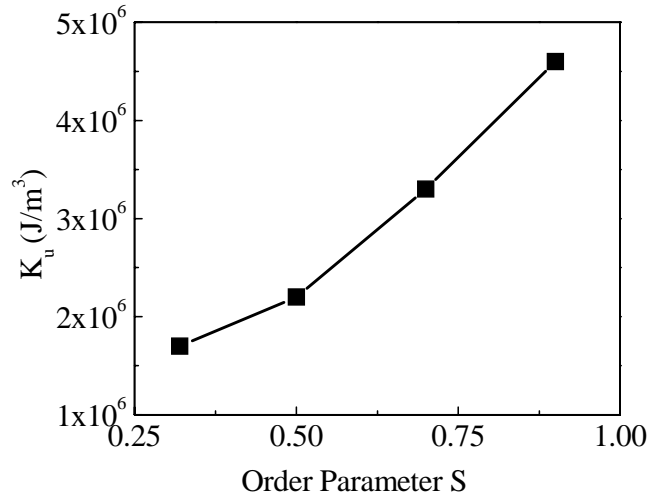


Fig. 6.7. Dependence of magnetic anisotropy on the order parameter.

The completely disordered film has soft magnetic properties with an in-plane easy axis, and an H_k ($\sim 12.4 \text{ kOe}$) derived from the out-of-plane loop almost equal to the demagnetizing field ($\sim 13 \text{ kOe}$).

For the application of multilayer exchanged composite media and anisotropy graded media, it is desirable for the material of each layer to have perpendicular anisotropy. According to the results shown above, $\text{Fe}_{50}\text{Pt}_{50}$ films with S greater than 0.32 are suitable for this application. It needs to be mentioned that the films considered are continuous films that have large demagnetizing fields ($\sim 13 \text{ kOe}$). The effect of the demagnetizing fields is to make the moment in-plane. Thus, the demagnetizing fields are equivalent to an in-plane anisotropy with a magnitude of $6 \times 10^5 \text{ J/m}^3$. A film shows a perpendicular easy axis only when its perpendicular crystalline anisotropy is larger than $6 \times 10^5 \text{ J/m}^3$. Therefore, films with an order parameter lower

than 0.32 may also have perpendicular crystalline anisotropy. The reason for their having an in-plane easy axis is that their anisotropy fields are smaller than their demagnetizing fields. In practice, a recording medium is made of a large amount of separated grains instead of a continuous film. Its recording properties are determined by the individual grains. Typically, the grain size in a medium is on the order of tens of nanometers in diameter. At this size, the demagnetized field in a grain should be much smaller than in a continuous film. Therefore, a much smaller perpendicular anisotropy may be enough to lead to a perpendicular easy axis in a grain. For this reason, a chemical order parameter smaller than 0.3 may also be useful in fabricating anisotropy graded media, which means we can make the soft end of the graded media even softer.

6.3 Structures and Magnetic Properties of $\text{Fe}_{50}\text{Pt}_{50}$ Thin Films with Graded Order Parameters

The magnetic anisotropy of a uniform $\text{Fe}_{50}\text{Pt}_{50}$ film changes with order parameter S . This can be controlled by varying the growth temperature. Thus, by changing the growth temperature during deposition, we can make the anisotropy change along the thickness of the film.

By depositing $\text{Fe}_{50}\text{Pt}_{50}$ at four different temperatures, we made a $\text{Fe}_{50}\text{Pt}_{50}$ film stacked with layers of four different anisotropies. Fig. 6.8 shows the structure of the sample. Each $\text{Fe}_{50}\text{Pt}_{50}$ layer was deposited at the design temperature. During the change of temperature, the shutter was closed. Deposition did not begin until the temperature became stable ($\pm 10^\circ$) around the design temperature.

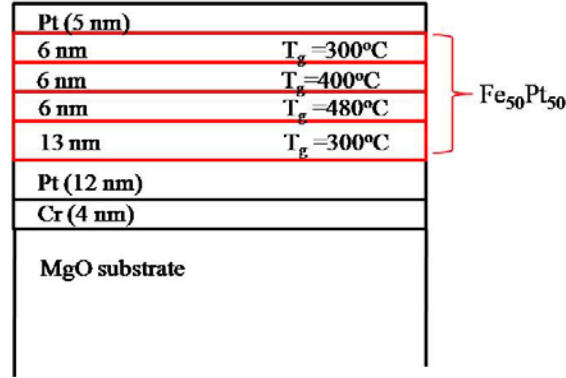


Fig. 6.8. Structure of the sample stacked with 4 Fe₅₀Pt₅₀ layers deposited at different T_gs.

The X-ray diffraction spectrum of the sample is shown in Fig. 6.9. In the spectrum, the Fe₅₀Pt₅₀ (002) peak, the Pt (200) peak, and the Cr (200) and MgO (200) peaks overlap each other. To accurately determine the order parameters, we need to separate these peaks. This can be achieved by fitting them with Lorentz functions. The fits (red) and the deconvolved peaks (green) are also shown in Fig. 6.9. The order parameter determined by the intensity ratio of the (001) and (002) peaks is 0.58. Since the sample was stacked with four layers, each layer has a different order parameter. The order parameter determined from X-ray diffraction is actually an average of the order parameters of all these four layers. According to our former results, the order parameters for Fe₅₀Pt₅₀ films deposited at 300°, 400°C, 480° and 700° are 0, 0.33, 0.55 and 0.9 respectively. The average order parameter can be calculated by the following equation:

$$S = t^{-1} \sum_i t_i \cdot S_i \quad (6.14)$$

where t is the total Fe₅₀Pt₅₀ thickness; t_i and S_i are the thickness and order parameter of i layer respectively.

The order parameter directly calculated by using Eq. 6.15 is 0.55. This value is very close to what we obtained by X-ray diffraction ($S=0.58$), which means the order parameter of each Fe₅₀Pt₅₀ layer is similar to that of a uniform film deposited at the same temperature.

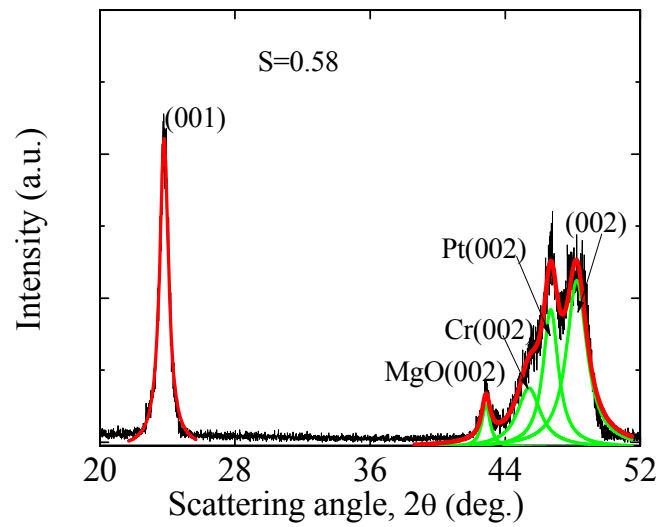


Fig. 6.9. X-ray diffraction spectrum and peak analysis.

The magnetic properties of the sample are shown in Fig. 6.10. The saturation magnetization is still about 1200 emu/cc, almost the same as that of a uniform $\text{Fe}_{50}\text{Pt}_{50}$ film, which confirms that the saturation magnetization of $\text{Fe}_{50}\text{Pt}_{50}$ does not depend strongly on order parameter S . The film has an easy axis perpendicular to the plane. By extrapolating the hard axis loop, we can estimate the switching field to be 45 kOe. This is much less than in a uniform film deposited at 700 °C, which has a switching field of about 70 kOe.

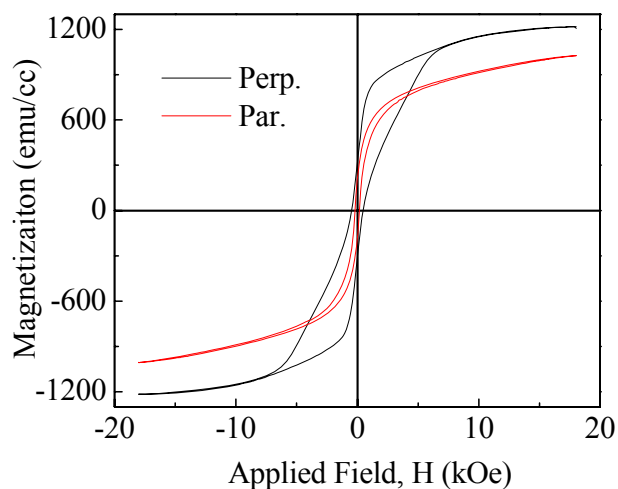


Fig. 6.10. Magnetic properties of the sample with $\text{Fe}_{50}\text{Pt}_{50}$ layers deposited at 4 different T_g s.

Since the anisotropy of $\text{Fe}_{50}\text{Pt}_{50}$ films monotonically decreases with the order parameter, we can decrease anisotropy more gradually by continuously changing the growth temperature.

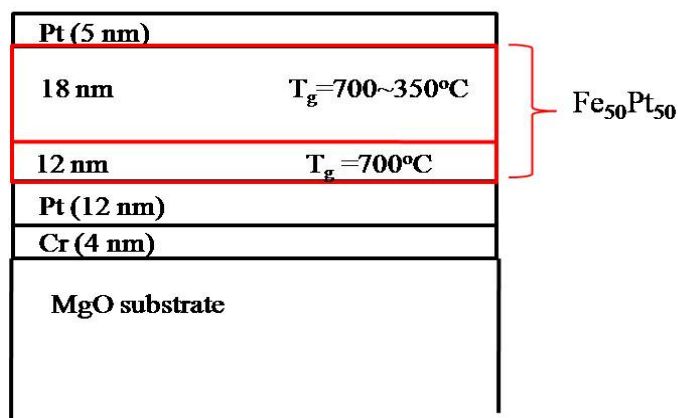


Fig. 6.11. Structure of the sample stacked with $\text{Fe}_{50}\text{Pt}_{50}$ layers deposited at a continuously decreased temperature.

Fig. 6.11 shows the structure of a sample with the growth temperature continuously decreased from 700 to 350°C. The changing of temperature is carried out by manually decreasing the applied voltage of the sample heater without stopping the sputtering process. Since the decrease rate of the temperature cannot be controlled uniformly, the thickness of

$\text{Fe}_{50}\text{Pt}_{50}$ deposited at each temperature is not known. Thus, we cannot estimate the order parameter of this sample by using Eq. 6.15.

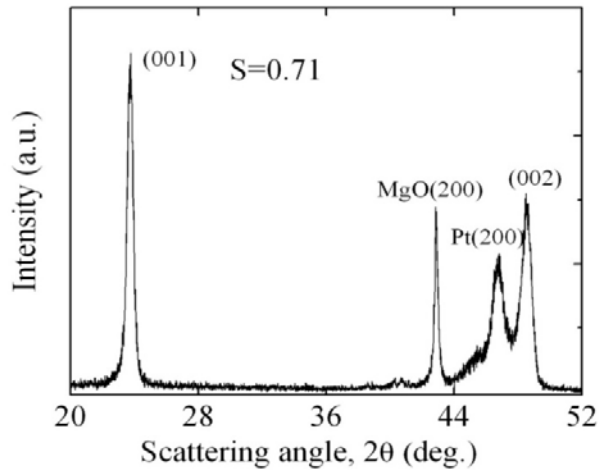


Fig. 6.12. X-ray diffraction spectrum of the sample stacked with $\text{Fe}_{50}\text{Pt}_{50}$ layers deposited at a continuously decreased temperature.

Fig. 6.12 shows the X-ray diffraction pattern of the sample with $\text{Fe}_{50}\text{Pt}_{50}$ deposited at a continuously changed temperature. The peaks are less overlapped than those in the sample stacked with four layers of $\text{Fe}_{50}\text{Pt}_{50}$. By using the same method described before, we separated the peaks and got the order parameter to be about 0.7.

The hysteresis loops of the sample are shown in Fig. 6.13. The easy axis of the sample is perpendicular to the film surface. The switching field obtained by extrapolation of the hard axis loop is about 37 kOe. This value is even smaller than that of the sample stacked with four $\text{Fe}_{50}\text{Pt}_{50}$ layers deposited at different temperatures.

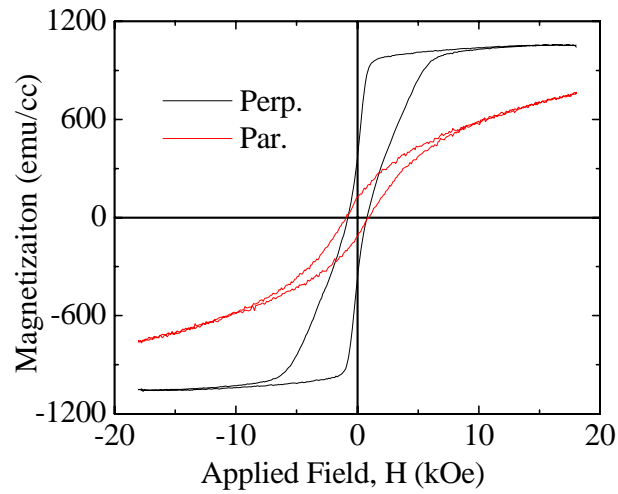


Fig. 6.13. Magnetic properties of the sample stacked with $\text{Fe}_{50}\text{Pt}_{50}$ layers deposited at a continuously decreased temperature.

Conclusions

The anisotropy of $\text{Fe}_{50}\text{Pt}_{50}$ can be controlled by varying the growth temperature. The chemical order parameter, S , and the magnetic anisotropy K_u increase with increasing growth temperature. Moreover, the saturation magnetization of $\text{Fe}_{50}\text{Pt}_{50}$ does not change with order parameter. The magnetic properties of $\text{Fe}_{50}\text{Pt}_{50}$ films with graded order parameters are studied. It is found that films with graded ordered parameters have a much smaller switching field than fully ordered uniform $\text{Fe}_{50}\text{Pt}_{50}$ film. Graded $\text{Fe}_{50}\text{Pt}_{50}$ films are very promising in the fabrication of graded media.

CHAPTER 7 MAGNETIC PROPERTIES OF EPITAXIAL $\text{Fe}_{100-x}\text{Pt}_x$ (001) UNIFORM FILMS AND MULTILAYERS

Introduction

Although fully ordered $L1_0$ phase equiatomic FePt alloy has an extremely large magnetocrystalline anisotropy, it is hard to write. To decrease the coercivity, the magnetic properties of $\text{Fe}_{100-x}\text{Pt}_x$ with $x \neq 50$ have also been studied [88, 89]. It was found that the anisotropy of FePt films also depends on the film composition, which suggests that the anisotropy of FePt can be tuned by composition as well as the order. Previous studies show that, $\text{Fe}_{100-x}\text{Pt}_x$ (001) thin films show perpendicular anisotropy with x in the range of 45-70 [90-92] and the anisotropy decreases with the increase of $|x - 50|$.

In this chapter, we will examine the dependence of the magnetic properties of Fe-rich ordered $\text{Fe}_{100-x}\text{Pt}_x$ (001) uniform films on composition. Based on this, we will discuss the possibility of building magnetic anisotropy graded media with $\text{Fe}_{100-x}\text{Pt}_x$ with different x .

7.1 Sample Preparation

Sample Fabrication

All samples were deposited at 600-700°C on MgO(100) substrates which were degassed at 750°C. The degassing period lasted for more than 30 min until the base pressure was reduced to less than 5×10^{-8} torr.

The process for the deposition of Cr (4nm) and Pt(12nm) was the same as described in the last chapter. The deposition of the $\text{Fe}_{100-x}\text{Pt}_x$ layer was performed by co-sputtering with a

pure Fe target and a Fe₅₀Pt₅₀ alloy target. The sputtering rate for each target depended on the stoichiometry of the film.

Composition design

To fabricate Fe_{100-x}Pt_x films by co-sputtering with a pure Fe target and a Fe₅₀Pt₅₀ alloy target, the sputtering rate of each target needs to be determined. To do that, the dependence of the ratio of sputtering rates on the film composition should be derived

For a given material, after t seconds of sputtering, the weight (W) of the film will be

$$W = \rho \times R \times t \times S \quad (7.1)$$

where ρ and R are the density and the deposition rate of the material respectively; t is the sputtering time and S is the area of the film.

The mole number N can then be calculated by using weight (W) and atomic weight (M),

$$N = \frac{W}{M} \quad (7.2)$$

The number of Pt and Fe atoms can be obtained by using Avogadro's constant times the mole number N . Since a 2-atom cell of FePt contributes one Fe atom and one Pt atom, after t seconds of co-sputtering, the total number of Pt atoms and Fe atoms will be

$$n_{Pt} = C_A \times W_{FePt} / M_{FePt} \quad (7.3)$$

and

$$n_{Fe} = C_A (W_{FePt} / M_{FePt} + W_{Fe} / M_{Fe}) \quad (7.4)$$

where n_{Fe} and n_{Pt} are the number of Fe and Pt atoms; M_{Fe} and M_{FePt} are the atomic weights of Fe and of FePt respectively and C_A is Avogadro's constant. Thus the ratio of Fe and Pt should be

$$n_{Fe} / n_{Pt} = 1 + (W_{Fe} / M_{Fe}) / (W_{FePt} / M_{FePt}) \quad (7.5)$$

After substituting Eq. 7.1 for atom weights (M_{Fe} and M_{FePt}) in 7.4, the dependence of the atom ratio between Fe and Pt on the sputtering rates of FePt and Fe can be expressed as

$$n_{Fe}/n_{Pt} = 1 + (\rho_{Fe}R_{Fe}/M_{Fe})/(\rho_{FePt}R_{FePt}/M_{FePt}) \quad (7.6)$$

where ρ_{Fe} and ρ_{FePt} are the densities of Fe and FePt.

For the deposition of a $Fe_{100-x}Pt_x$ film, the atom ration should be

$$n_{Fe}/n_{Pt} = (100 - x)/x = 1 + (\rho_{Fe}R_{Fe}/M_{Fe})/(\rho_{FePt}R_{FePt}/M_{FePt}) \quad (7.7)$$

Therefore, the ratio of sputtering rate of Fe and $Fe_{50}Pt_{50}$ should be

$$R_{Fe}/R_{FePt} = ((100 - 2x)/x) \times (M_{Fe}/M_{FePt}) \times (\rho_{FePt}/\rho_{Fe}) \quad (7.8)$$

Sputtering power determination

To deposit a film with designed composition, the sputtering power for each target needs to be calculated. Therefore, the relation between the sputtering rate and the applied powers for Fe and $Fe_{50}Pt_{50}$ has to be found. For pure Fe, a quartz crystal microbalance can be used to directly measure the sputtering rate at different powers. For $Fe_{50}Pt_{50}$ alloy, since its Z factor, a factor used to match the acoustic impedance of deposited material to that of the base quartz sensor material, is not known, the sputtering rate can not be characterized by using a quartz crystal microbalance. To find out the relation between the sputtering rate and the sputtering power, a series of films need to be deposited at different powers. For a given film, after the measurement of its X-ray reflectivity (XRR) spectrum, the thickness can be determined by fitting the XRR spectrum with the software package WinGixa. The sputtering rates can be calculated by dividing the thickness by the sputtering time. The sputtering rates of Fe and $Fe_{50}Pt_{50}$ are shown in Fig. 7.2 (a) and (b), respectively. The rates of both materials depend nearly linearly on the applied power in given ranges. By using a linear fitting, the relation between sputtering rate and applied power for both materials can be expressed as:

$$R_{FePt} = 0.03P \quad 10w < P < 40w \quad (7.9)$$

$$R_{Fe} = 0.004P - 0.01 \quad 30w < P < 90w \quad (7.10)$$

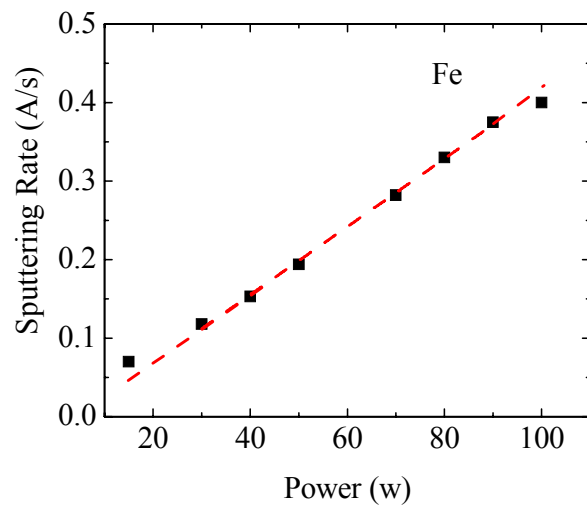
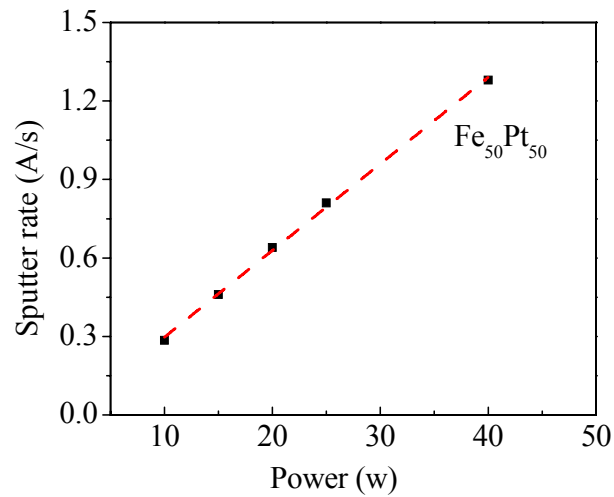


Fig .7.1. Dependence of sputtering rate on sputtering power.

where P represents the applied power. By using these equations, the sputtering rate for each material can be determined, and corresponding applied power can thus be obtained accordingly. For safety, the applied powers should be kept within the indicated ranges because the linear

relations only hold in those ranges. Table 7.1 shows the sputtering rates and powers for materials relating to the designed composition.

Table 7.1. Sputtering rates and powers of Fe and Fe₅₀Pt₅₀ for co-sputtering of Fe_{100-x}Pt_x.

Fe _{100-x} Pt _x	R _{Fe} /R _{FePt}	Fe ₅₀ Pt ₅₀ rate (Å/s)	Fe rate (Å/s)	Fe ₅₀ Pt ₅₀ Power (W)	Fe Power (W)	Fe _{100-x} Pt _x rate (Å/s)
Fe ₅₀ Pt ₅₀	0	0.645	0	20	0	0.
Fe ₅₅ Pt ₄₅	0.095	0.645	0.062	20	15*	071
Fe ₆₀ Pt ₄₀	0.215	0.645	0.14	20	35	0.79
Fe ₆₇ Pt ₃₃	0.44	0.645	0.284	20	74	0.93
Fe ₇₅ Pt ₂₅	0.856	0.286	0.245	10	60	0.531
Note: * this power is determined directly from measurement, not by Eq. 7.9						

7.2 Structures and Magnetic Properties of Uniform Fe_{100-x}Pt_x (x≥33) Films

By using the sputtering powers determined above, we can make uniform Fe_{100-x}Pt_x thin films samples. The sample structure is shown in Fig .7.2.

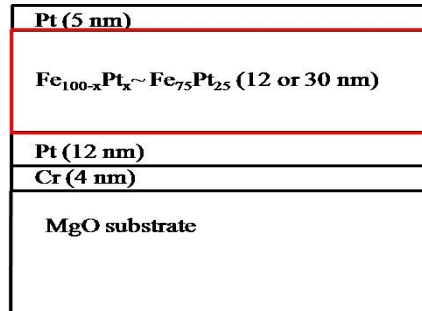


Fig. 7.2. Structure of uniform Fe_{100-x}Pt_x (x≥33) thin films.

Fig. 7.3 shows the XRD pattern of Fe_{100-x}Pt_x films with x =50, 45, 40, 33. All of these films show the (001) superlattice peak. The films with the highest Fe ratio have a broad (001) peak compared with other films and a very broad (002) peak. This is most likely due to the coexistence of different phases and orientations in extremely Fe rich films.

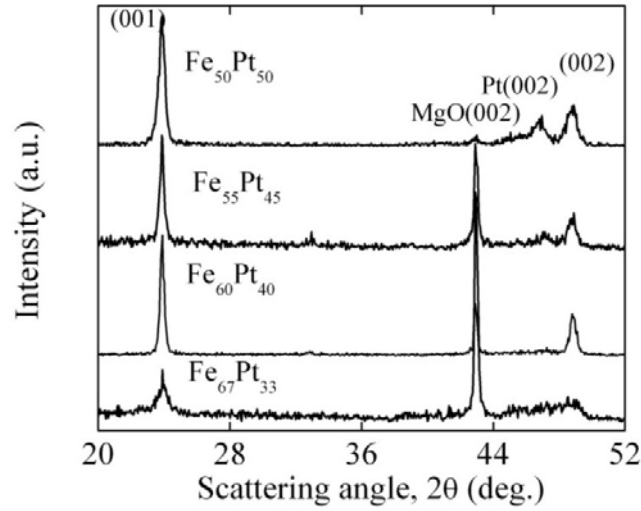


Fig. 7.3 X-ray diffraction patterns of $\text{Fe}_{100-x}\text{Pt}_x$ films.

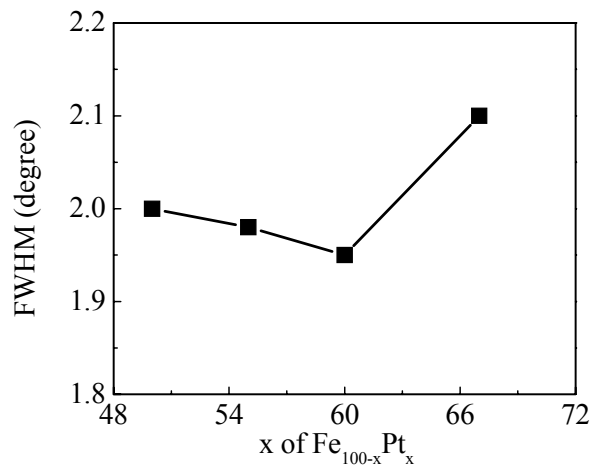


Fig. 7.4. Dependence of FWHM of (001) peak on the composition of $\text{Fe}_{100-x}\text{Pt}_x$ films.

The rocking curves (001) of the films were measured to study the orientation dispersion. The full width at half maximum (FWHM) of (001) for each sample is shown in Fig. 7.4. For all the samples, the FWHMs are quite close and approximately 2 degrees, which suggests that all the samples have good a (001) orientation and the dispersion is very small (about $\pm 1^\circ$).

Magnetic properties

The magnetic properties of the films are shown in Fig. 7.5. For the films with an Fe atom ratio up to 60%, the easy axis is still out of plane. However, as the Fe composition increases, the hard axis coercivity increases. Since the X-ray rocking curve analysis did not show an increase in c-axis dispersion nor does the the X-ray diffraction pattern of these films show any apparent in-plane c-axis variants, the dispersion of the c-axis is not likely the main reason for the broad hard axis loops. In general, the anisotropy energy for a magnetic material with a uniaxial anisotropy is given by

$$E(\theta) = K_1 \sin^2 \theta + K_2 \sin^4 \theta + \dots \quad (7.11)$$

with θ representing the angle between magnetic moment and the easy axis, K_1 and K_2 represent the first order and second order anisotropy energies, respectively. However, in many applications, only K_1 is considered, the effect of K_2 is neglected. This causes no problem in most cases, because usually K_2 is quite small compared to K_1 . However, when K_2 is not small, neglecting of K_2 is not valid. A large K_2 ($K_2 > K_1$) was found by Nahid *et al.* [93] in ordered Fe₇₅Pt₂₅ film, which can lead to a tilting of the easy axis. A careful study of the easy axis loops with x=55 and x=50, shows that the loops are not completely flat, which suggests that the perpendicular direction may not correspond to easy axis. The film with x=67 shows almost isotropic magnetic properties. Various factors such as mixture of phases, variation of orientations and the tilting of the easy axis by a large K_2 can cause this effect. To investigate the real reason, it is helpful to make films with x=75 and to compare their magnetic properties with those of the film with x=67.

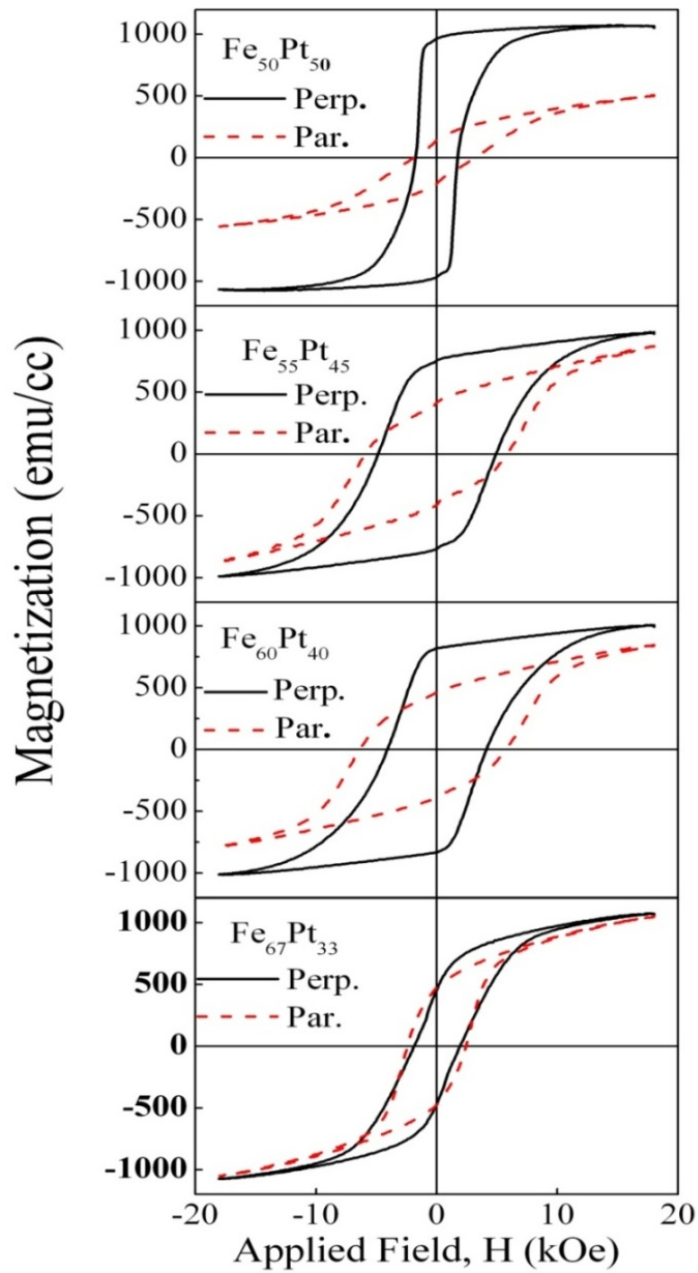


Fig. 7.5. Magnetic properties of Fe_{100-x}Pt_x films.

7.3 Structures and Magnetic Properties of Uniform Fe₇₅Pt₂₅ Films

Two Fe₇₅Pt₂₅ films were made at different growth temperatures (T_g) with 12 nm thickness. One was deposited at 400°C, the other was deposited at 600°C. As we know, Fe₇₅Pt₂₅ will have L1₂ structure when it is chemically ordered and will have face-centered cubic (fcc) structure when it is chemically disordered. By using X-ray diffraction, we can determine the order parameter of Fe₇₅Pt₂₅.

To determine the order parameter of Fe₇₅Pt₂₅, we need to calculate the peak intensity ratio for a fully ordered Fe₇₅Pt₂₅ film with certain thickness first. This can be performed by using the method described in chapter 5.

Since, the crystal structure of Fe₇₅Pt₂₅ is different from that of Fe₅₀Pt₅₀, its structure factors will also differ from those of Fe₅₀Pt₅₀, and can be expressed as:

$$F = \begin{cases} 3f_{Fe}e^{-W_{Fe}} + f_{Pt}e^{-W_{Pt}} & \text{for (002) peak} \\ f_{Pt}e^{-M_{Pt}} - f_{Fe}e^{-M_{Fe}} & \text{for (001) peak} \end{cases} \quad (7.12)$$

Thus $|F|^2$ can be expressed as

$$|F|^2 = \begin{cases} [(3r_{Fe}e^{-W_{Fe}} + r_{Pt}e^{-W_{Pt}})^2 + (3\Delta_{Fe}e^{-W_{Fe}} + \Delta_{Pt}e^{-W_{Pt}})^2] & \text{(002) Peak} \\ [(r_{Pt}e^{-W_{Pt}} - r_{Fe}e^{-W_{Fe}})^2 + (\Delta_{Pt}e^{-W_{Pt}} - \Delta_{Fe}e^{-W_{Fe}})^2] & \text{(001) peak} \end{cases} \quad (7.13)$$

The parameters used for calculating the peak intensity of a fully ordered Fe₇₅Pt₂₅ with thickness of 12 nm are shown in Table 7.2.

Table 7.2. Parameters for the calculations of peak intensities of fully ordered Fe₇₅Pt₂₅.

Peak	2θ	LP	W_{Fe}	r_{Fe}	Δ_{Fe}	W_{Pt}	r_{Pt}	Δ_{Pt}	G_t
(001)	23.7	4.57	0.005	21.01	3.4	0.005	64.43	8	0.0325
(002)	48.5	1.921	0.019	16.93	3.3	0.041	45.81	7	0.0161

By using these parameters, we obtained the calculated peak intensity ratio for a fully ordered 12 nm Fe₇₅Pt₂₅ film to be

$$\left(\frac{I_{001}}{I_{002}}\right)_{cal}^{S=1} = 0.83$$

Therefore, we can determine the order parameter of Fe₇₅Pt₂₅ film by using Eq. 6.1 when we get the experimental peak intensity ratio from X-ray diffraction.

Fig. 7.6 shows the X-ray diffraction patterns for Fe₇₅Pt₂₅ films deposited at different temperatures. The film deposited at 400°C is close to fully disordered with a tiny (001) peak. The estimated order parameter S is smaller than 0.1. When the growth temperature goes to 600°C, Fe₇₅Pt₂₅ becomes ordered with order parameter S~0.85. With the increase of growth temperature, the lattice constant c increases. Lattice constant c is 3.67 Å for disordered Fe₇₅Pt₂₅ and becomes 3.75 for ordered Fe₇₅Pt₂₅.

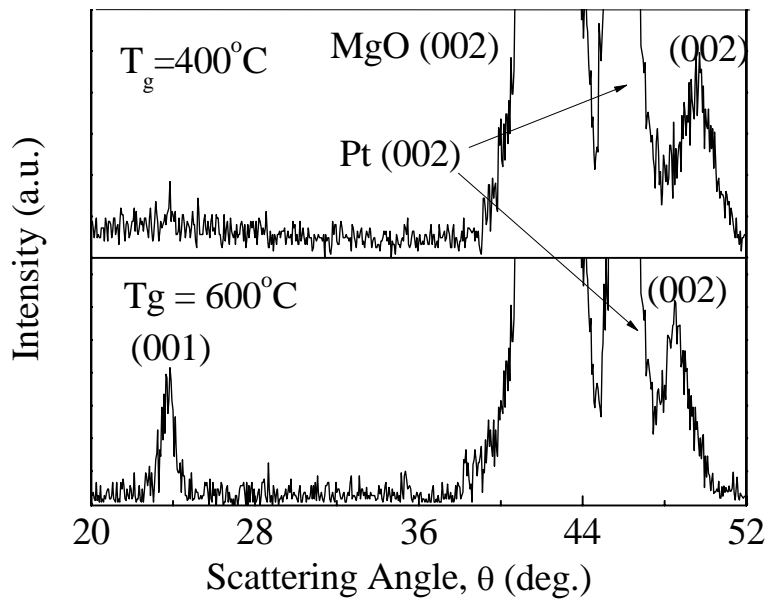


Fig. 7.6. X-ray diffraction spectra of Fe₇₅Pt₂₅ films deposited at 400°C and 600°C.

The magnetic properties of $\text{Fe}_{75}\text{Pt}_{25}$ highly depend on its phase. For disordered $\text{Fe}_{75}\text{Pt}_{25}$, the easy axis is in the film plane. For ordered $\text{Fe}_{75}\text{Pt}_{25}$, the in-plane and out-of-plane loops are nearly identical. Comparing the magnetic properties of the ordered $\text{Fe}_{75}\text{Pt}_{25}$ film with those of the $\text{Fe}_{67}\text{Pt}_{33}$ film, we find that the in-plane hysteresis loop is quite similar to the out of plane hysteresis loop for both films. The loops of $\text{Fe}_{75}\text{Pt}_{25}$ are more nearly identical than those of the $\text{Fe}_{67}\text{Pt}_{33}$ film. Since we already know that $\text{Fe}_{75}\text{Pt}_{25}$ has a tilted easy axis due to a large negative K_2 , we can conclude that the isotropic magnetic properties of the film with $x=67$ is most likely due to the large negative K_2 . The large coercivity of the hard axis loops of other Fe-rich films may be also, at least partially, due to the same reason. The magnetization of $\text{Fe}_{75}\text{Pt}_{25}$ is about 1700 emu/cc which is much higher than that of $\text{Fe}_{50}\text{Pt}_{50}$.

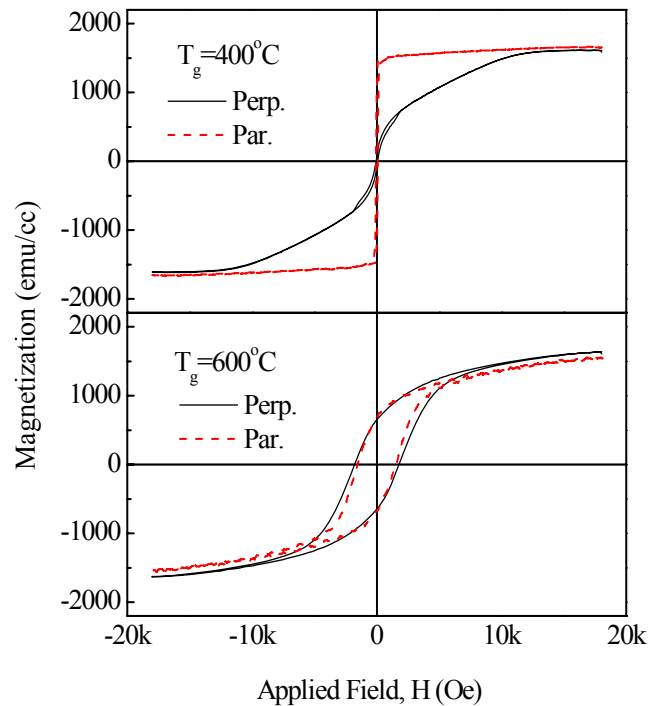


Fig. 7.7. Magnetic properties of $\text{Fe}_{75}\text{Pt}_{25}$ thin films deposited at 400°C and 600°C .

For an application as recording media, a large K_2 is not desirable because it will make things more complicated by introducing another variant. Moreover, the sign of K_1 and K_2 can be different, which may lead to a tilted easy axis. Since the value and sign of K_1 and K_2 depend on the fabrication process and condition, to control the magnetic anisotropy value by changing composition, more effort is needed to optimize the fabrication process for decreasing the effect of K_2 .

7.4 Magnetic Properties of $\text{Fe}_{100-x}\text{Pt}_x$ Films with Graded Compositions ($25 \leq x \leq 50$)

After studying the magnetic properties of uniform films, the magnetic properties of films stacked with $\text{Fe}_{100-x}\text{Pt}_x$ layers where x changes monotonically were studied. Two kinds of stacked films were fabricated and the structures of both samples are shown in Fig. 7.8. In both samples, the bottom $\text{Fe}_{100-x}\text{Pt}_x$ layer is 12 nm $\text{Fe}_{50}\text{Pt}_{50}$. In sample a, three layers of $\text{Fe}_{100-x}\text{Pt}_x$ with $x = 40, 33$ and 25 were stacked on $\text{Fe}_{50}\text{Pt}_{50}$ layer with a thickness of 6 nm for each. In sample b, the composition x of layers stacked on $\text{Fe}_{50}\text{Pt}_{50}$ was continuously changed from $x=50$ to 25 by manually decreasing the applied power of the Fe target.

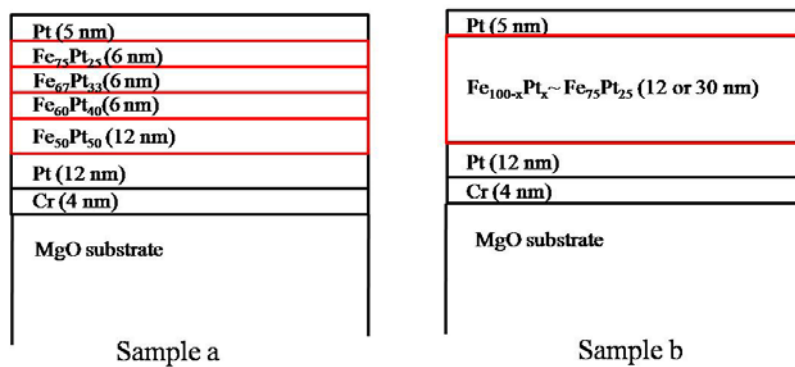


Fig. 7.8. Structures for samples with graded compositions.

Fig. 7.9 shows the X-ray diffraction patterns and magnetic properties of both samples. Both samples show a very good (001) orientation with only the (001) and the (002) peaks appearing. The hysteresis loops show that sample b has an easy axis almost along the perpendicular direction. As for sample a, although the hysteresis loop is more easily to saturate

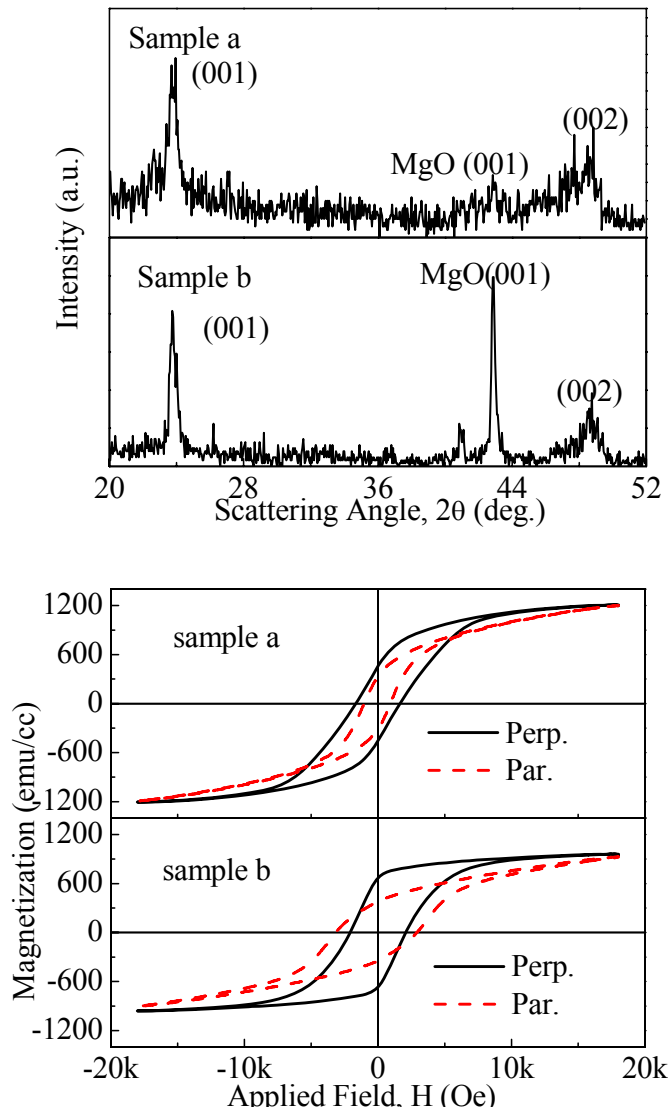


Fig. 7.9. X-ray diffraction spectra and magnetic properties of samples with graded compositions.

when the applied field is perpendicular to the film, its easy axis is apparently tilted a larger angle from the direction of the surface normal than that of sample b.

Large coercivities in hard axis loops make it impossible to estimate H_k from the hard axis loop for both samples. In this situation, it is hard to know if the compositional gradient of the film can be helpful in decreasing the switching field.

Conclusions

By studying the magnetic properties of $\text{Fe}_{100-x}\text{Pt}_x$ films, we found that two reasons make $\text{Fe}_{100-x}\text{Pt}_x$ not promising in graded media application:

1) The hard axis loops of epitaxial $\text{Fe}_{100-x}\text{Pt}_x$ films have a large coercivity. One of the reasons might be that, with the increase of Fe composition, the easy axes of the films tilt at some angle from the surface normal due to a large negative K_2 . The tilting of the easy axis of $\text{Fe}_{100-x}\text{Pt}_x$ films will lead to a large easy axis dispersion which is not desirable for making graded media. To avoid the tilting of the easy axis, further investigations on the dependence of the magnetic properties of $\text{Fe}_{100-x}\text{Pt}_x$ on the fabrication process and the seed layer selection are needed.

2) The magnetization of $\text{Fe}_{100-x}\text{Pt}_x$ changes with x , which leads to another set of variables for graded media fabrication.

CHAPTER 8 MAGNETIC STRUCTURE OF FePt₃ AND SELF-EXCHANGE BIAS IN FePt₃(ORDERED)/FePt₃ (DISORDERED) SUPERLATTICES

Introduction

FePt₃ is a material which has the remarkable property that, depending on the degree of chemical order, a ferromagnetic (FM) and an antiferromagnetic (AF) state can coexist at the same temperature. Direct magnetic exchange coupling at the interface between an antiferromagnet and a ferromagnet can result in a shift of the magnetic hysteresis curve along the field axis. This exchange bias effect (for recent reviews, see [94-96]) essentially is a magnetic pinning effect leading to a unidirectional anisotropy. If an FM/AF interface sample is cooled in an external magnetic field from a temperature below the Curie temperature T_C of the FM through the Néel temperature T_N of the AF ($T_C > T_{\text{start}} > T_N \Rightarrow T_C > T_N > T_{\text{end}}$), the interfacial AF spins may align in a preferential orientation relative to the FM spins as the AFM order sets in. If subsequently, after completion of the cooling process, the direction of the external field is reversed, the AF/FM interface spins exert a torque on reversing FM interface spins which effectively stabilizes their field-cooled direction. Macroscopically, the exchange bias effect leads to an offset of the center of the hysteresis loop by an amount called the exchange bias field.

In recent years, significant research efforts were aimed at exploring the exchange bias effect in thin film structures. This is due to its implementation in devices such as spin valves in magnetoresistive sensors and non-volatile magnetic random access memory cells (MRAM) (for recent reviews, see [97, 98]). While the basic mechanisms of exchange bias are qualitatively well understood, to obtain a quantitative understanding of the effect is challenging in view of the

frequently used complex chemical structures and electronic interactions at actual FM/AF thin film interfaces. In order to test the applicability of theoretical models it would be highly desirable to investigate AF/FM interfaces that are structurally as perfect as possible. In this regard, FePt₃ is a remarkable exception because, depending on the degree of chemical order, it can, at the same temperature and composition, develop either FM or AF magnetic order [99, 100].

The crystal structure of FePt₃ is similar to Cu₃Au which is a prototype for a chemical order-disorder transition. Stoichiometric FePt₃ in perfectly chemically ordered face-centered cubic (fcc) L1₂ structure shows antiferromagnetic order below T_N = 160 K. In this structure, the chemical order corresponds to the Fe atoms occupying the corners and the Pt atoms occupying the faces of the cubic cell. The Fe moments (m_{Fe} = 3.3 μ_B extrapolated to T = 0 K) order on (110) alternating ferromagnetic subsheets, while the Pt atoms carry a small moment (m_{Pt} < 0.2 μ_B).

The AF ordered magnetic phase of FePt₃ is very sensitive to plastic deformation resulting in chemical disorder [100, 101]. Plastic deformation with consequential increased dislocation densities can be obtained by cold working the chemically ordered alloy, which, in turn, leads to Fe atoms occupying face centered positions rather than corner positions in the fcc ordered lattice [101, 102]. As a result, the positive exchange between next neighbor Fe atoms introduces a tendency to FM order. Completely disordered FePt₃, has an fcc structure in which each lattice site is occupied by, on average, ¼ Fe and ¾ Pt atoms, where the atomic fractions represent probabilities. Chemically disordered bulk FePt₃ shows FM order at temperatures below about 425 K (m_{Fe} = 4.0 μ_B and m_{Pt} < 0.2 μ_B).

In this chapter, we demonstrate that the chemical ordering of epitaxial films can be controlled by varying the substrate temperature during growth. The design of this experiment was stimulated by a prior result where we studied a superlattice of CoPt₃/FePt₃. It was expected

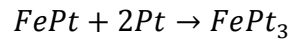
that such a superlattice would constitute a FM/AF system since the perfectly ordered films are FM for CoPt₃ and AF for FePt₃. However, a detailed analysis of the data showed that a portion of the FePt₃ contributed to the ferromagnetism of the sample [103]. These results show the tantalizing result that a properly designed sample may exhibit a new result—namely a material which is exchange biased with itself. Our preliminary results are promising and show that a film produced by modulating the substrate temperature during growth has a significant ferromagnetic fraction with a Curie temperature near 300K.

8.1 Sample Preparation

The FePt₃ films were deposited on MgO (100) substrates and sapphire (Al₂O₃) substrates by co-sputtering with a Fe₅₀Pt₅₀ alloy target and a pure Fe target.

Sputtering rate determination

FePt₃ thin films were deposited by co-sputtering with a Fe₅₀Pt₅₀ alloy target and a pure Pt target in a reaction given by



Thus, the relation of FePt sputtering rate and Pt sputtering can be expressed as:

$$\frac{R_{FePt} \times t \times S \times \rho_{FePt}}{M_{FePt}} = \frac{R_{Pt} \times t \times S \times \rho_{Pt}}{2M_{Pt}} \quad (8.1)$$

where t is the sputtering time; S is the area of the substrate; R_{FePt} and R_{Pt} are the sputtering rates of FePt and Pt; and ρ_{FePt} , ρ_{Pt} , M_{FePt} , and M_{Pt} are the densities and molar masses of FePt and Pt, respectively.

The sputtering rate of FePt can be expressed as:

$$R_{FePt} = \frac{R_{Pt} \times \rho_{Pt} \times M_{FePt}}{2M_{Pt}\rho_{FePt}} \quad (8.2)$$

8.2 Determination of Order Parameter and Growth Temperature

Determination of order parameter FePt₃

Ordered FePt₃ has L1₂ structure with Fe atoms at the corner and Pt atoms at the face centers. The structure factor of FePt₃ can be expressed as:

$$F = \begin{cases} f_{Fe}e^{-W_{Fe}} + 3f_{Pt}e^{-W_{Pt}} & \text{for the (002) peak} \\ f_{Pt}e^{-W_{Pt}} - f_{Fe}e^{-W_{Fe}} & \text{for the (001) peak} \end{cases} \quad (8.3)$$

where $f_{Fe(Pt)}$ is the atomic scattering factor of a Fe(Pt) atom and $e^{-W_{Fe(Pt)}}$ represents the Debye-Waller correction for Fe (Pt) atoms. The $|F|^2$ can thus be expressed as:

$$|F|^2 = FF^* = \begin{cases} [(R_{Fe}e^{-M_{Fe}} + 3R_{Pt}e^{-M_{Pt}})^2 + (R_{Fe}\Delta_{Fe}e^{-M_{Fe}} + R_{Pt}\Delta_{Pt}e^{-M_{Pt}})^2] \\ [(R_{Pt}e^{-M_{Pt}} - R_{Fe}e^{-M_{Fe}})^2 + (\Delta_{Pt}e^{-M_{Pt}} - \Delta_{Fe}e^{-M_{Fe}})^2] \end{cases} \quad (8.4)$$

Where $R_{Fe/Pt}$ and $\Delta_{Fe/Pt}$ represent the real and imaginary parts of the atomic scattering factors of Fe or Pt atoms. After considering the thickness factor (G_t) and Lorentz polarization factor (LP), the intensity can be expressed as:

$$I = G_t \times (LP) \times \begin{cases} [(R_{Fe}e^{-M_{Fe}} + 3R_{Pt}e^{-M_{Pt}})^2 + (R_{Fe}\Delta_{Fe}e^{-M_{Fe}} + R_{Pt}\Delta_{Pt}e^{-M_{Pt}})^2] \\ [(R_{Pt}e^{-M_{Pt}} - R_{Fe}e^{-M_{Fe}})^2 + (\Delta_{Pt}e^{-M_{Pt}} - \Delta_{Fe}e^{-M_{Fe}})^2] \end{cases} \quad (8.5)$$

in which the thickness factor (G_t) and the Lorentz polarization factor (LP) can be calculated by using the methods described in chapter 6.

All the parameters for the calculation of the (001) and (002) peak intensity of fully ordered FePt₃ thin film are shown in Table 8.1.

Table 8.1. Parameters for the calculations of (001) and (002) peak intensities.

Peak	theta	LP	W_{Fe}	R_{Fe}	Δ_{Fe}	W_{Pt}	R_{Pt}	Δ_{Pt}	μ (cm ⁻¹)
(001)	11.45	4.75	0.0064	21.01	3.4	0.0064	64.43	8	3668
(002)	23.4	2.015	0.023	16.93	3.3	0.022	55.12	7	3668

After the intensities for the (001) and (002) peaks have been calculated, the peak intensity ratio of (001) and (002) peaks for perfectly chemical ordered FePt₃ with different thickness was obtained. For a 30nm film the calculated intensity ratio is $I_{001}:I_{002} = 1:4.4$; for 150 nm film, this ratio is 1:3.9. A fully chemically ordered film has order parameter $S=1$ and a chemically-disordered film has an order parameter $S = 0$. In between, the order parameter can be calculated from the intensity ratio by using the equation

$$S^2 = \frac{(I_{001}/I_{002})_{exp}}{(I_{001}/I_{002})_{Cal}^{S=1}} \quad (8.6)$$

Here, $(I_{001}/I_{002})_{exp}$ represents the ratio of peak intensities obtained by experimental measurement and $(I_{001}/I_{002})_{Cal}^{S=1}$ represents the calculated ratio of peak intensities for fully ordered FePt₃.

Determination of growth temperature

Our final goal is to study the interface of FePt₃ (ordered)/FePt₃ (disordered) by using neutron reflectivity. To perform neutron reflectivity measurements, it is desirable to have a periodic variation of the film structure with a few repeats. The periodicity must correspond to the inverse of the momentum transfer range of the instrument to enable the observation of Bragg peaks in the reflectivity data. The disordered phase should be deposited at low temperature and the ordered phase should be deposited at high temperature. After the deposition of one phase is finished, the temperature is changed to deposit another phase. The sputtering is not stopped during the change of temperature. Therefore, the film deposited during the change of temperature will be partially ordered. To minimize the partially ordered phase, it is desirable to find the highest growth temperature that does not produce significant chemical ordering and the lowest growth temperature that produces almost complete chemical ordering.

Fig. 8.1 shows X-ray diffraction results for three films with a total $\text{Fe}_{25}\text{Pt}_{75}$ thickness of 30 nm. For all the films, the (002) peak appears at the same position with $2\theta=46.9^\circ$ which corresponds to a lattice constant $c=3.88 \text{ \AA}$. For the film deposited at 400°C , the intensity of the 001 peak is zero, so the film is completely disordered. This temperature was selected as the low temperature of our modulated structure. The film deposited at 600°C has an intensity ratio of 1/5.5 which corresponds to an order parameter of 0.9. This temperature was selected as the high temperature of our modulated structure to minimize the time it takes to change the temperature between individual layers. Almost perfect order, $S=0.99$, is obtained for a film deposited at 700°C , but it takes nearly twice as long to cool the sample to 400°C from this temperature. Our prior results of neutron scattering measurements of the antiferromagnetic order in these materials have shown that the presence of chemical order is directly correlated to the existence of antiferromagnetic phases within the material [103, 104].

In Fig. 8.1.c, the film is composed of 20 nm of $\text{Fe}_{25}\text{Pt}_{75}$ deposited at 600°C and 10 nm deposited at 400°C , so the order parameter should be $S = 0.9 \times 2/3 = 0.6$. Using Eq. 8.6, the ratio of 1/9.5 from the measurement and the ratio of 1/4.4 from calculation for fully ordered FePt_3 with the same thickness, we obtain an order parameter of $S = 0.68$, experimentally. This clearly shows that the bilayer film has a modulation in the order parameter as a result of a change in temperature during growth. The amount of order is higher than the portion of the film deposited at higher temperature. The reason is that part of the 10 nm disordered $\text{Fe}_{25}\text{Pt}_{75}$ was deposited during the decreasing of temperature and this part (about 2-3nm) is partially ordered with order parameter $S>0$.

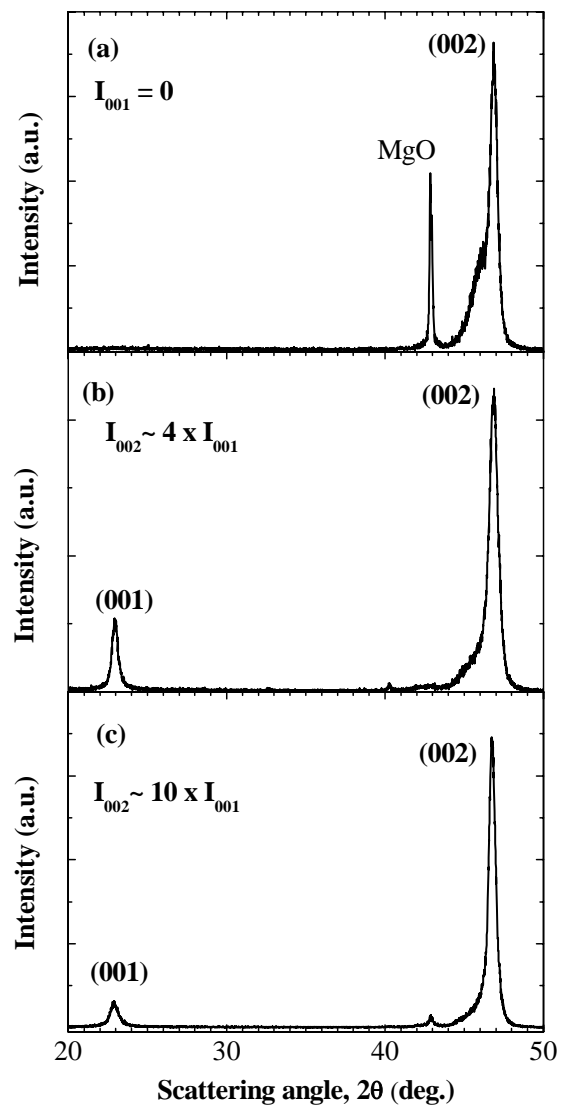


Fig. 8.1. X-ray diffraction patterns of films deposited at different temperatures.

8.3 Order Parameter Modulation in FePt₃ (Ordered)/FePt₃ (Disordered) Superlattices

Order parameter modulation in [FePt₃(x nm) (600°C)/FePt₃ (10nm) (400°C)]₅ films

Samples with five interface repetitions were chosen to fabricate for neutron reflectivity measurement. These samples were made with the ordered FePt₃ layers having thickness $x = 20$, 30, and 40 nm. The X-ray diffraction data for the superlattice films are shown in Fig. 8.2. For the sample with $x = 20$ nm, if the modulation is perfect, the measured order parameter should be the same as the bilayer, since the relative amounts of chemically-ordered and chemically-disordered material are the same as in the bilayer sample. From the data, an order parameter for the film with $x = 20$ nm was calculated. It is found that the order parameter S is 0.67, which is almost the same as that of the bilayer. Therefore, this sample has almost perfect modulation. With the increase of x , the order parameter increases because the amount of chemically ordered material increases. However, according to the analysis of the X-ray data, the order parameter is 0.63 for the sample with $x = 30$ nm and is 0.57 for $x = 40$ nm, showing a decrease in the order parameter with the increase of x . This is most likely a consequence of an increase in disorder as a function of film thickness and may originate from depositing the chemically-ordered material on top of the chemically-disordered material. It seems that 20 nm is a good choice for the thicknesses of ordered FePt₃ layers to make perfect order parameter modulation.

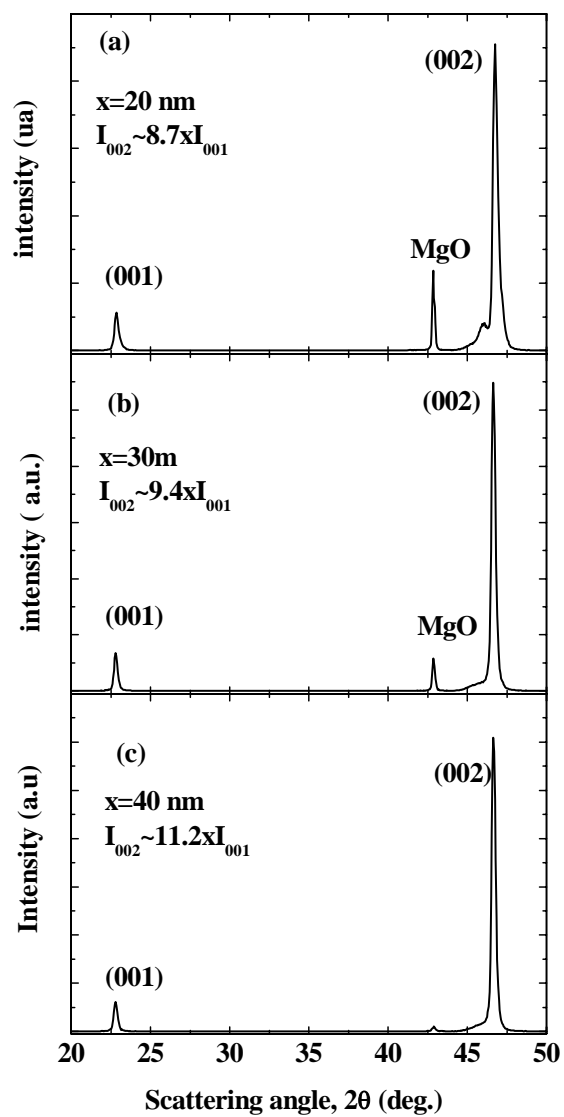


Fig. 8.2. X-ray diffraction spectra of MgO/Pt(4nm)/Cr(3nm)[FePt₃(x nm)(600°C)/FePt₃(10nm)(400°C)]₅.

Order parameter modulation in $[\text{FePt}_3(20 \text{ nm}) (600^\circ\text{C})/\text{FePt}_3(10 \text{ nm}) (500^\circ\text{C})]_5$ films

To investigate the effect of the deposition temperature of the disordered phase on the order parameter, a five-interface superlattice $[\text{FePt}_3(20 \text{ nm}) (\text{ordered})/\text{FePt}_3(10 \text{ nm})]_5$ film was fabricated, in which the 20 nm ordered FePt_3 layers were still deposited at 600°C while the 10 nm disordered FePt_3 layers were deposited at 500°C . The X-ray diffraction result is shown in Fig. 8.3. From X-ray data, the order parameter of this sample was found to be 0.71, which is larger than the sample with the same structure and a deposition temperature of 400°C for disordered layers.

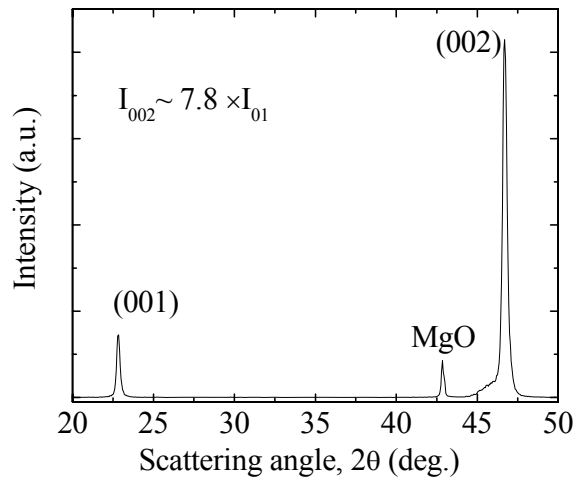


Fig. 8.3. X-ray diffraction pattern of $\text{MgO}/\text{Pt}(4 \text{ nm})/\text{Cr}(3 \text{ nm})[\text{FePt}_3(20 \text{ nm})(600^\circ\text{C})/\text{FePt}_3(10 \text{ nm}) (500^\circ\text{C})]_5$.

8.4 Magnetic Spin Configurations of a Fully Ordered FePt_3 Film

The $\text{Fe}_x\text{Pt}_{100-x}$ ($23 \leq x \leq 29$) alloys in bulk form were studied with neutron diffraction by Bacon [105]. Bulk FePt_3 exhibits an antiferromagnetic spin structure with a wave vector $Q_1 = 2\pi/a (\frac{1}{2} \frac{1}{2} 0)$ below $T_{N1} \sim 160 \text{ K}$. When $x > 26$, a spin structure transition to a second

antiferromagnetic phase, $Q_2 = 2\pi/a$ ($\frac{1}{2} 0 0$) occurs below $T_{N2} \sim 100$ K. The Q_1 phase is further suppressed when x reaches 30.

To study the antiferromagnetic configuration of our samples, unpolarized neutron diffraction measurements were performed. Fig. 8.4 shows the temperature dependence of intensity of the ($\frac{1}{2}, \frac{1}{2}, 0$) peak of the ordered FePt₃ film which was deposited at 600°C. Peaks with half integer index represent the diffraction of an antiferromagnetic configuration.

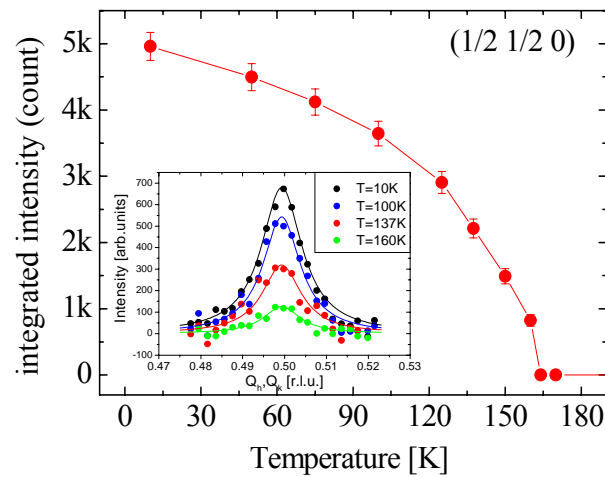


Fig. 8.4. Temperature dependence of the ($\frac{1}{2} \frac{1}{2} 0$) neutron scattering peak of the fully ordered FePt₃ film.

With the decrease of temperature, the peak intensity increases, which means antiferromagnetic order along ($\frac{1}{2} \frac{1}{2} 0$) increases. The peak disappears when the temperature is higher than 160k. This result is in good agreement with what was reported [100]. Since we did not find the antiferromagnetic configuration along ($\frac{1}{2} 0 0$) even at low temperature (<100K), we can conclude that Fe is deficient in our sample ($x < 25$).

The temperature dependence of (200) and (110) peaks of the ordered FePt₃ film are shown in Fig. 8.5. Peaks with integer index represent the diffraction of the ferromagnetic configuration. The intensities of both peaks do not change significantly with temperature, so

these peaks are produced solely by the diffraction of nuclei of the atoms. There is no contribution from magnetic diffraction. Therefore, there is little or no ferromagnetic phase in the film.

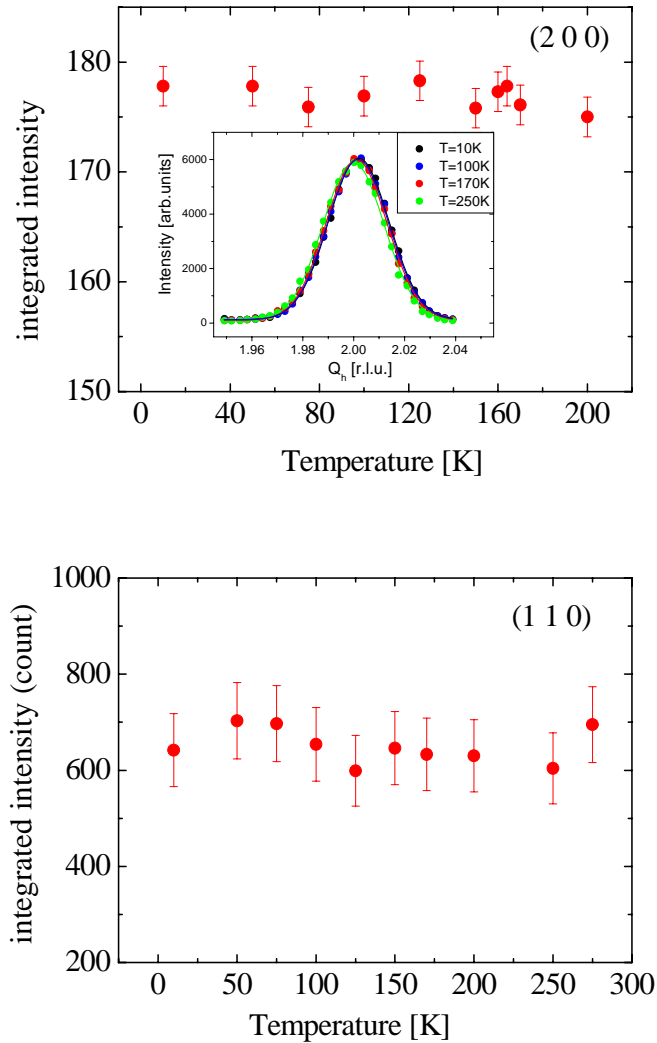


Fig. 8.5. Temperature dependence of (200) and (110) peaks of the fully ordered FePt₃ film.

In our previous study, we found that the FePt₃ film deposited at 600°C was not fully ordered with order parameter 0.9 instead of 1. If the film has stoichiometry FePt₃, a small amount of the ferromagnetic phase should be found. Since no ferromagnetic phase was found in the film, we

can reasonably predict that the order parameter less than 1 is due to Fe deficiency, not the deposition temperature.

8.5 Magnetic Structure and Interface of $[\text{FePt}_3(\text{Ordered})/\text{FePt}_3(\text{Disordered})]_n$ Superlattice Films on MgO Substrates

Determination of roughness of interface by X-ray reflectivity

By using WinGixa, X-ray reflectivity data can be fitted and the roughness information at each interface can be obtained. This information will be helpful in analyzing neutron reflectivity data. Fig. 8.6 is the X-ray reflection data and fitting of sample MgO/Cr(4nm)/Pt(12nm)/ $[\text{FePt}_3(20\text{nm})(600^\circ\text{C})/\text{FePt}_3(10\text{nm})(400^\circ\text{C})]_5/\text{Pt}(5\text{nm})$. FePt_3 layers were deposited at 600°C and 400°C respectively. The fitting is very good. The related parameters for the fitting model are shown in Table 8.2. The actual thickness of the Cr layer is lower than the designed value and the thicknesses of the Pt layers are higher than the designed values.

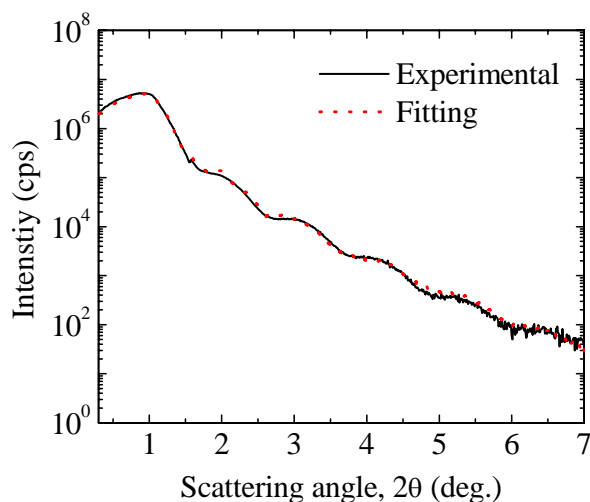


Fig. 8.6. X-ray reflectivity spectrum of a $[\text{FePt}_3/\text{FePt}_3]_n$ superlattice film and its fit.

Table 8.2. Model for the X-ray reflectivity fitting.

Layer	Thickness (nm)	Rms roughness (nm)
Pt	7.5	0.8
FePt ₃	10	0.7
FePt ₃	20	0.7
Pt	16	0.4
Cr	3	0.3
MgO		0.2

Neutron reflectivity and fittings

Our neutron reflectivity measurements were taken at the Spallation Neutron Source at Oak Ridge National Lab with a 1T magnetic field applied to the sample to saturate the magnetic layer during the measurement. The reflectivity spectra were recorded at different temperatures – 5 K, 75 K, 150 K and 300 K.

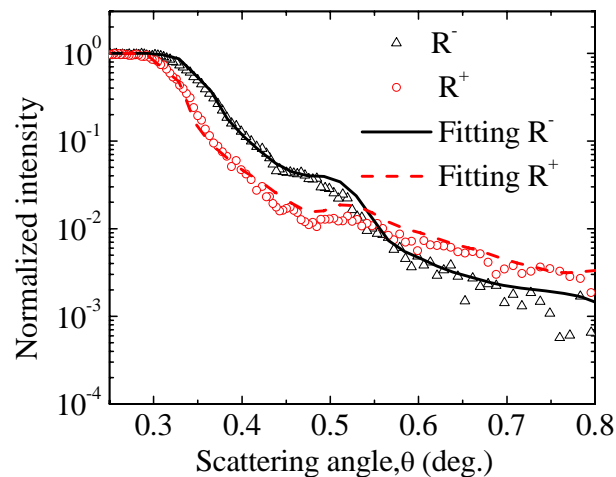


Fig. 8.7. Neutron reflectivity spectra of MgO/Cr(3nm)/Pt(16nm)/[FePt₃(20nm)(600°C)/FePt₃(10 nm)(400°C)]₅/Pt(7.5nm) at a temperature of 5K and their fits.

By using SimulReflec software, the neutron reflectivity spectra can be fitted. All the fittings in this chapter include both the contributions from spin-flip and non spin-flip channels. Therefore, the reflectivity of spin up reflection is $R^+ = R^{++} + R^{+-}$ and the reflectivity of spin down

refection is $R^- = R^- + R^+$. The volume of the FePt_3 unit cell used in the fittings is 58.4 \AA^3 , which corresponds to a lattice constant of 3.88 \AA .

The neutron reflectivity spectra at a temperature of 5 K and the corresponding fits for $\text{MgO}/\text{Cr}(3\text{nm})/\text{Pt}(16\text{nm})/[\text{FePt}_3(20\text{nm})(600^\circ\text{C})/\text{FePt}_3(10\text{nm})(400^\circ\text{C})]_5/\text{Pt}(7.5\text{nm})$ are shown in Fig. 8.7. Note that the thicknesses indicated here are actual values obtained from X-ray reflectivity fitting described above not the designed values. In the fitting model, we use the values obtained from X-ray reflectivity for the thickness and roughness of each layer.

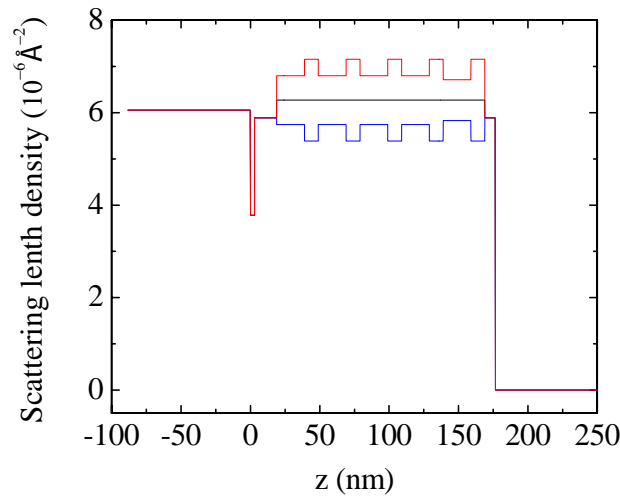


Fig. 8.8. Scattering length density profile of $\text{MgO}/\text{Cr}(3\text{nm})/\text{Pt}(16\text{nm})/[\text{FePt}_3(20\text{nm})(600^\circ\text{C})/\text{FePt}_3(10 \text{ nm})(400^\circ\text{C})]_5/\text{Pt}(7.5\text{nm})$.

The corresponding scattering length density profile is shown in Fig. 8.8. As we can see, the FePt_3 layers deposited at 600°C have an average magnetic moment $1.2 \mu_B$ per unit cell. According to our neutron diffraction results, the FePt_3 film deposited at 600°C does not have a ferromagnetic phase, so we guess this moment comes from the partially ordered phase formed during the deposition temperature changes. The layers deposited at 400°C have an average magnetic moment of $2.2 \mu_B/\text{cell}$, and the last layer has an average magnetic moment of 2.4

μ_B/cell . This moment is smaller than the moment of a Fe atom in FCC FePt_3 which should be $4 \mu_B/\text{cell}$.

8.6 Magnetic Structure and Interface of $[\text{FePt}_3(\text{Ordered})/\text{FePt}_3(\text{Disordered})]_n$ Superlattice Films on Sapphire Substrates

So far, we have only shown the results of $\text{FePt}_3(\text{ordered})/\text{FePt}_3(\text{disordered})$ multilayer films on MgO substrate. To study the effect of crystal orientation on the magnetic structure and magnetic properties of $\text{FePt}_3(\text{ordered})/\text{FePt}_3(\text{disordered})$ multilayer films, we also deposited multilayer films on (1102) sapphire (Al_2O_3) substrates.

Fig. 8.9 shows the X-ray diffraction data of $\text{Al}_2\text{O}_3/\text{Pt}(16\text{nm})/[\text{FePt}_3(40\text{nm})(600^\circ\text{C})/\text{FePt}_3(10\text{nm})(400^\circ\text{C})]_5/\text{Pt}(7.5\text{nm})$. FePt_3 layers are epitaxially grown on a sapphire substrate with perfect (111) orientation.

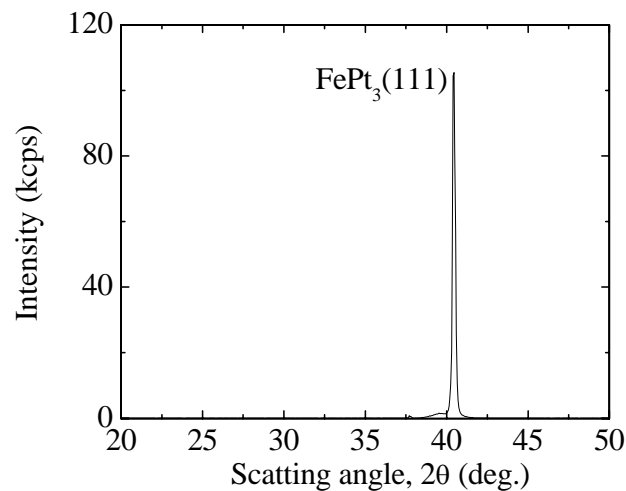


Fig. 8.9. X-ray diffraction spectrum of $\text{Al}_2\text{O}_3/\text{Pt}(16\text{nm})/[\text{FePt}_3(40\text{nm})(600^\circ\text{C})/\text{FePt}_3(10\text{nm})(400^\circ\text{C})]_5/\text{Pt}(7.5\text{nm})$.

Neutron scattering of $(\text{FePt}_3/\text{FeP}_3)_n$ on Sapphire substrate

Fig. 8.10 shows the neutron scattering data for $\text{Al}_2\text{O}_3/\text{Pt}(16\text{nm})/[\text{FePt}_3(40\text{nm})(600^\circ\text{C})/\text{FePt}_3(10\text{nm})(400^\circ\text{C})]_5/\text{Pt}(7.5\text{nm})$. The $(\frac{1}{2} \frac{1}{2} 0)$ peak appears at about 160°C , and increases as the temperature decreases. No $(\frac{1}{2} 0 0)$ peak was detected. The $(\frac{1}{2} \frac{1}{2} 0)$ peak comes from the scattering of ordered FePt_3 layers, which means that all ordered FePt_3 layers only exhibit an antiferromagnetic spin configuration with a wave vector $Q_1 = 2\pi/a (\frac{1}{2} \frac{1}{2} 0)$ even at very low temperature. This result is in good agreement with that of the ordered FePt_3 thin film on MgO substrate.

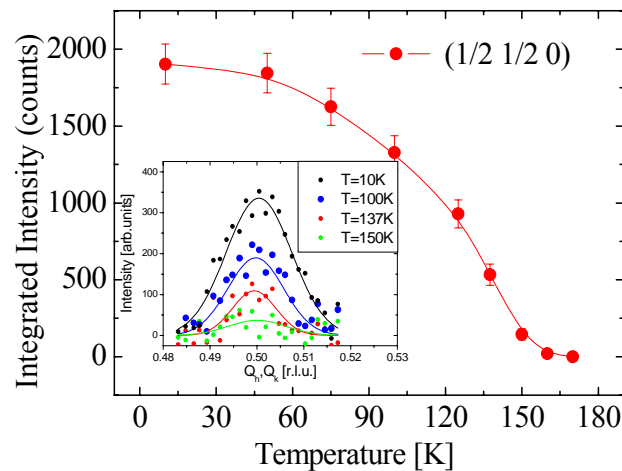


Fig. 8.10. Neutron scattering intensity of the $(\frac{1}{2} \frac{1}{2} 0)$ peak of $\text{Al}_2\text{O}_3/\text{Pt}(16\text{nm})/[\text{FePt}_3(40\text{ nm})(600^\circ\text{C})/\text{FePt}_3(10\text{nm})(400^\circ\text{C})]_5/\text{Pt}(7.5\text{nm})$ as a function of temperature.

The temperature dependences of the (-200) and (110) peaks are shown in Fig. 8.11. There are two contributions to these two peaks: the scattering from atomic nuclei and the scattering from the magnetic configuration. The first contribution does not depend on temperature, but the second does. The increase of the intensity of (-200) and (110) peaks indicates the existence of a ferromagnetic phase. As we showed before, for ordered FePt_3 , the intensities of (100) and (110)

peaks do not change significantly with temperature. Therefore, the increase of intensity with temperature comes from the scattering of disordered FePt₃ layers deposited at 400°C.

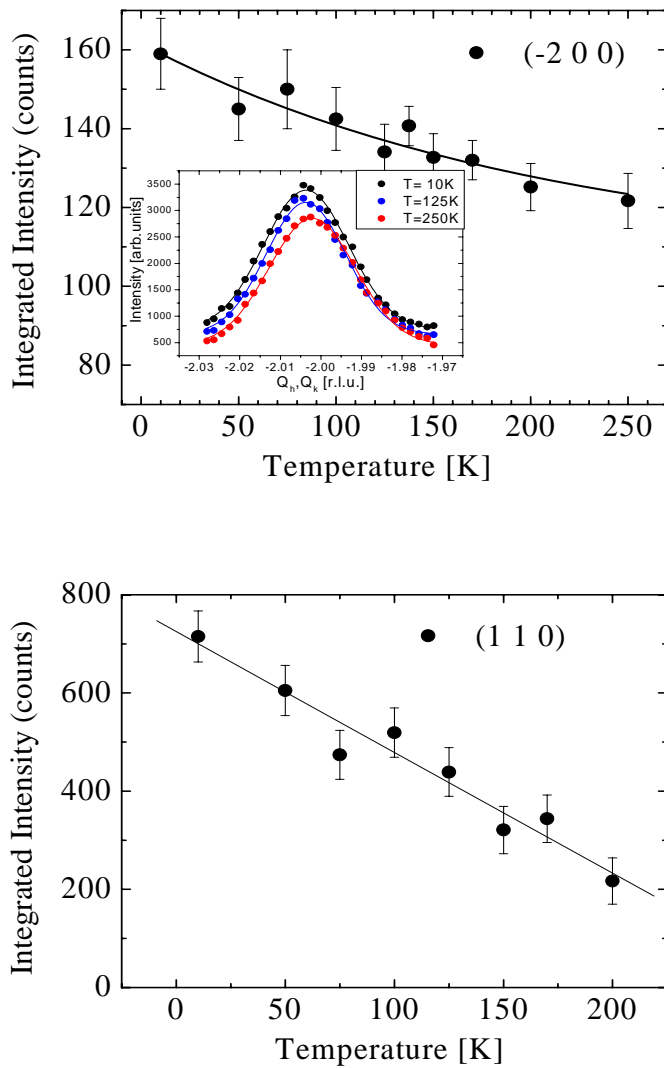


Fig. 8.11. Neutron scattering intensities of (-200) and (110) peaks of Al₂O₃/Pt(16nm)/[FePt₃(40nm)(600°C)/FePt₃(10nm)(400°C)]₅/Pt(7.5nm) as a function of temperature.

Neutron reflectivity study of magnetic structure and interface

Neutron reflectivity measurements of samples on sapphire substrates were carried out with a 5500 Oe magnetic field applied on the sample to saturate the ferromagnetic layers. The X-ray reflectivity spectra were recorded at various temperatures.

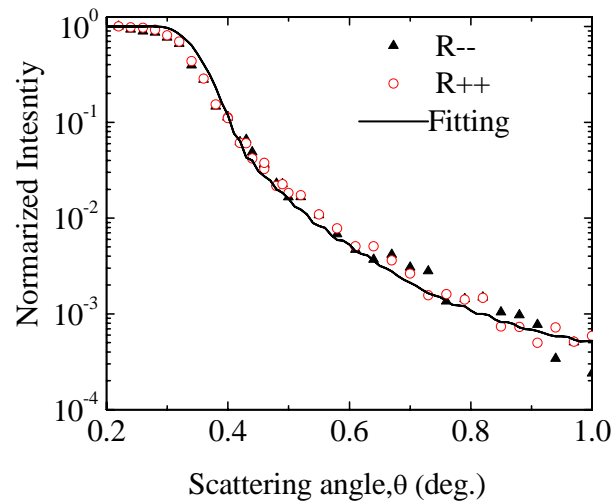


Fig. 8.12. Neutron reflectivity spectra and the fit of $\text{Al}_2\text{O}_3/\text{Cr}(3\text{nm})/\text{Pt}(12\text{nm})/[\text{FePt}_3(40\text{nm})(600^\circ\text{C})/\text{FePt}_3(10\text{nm})(400^\circ\text{C})]_5/\text{Pt}(7.5\text{nm})$ (at 325K).

Table 8.3. Thicknesses and interface roughness in the $\text{FePt}_3/\text{FePt}_3$ superlattice film on a sapphire substrate.

Layer	Thickness (nm)	Rms roughness (nm)
Pt	7.5	2.0
$\left. \begin{array}{l} \text{FePt}_3 \\ \text{FePt}_3 \end{array} \right\} \times 5$	11.0	2.0
$\left. \begin{array}{l} \text{FePt}_3 \\ \text{FePt}_3 \end{array} \right\}$	40.0	2.0
Pt	12.0	0.3
Cr	3.0	0.3
Al_2O_3		0.2

Fig. 8.12 shows neutron reflectivity spectrum of $\text{Al}_2\text{O}_3/\text{Cr}(3\text{nm})/\text{Pt}(16\text{nm})/[\text{FePt}_3(40\text{nm})(600^\circ\text{C})/\text{FePt}_3(10\text{nm})(400^\circ\text{C})]_5/\text{Pt}(7.5\text{nm})$ at a temperature of 325 K and the corresponding fitting. At 325 K, there is no significant difference in the reflectivity curves, which indicates that

at this temperature, the disordered FePt₃ is in a paramagnetic phase. In the fitting, we can neglect the magnetic contribution to the reflectivity spectrum. The thickness and roughness of each layer obtained from curve fitting are shown in Table 8.3. The roughness of FePt₃ superlattice layers is about 2.0 nm.

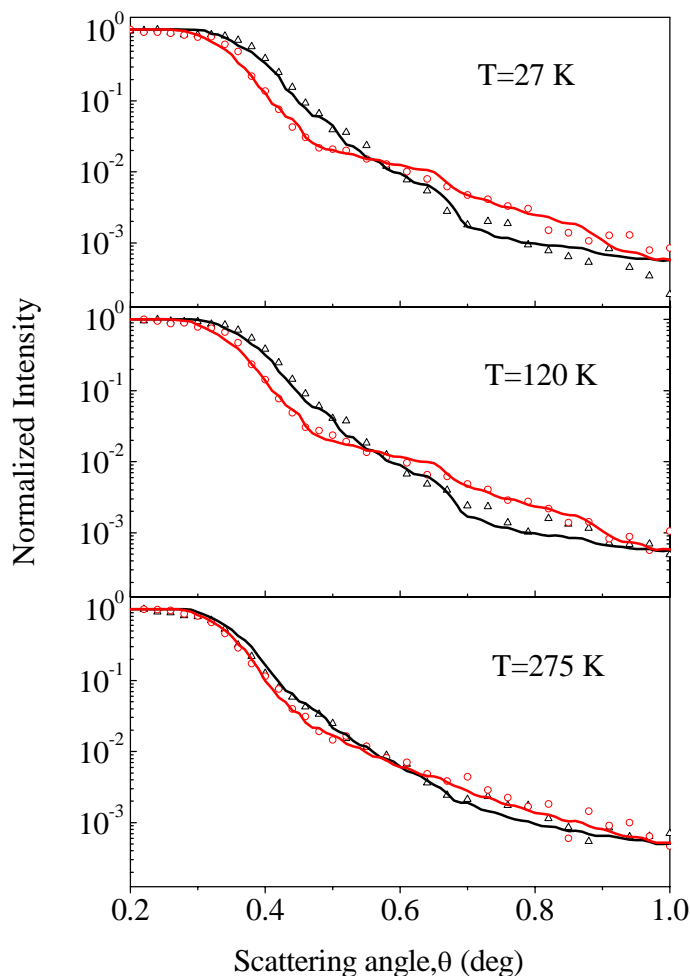


Fig. 8.13. Neutron reflectivity spectra of Al₂O₃/Cr(3nm)/Pt(16nm)/[FePt₃ (40nm)(600°C)/FePt₃ (10nm)(400°C)]₅/Pt(7.5nm) at different temperatures and the related fits.

By using the same model and considering the magnetic contribution, the polarized neutron reflectivity spectra at low temperature were fitted. The spectra and corresponding fits are shown in Fig. 8.13. At 27 K, the average magnetic moment in ordered FePt₃ layers in this

sample is about $1.0 \mu_B/\text{cell}$ and the average magnetic moment of disordered FePt_3 layers is about $3.0 \mu_B/\text{cell}$. With the increase of temperature, the moment of each layer decreases. The magnetization in disordered FePt_3 as a function of temperature is shown in Fig. 8.14.

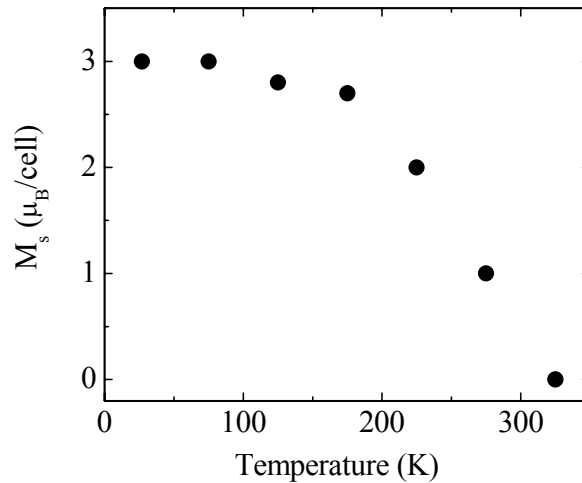


Fig. 8.14. Magnetization in disordered FePt_3 as a function of temperature (derived by fitting).

Fig. 8.15 shows the asymmetry ratio spectra at different temperatures. The asymmetry ratio depends on scattering angle as well as temperature. In all spectra, there is a peak that appears at about 0.44° degree. The peak value decreases with the increase of temperature. To study the dependence of the asymmetry ratio on temperature, we plot peak value as a function of temperature and show it in Fig. 8.16. Since the asymmetry ratio is proportional to the magnetization of the ferromagnetic layers, the change of asymmetry ratio with temperature actually gives the information on the temperature dependence of magnetization. Comparing with Fig. 8.14, we can see that the asymmetry ratio and the magnetization of disordered FePt_3 layers have similar temperature dependence.

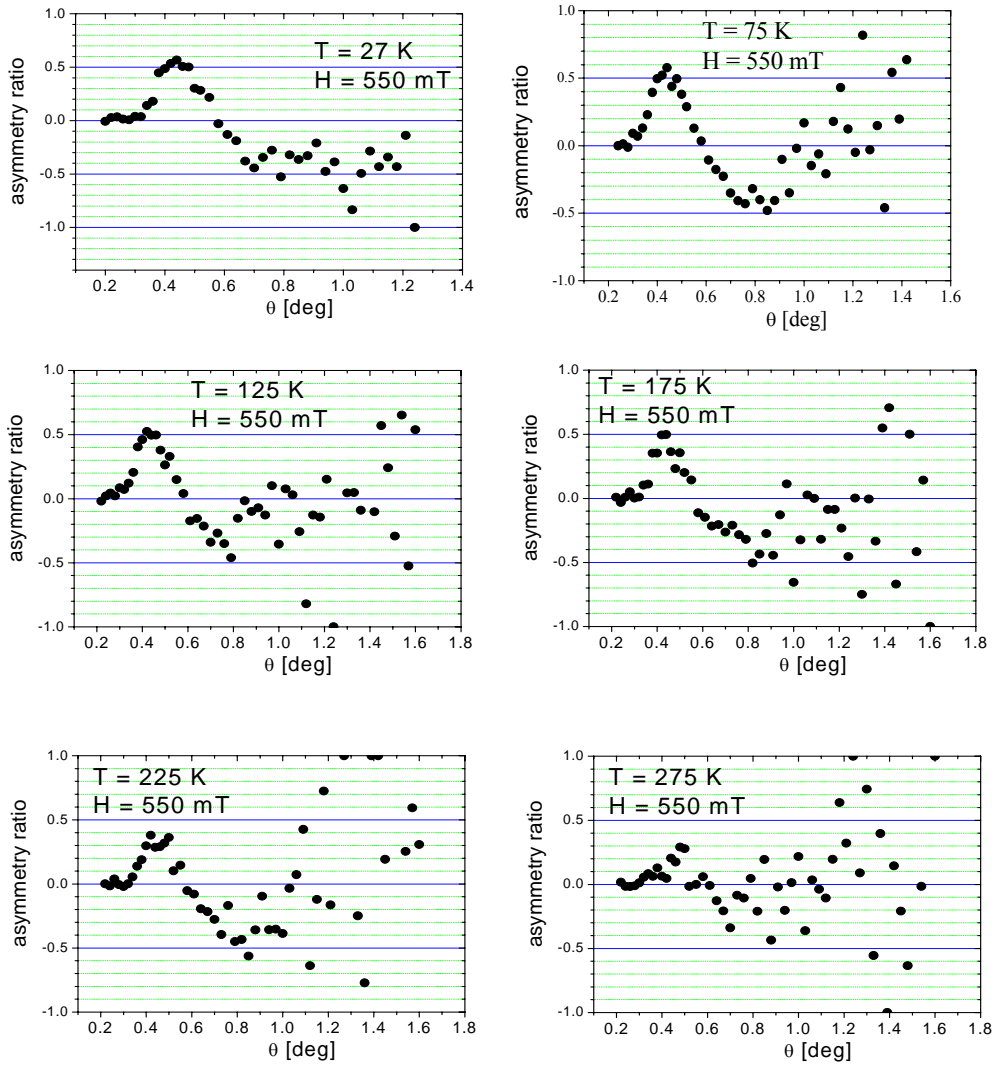


Fig. 8.15. Asymmetry ratio as a function of scattering angle at different temperatures.

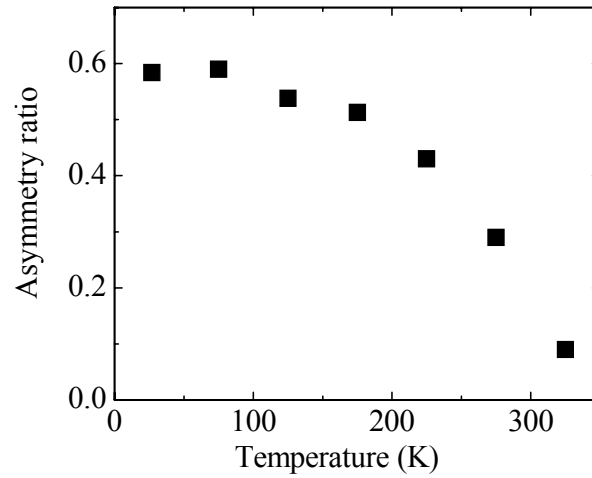


Fig. 8.16. Asymmetry ratio at $\theta = 0.44^\circ$ in disordered FePt_3 as a function of temperature.

8.7 Exchange Bias in $[\text{FePt}_3(\text{Ordered})/\text{FePt}_3(\text{Disordered})]_n$ Superlattice Films

The magnetic properties of the samples were measured by using vibrating sample magnetometry (VSM) at different temperatures. Before the measurement, the samples were cooled down to 5 K in a 1000 Oe applied field to induce unidirectional anisotropy.

Fig. 8.17 shows the hysteresis loops of $\text{MgO}/\text{Cr}(3\text{nm})/\text{Pt}(16\text{nm})/[\text{FePt}_3(20\text{nm})(600^\circ\text{C})/\text{FePt}_3(10\text{nm})(500^\circ\text{C})]_5/\text{Pt}(7.5\text{nm})$ at temperatures of 5 K and 200 K. At different temperatures, the magnetic properties of the sample are quite different: At low temperature, the magnetic moment of the sample is much higher than at high temperature. This is due to the decrease of magnetization of disordered FePt_3 with the increase of temperature as shown in Fig. 8.14. Secondly, the coercivity of the sample at low temperature is much larger than at high temperature. The increase of coercivity can be attributed to the pinning effect of the ordered FePt_3 layer. As neutron scattering results show, ordered FePt_3 is in a paramagnetic phase at high temperature and transitions to an antiferromagnetic phase after the temperature goes below 170

Thirdly, at 5 K, the exchange bias is quite large with a exchange field H_{ex} of about 470 Oe, while at 200 K, H_{ex} is very small (about 5 Oe).

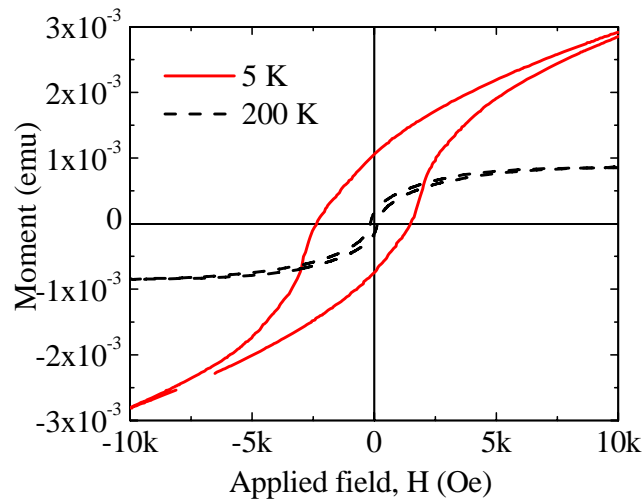


Fig. 8.17. Hysteresis loops of the $[\text{FePt}_3/\text{FePt}_3]_n$ superlattice film deposited on a MgO substrate.

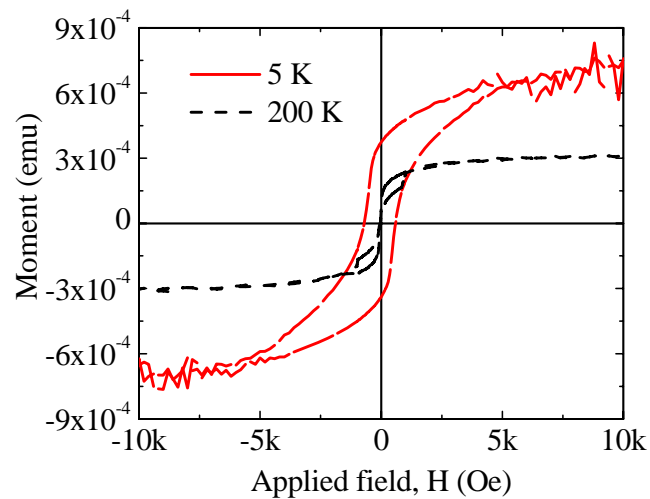


Fig. 8.18. Hysteresis loops of the $[\text{FePt}_3/\text{FePt}_3]_n$ superlattice film deposited on a sapphire substrate.

The hysteresis loops of $\text{Al}_2\text{O}_3/\text{Cr}(3\text{nm})/\text{Pt}(16\text{nm})/[\text{FePt}_3(40\text{nm})(600^\circ\text{C})/\text{FePt}_3(10\text{nm})(400^\circ\text{C})]_5/\text{Pt}(7.5\text{nm})$ at 5 K and 200 K are shown in Fig. 8.18. The coercivity and moment of the

sample decrease with the increase of temperature. At 5 K, the exchange bias of the sample is about 57 Oe, and it goes to zero at 200 K.

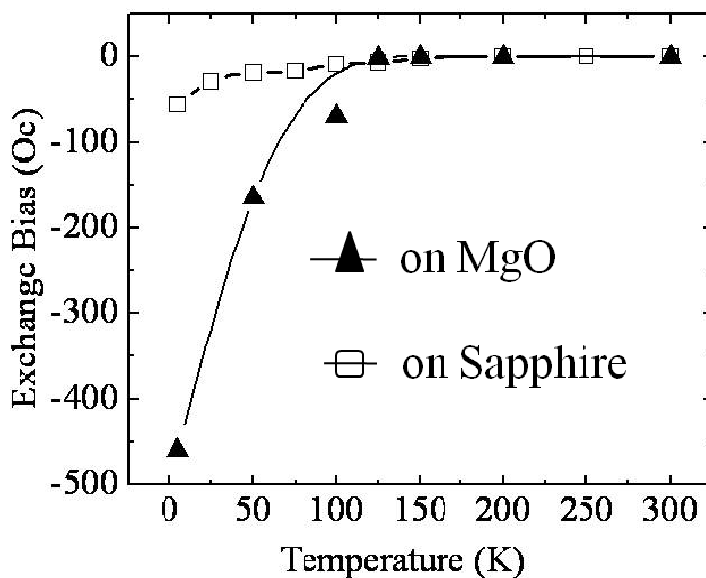


Fig. 8.19. Exchange bias as a function of temperature.

The dependences of the exchange bias field of both samples on temperature are shown in Fig. 8.19. With an increase of temperature, the exchange bias of each sample decreases and goes to zero at around 160 K, which corresponds to the phase transition temperature of ordered FePt₃. However, at low temperature, the exchange bias of MgO/Cr(3nm)/Pt(16nm)/[FePt₃(20nm)(600°C)/FePt₃(10nm)(500°C)]₅/Pt(7.5nm) is much larger than that of Al₂O₃/Cr(3nm)/Pt(16nm)/[FePt₃(40nm)(600°C)/FePt₃(10nm)(400°C)]₅/Pt(7.5nm). One of the reasons for the large value of the exchange bias in the former sample is that FePt₃ layers deposited at higher temperature (500 °C) are partially-ordered instead of fully disordered. The ordered parts in these layers will offer additional exchange bias to the disordered part (self-exchange bias). The different crystal orientation of ordered FePt₃ may be another reason for the difference in exchange bias. The spin

of Fe atoms in the antiferromagnetic phase of FePt₃ may lie along some special direction instead of parallel to the sample surface due to the crystalline anisotropy of antiferromagnetic material. Since the FePt₃ layers have a (001) orientation on MgO substrates and a (111) orientation on sapphire substrates, the exchange coupling between the spins in antiferromagnetic layers and the spins in ferromagnetic layers may be different in these two cases and lead to a difference in exchange bias.

Conclusions

Samples with a modulated order parameter along the growth direction can be produced by varying the substrate temperature during growth. X-ray diffraction measurements confirm that the amount of order is consistent with growth temperature changes for a bilayer film and for a superlattice with the thickness of ordered layers about 20nm. In the case of a superlattice with larger thickness of the ordered layers, the amount of order will be lower than the expected value. By fitting the neutron reflectivity results, it is found: 1) The fully chemically disordered phase of FePt₃ has a Curie temperature of about 325 K. 2) When the FePt₃ layers are deposited at 600°C, they are partially ordered and have some ferromagnetic phase present. 3) FePt₃ layers deposited at 400°C are also partially ordered and contain some antiferromagnetic phase which leads to a decrease of magnetization. 4) In the superlattice deposited on a sapphire substrate, the layers deposited at 400°C have higher magnetization than those in the superlattice deposited on an MgO substrate.

Exchange bias in the superlattice on an MgO substrate is much higher than that in the superlattice on a sapphire substrate. One of the possible reasons is that a larger self-exchange bias exists in the superlattice on the MgO substrate due to a larger amount of antiferromagnetic phase in FePt₃ layer deposited at 400°C.

CHAPTER 9 CONCLUSIONS

Based on a one-dimensional model, a new energy landscape, $E(z)$, is developed to study and compare different kinds of magnetic recording media from the point of view of the figure of merit. In this new energy landscape, both ΔE and H_c of a medium can be directly obtained and the figure of merit can be easily evaluated. By using this method, it is very directly proved that for a given energy barrier and total moment, there is a theoretical limit for the figure of merit which is 4. This theoretical limit corresponds to a linear energy landscape and can be closely achieved by graded media with a quadratic anisotropy profile starting from a zero minimum value ($K(z) \propto z^2$). For a graded medium with a quadratic anisotropy profile starting from a nonzero minimum value, a soft-tail can help to decrease the coercivity and increase the figure of merit. To further enhance the thermal stability of a graded medium, a hard tail can be functional. However, the adding of a hard tail will lead to an increase of coercivity so as to lead to a decrease of figure of merit accordingly. To further push the figure of merit toward the theoretical limit, it is apt to decrease the exchange stiffness constant in the graded media.

By using LLG simulation, the magnetic properties of graded media are studied. It is found that the coercivity obtained by LLG simulation is in very good agreement with what is estimated by the energy landscape. From the comparison of simulated hysteresis loops with and without considering magnetostatic interaction, the magnetostatic interaction is found to increase the coercivity of a graded medium. For a medium with a quadratic anisotropy profile

starting from a zero minimum value, a small lateral field can help to overcome the effect of demagnetization field and decrease the switching field by a small amount. For a medium with a quadratic anisotropy profile starting from a non-zero minimum value, applying a field with 45° from easy axis will greatly decrease the coercivity. By comparing the simulated hard axis loops of graded media with different anisotropy profiles, it is found that the hard axis loop highly depends on the anisotropy profile. Magnetostatic interactions and exchange interactions have only small effects on the hard axis loop. It is possible to determine the anisotropy distribution of an anisotropy graded medium by analyzing its hard axis loop.

By using first principles, the magnetic and electronic structures of three different spin configurations of $L1_0$ structured FePt and MnPt are studied. It is found that the ferromagnetic state of FePt with a c/a value of 0.98 is the most stable state; for MnPt, the most stable state is the antiferromagnetic state with an antiferromagnetic configuration along the (100) direction and a c/a value 0.92. The magnetic state and magnetic properties of both FePt and MnPt are found to depend on the c/a value. For the FePt alloy, with a small decrease of c/a from 0.98, there is a phase competition between ferromagnetic phase and antiferromagnetic phase. For the ground state of MnPt, the energy band is found to have large dispersion at the Fermi energy, which leads to a large velocity for electrons at Fermi energy. This might be one of the reasons for MnPt to have a smaller resistivity than other antiferromagnetic materials.

Epitaxial $Fe_{50}Pt_{50}$ films were fabricated by magnetron sputtering at different growth temperatures. It is found that the anisotropy of $Fe_{50}Pt_{50}$ thin film can be controlled by varying the growth temperature. With the decrease of growth temperature, the chemical order parameter S of $Fe_{50}Pt_{50}$ decreases and the anisotropy decreases. It is also found that the saturation magnetization of $Fe_{50}Pt_{50}$ films does not change significantly with order parameter. $Fe_{50}Pt_{50}$ films

with graded order parameter are also fabricated and studied. The graded films are found to have a much smaller switching field than fully ordered uniform $\text{Fe}_{50}\text{Pt}_{50}$ film. $\text{Fe}_{50}\text{Pt}_{50}$ films with gradient order parameter are very promising in fabrication of graded media.

Epitaxial $\text{Fe}_{100-x}\text{Pt}_x$ films are fabricated to study the possibility of controlling anisotropy by changing composition. It is found that, with the increase of Fe composition, the hard axis loops of epitaxial $\text{Fe}_{100-x}\text{Pt}_x$ films have large coercivities which make it hard to evaluate the anisotropies by analyzing the hard axis loops. One of the reasons for the high anisotropy in the hard axis loop might be that, with the increase of Fe composition, the easy axis of the film tilts from the surface normal due to a large negative K_2 . The tilting of easy axis of $\text{Fe}_{100-x}\text{Pt}_x$ films will lead to a large easy axis dispersion, which is not desirable for making graded media. To avoid the tilting of the easy axis, further investigation of the dependence of magnetic properties $\text{Fe}_{100-x}\text{Pt}_x$ on fabrication process and seed layer selection is needed.

FePt_3 (ordered)/ FePt_3 (disordered) superlattice films are fabricated by varying the substrate temperature during growth. It is found that a modulated order parameter along the growth direction can be achieved. X-ray diffraction measurements confirm that the amount of order is consistent with growth temperature changes for a bilayer film and for a superlattice with the thickness of ordered layers about 20nm. In case of a superlattice with larger thickness in ordered layers, the amount of order will be lower than expected value. The superlattice films are studied by polarized neutron reflectometry (PNR). By fitting the neutron reflectivity results, By fitting the neutron reflectivity results, it is found: 1) The fully chemically disordered phase of FePt_3 has a Curie temperature of about 325 K. 2) When the FePt_3 layers are deposited at 600°C, they are partially ordered and have some ferromagnetic phase present. 3) FePt_3 layers deposited at 400°C are also partially ordered and contain some antiferromagnetic phase which leads to a

decrease of magnetization. 4) In the superlattice deposited on a sapphire substrate, the layers deposited at 400°C have higher magnetization than those in the superlattice deposited on an MgO substrate.

The magnetic properties of all the samples are studied by measuring the hysteresis loops at different temperatures. It is found that the exchange bias in a superlattice on an MgO substrate is much higher than that in a superlattice on a sapphire substrate. One of the possible reasons is that a larger self-exchange bias exists in a superlattice on an MgO substrate due to a larger amount of antiferromagnetic phase in FePt₃ layer deposited at 400°C.

REFERENCES

- [1] <http://www.tomshardware.com/gallery/Historical-Areal-Density-Trend,0101-156599-0----jpg-.html>.
- [2] M. H. Kryder, and R. W. Gustafson, *J. Magn. Magn. Mater.*, **287**, 449 (2005).
- [3] B. Dipert, and L. Hebert, *IEEE. Spectrum* **30**, 48 (1993).
- [4] P. Pavan, R. Bez, P. Olivo, and E. Zanoni, *Proceedings of the IEEE*, **85**, 1248 (1997).
- [5] R. Bez, E. Camerlenghi, A. Modelli, and A. Visconti, *Proceedings of the IEEE*, **91**, 489 (2003).
- [6] G. Lawton, *Computer*, **39**, 16 (2006).
- [7] http://en.wikipedia.org/wiki/solid-state_drive
- [8] <http://embeddedstar.com/weblog/2009/01/25/bitmirco-ssd-ide>
- [9] <http://www.networkworld.com/news/2009/041009-first-512gb-ssd-drive-offered.html>.
- [10] <http://www.pcguide.com/ref/hdd/perf/spec/postransAreal-c.html>.
- [11] W. F. Brown, *Phys. Rev.* **130**, 1677(1963).
- [12] J. L. Dormann, D. Fiorani, and E. Tronc, *Adv. Chem. Phys.* **98**, 283 (1997).
- [13] S. Batra, J. D. Hannary, Z. Hong, and J. S. Goldberg, *IEEE. Trans. Magn.* **40**, 319 (2004).
- [14] H. N. Bertram, J. G. Zhu, *IEEE Trans. Magn.* **27**, 5043 (1991).
- [15] J. G. Zhu and H. Wang, *IEEE Trans. Magn.* **MAG-31**, 1065 (1995). D. N. Lambeth, E. M. T. Valu, G. Bellesis, L. L. Lee, and D. E. Laughlin, *MRS Conf. Proc.* **517**, 217 (1998).
- [16] R. Wood, *IEEE Trans. Magn.* **36**, 36 (2000).

- [17] R. M. Metzger, V. V. Konovalov, M. Sun, T. Xu, G. Zangari, B. Xu, M. Benakli, W. D. Doyle, *IEEE Trans. Magn.* **36**, 30 (2000).
- [18] H. J. Richter, and A. Y. Dobin, *J. Magn. Magn. Mater.* **287**, 41 (2005).
- [19] R. L. White, R. M. H. Newt, and R. F. W. Pease, *IEEE. Trans. Magn.* **33**, 990 (1997)
- [20] J. Lohau, A. Moser, C. T. Rettner, M. E. Best, and B. D. Terris, *Appl. Phys. Lett.* **79**, 990 (2001)
- [21] J. Moritz, L. Buda, B. Dieny, J. P. Mozieres, R. Veerdonk, T. M. Crawford and D. Weller, *Appl. Phys. Lett.* **84**, 1519 (2004).
- [22] B. D. Terris, T. Thomson, and F. Hu, *Microsyst Technol.* **13**, 189 (2007).
- [23] A. Lyberatos, and K. Y. Guslienko, *J. Appl. Phys.* **94**, 1119 (2003).
- [24] K. W. Ng, S. H. Leong, Z. Yuan, B. Liu, and Y. Ma, *Appl. Phys. Lett.* **91**, 172511 (2007).
- [25] W. A. Challener, T. W. McDaniel, C. D. Mihalcea, K. R. Mountfield, K. Pelhos, and I. K. Sendur, *Jpn. J. Appl. Phys.* **42**, 981 (2003).
- [26] J. G. Zhu, X.C. Zhu, and Y. H. Tang, *IEEE. Trans. Magn.* **44**, 125 (2008).
- [27] R. H. Victora, and S. Xiao, *IEEE. Trans. Magn.* **41**, 537 (2005).
- [28] S. Hernandez, M. Kapoor, and R. H. Victora, *Appl. Phys. Lett.* **90**, 132505 (2007).
- [29] J. U. Thiele, S. Maat, and E. E. Fullerton, *Appl. Phys. Lett.* **82**, 2859. (2003).
- [30] D. Goll, S. Macke, and H. N. Bertram, *Appl. Phys. Lett.* **90**, 172506 (2007).
- [31] S. Mukherjee, and L. Berger, *J. Appl. Phys.* **99**, 08Q909 (2006).
- [32] A. Goncharov, T. Schrefl, G. Hrkac, J. Dean, S. Bance, D. Suess, O. Ertl, F. Dorfbauer, and J. Fidler, *Appl. Phys. Lett.* **91**, 222502 (2007).
- [33] D. Suess, J. Fidler, G. Zimanyi, T. Schrefl, and P. Visscher, *Appl. Phys. Lett.* **92**, 173111 (2008).

- [34] R. Skomski, T. A. George, and D. J. Sellmyer, *J. Appl. Phys.* **103**, p. 07F531 (2008).
- [35] S. Y. Chou, P. R. Krauss, W. Zhang, L. Guo, and L. Zhuang, *J. Vac. Sci. Technol.* **15**, 2897 (1997).
- [36] R. Victora and X. Shen, *IEEE Trans. Magn.* **41**, 537 (2005).
- [37] Y. Y. Zou, J. P. Wang, C. H. Hee, and T. C. Chong, *Appl. Phys. Lett.* **82**, 2473 (2003).
- [38] H. J. Richter, *IEEE. Trans. Magn.* **29**, 2258 (1993).
- [39] W. K. Shen, J. M. Bai, R. H. Victora J. H. Judy and J. P. Wang, *J. Appl. Phys.* **97**, 10N531 (2005).
- [40] D. Suess, T. Schrefl, R. Dittrich, M. Krischner, F. Dorfbauer, G. Hrkac, and J. Fidler, *J. Magn. Mater.* **287**, 41 (2005).
- [41] A. Yu. Dobin and H. J. Richter, *Appl. Phys. Lett.* **89**, 062512 (2006).
- [42] H. Kronmüller and D. Goll, *Physica B* **319**, 122 (2002).
- [43] D. Suess, T. Schrefl, S. Fahler, M. Krischner G. Hrkac, F. Dofbauer and J. Fiedler, *Appl. Phys. Lett.* **87**, 012504 (2005).
- [44] D. Suess, *J. Magn. Mater.* **308**, 183 (2007)
- [45] W. H. Meiklejohn, and C. P. Bean, *Phys. Rev.* **105**, 904 (1957).
- [46] A. E. Berkowitz and K. Takano, *J. Magn. Mater.* **200**, 552 (1999).
- [47] H. Ohldag, A. Scholl, F. Nolting, E. Arenholz, S. Maat, A. T. Young, M. Carey and Stohr, *Phys. Rev. Lett.* **91**, 017203 (2003).
- [48] H. Katada, M. Shiimoto, K. Nakamoto, H. Hoshiya, K. Hoshino, and N. Yoshida, *J. Magn. Soc. Jp.* **31**, 31 (2007)
- [49] H. Fukuzawa, H. Yuasa, and H. Iwasaki, *J. Phys. D.* **40**, 1213 (2007).
- [50] X. T. Tang, G. C. Wang, and M. Shima, *Phys. Rev. B.* **75**, 134404 (2007).

- [51] J. Nogues, D. Lederman, T. J. Moran, I. K. Schuller, and K. V. Rao, *Appl. Rev. Lett.* **68**, 3186 (1996).
- [52] I. K. Schuller and J. Nogues, *J. Magn. Magn. Mater.* **192**, 203 (1999).
- [53] Z. Lu, P. B. Visscher, and W. H. Butler, *IEEE Trans. Magn.* **43**, 2941 (2007).
- [54] M. Scheinfein, LLG Micromagnetic SimulatorTM (a commercial micromagnetic simulation program). Information available at <http://llgmicro.home.mindspring.com>.
- [55] Z. Lu, P. B. Visscher, and J. W. Harrell, *J. Appl. Phys.* **103**, 07F507 (2008)
- [56] T. L. Gilbert, *Phys. Rev.* **100**, 1243 (1955).
- [57] J. M. Barandian, M. Vazquez, A. Hernando, J. Gonzalez, and G. Rivero, *IEEE. Trans. Magn.* **25**, 3300 (1989).
- [58] A. Savitzky and M. J. E. Golay, *Anal. Chem.* **36**, 1627 (1964).
- [59] D. Weller and A. Moser, *Proc. IEEE Trans. Magn.* **36**, 10 (1999).
- [60] M. J. Carey, A. B. Banful, L. Folks, and B. A. Gurney, *Appl. Phys. Lett.* **84**, 3097 (2004).
- [61] M. F. Toney, M. G. Samant, T. Lin, and D. Mauri, *Appl. Phys. Lett.* **81**, 4565 (2002).
- [62] C. S. Severin, C. W. Chen, and C. Stassis, *J. Appl. Phys.* **50**, 4259 (1979).
- [63] E. Krén, C. Kádár, L. Pál, J. Sólyom, P. Szabó, and T. Tarnóczi, *Phys. Rev.* **171**, 574 (1968).
- [64] C. W. Chen and R. W. Buttry, *AIP. Conf. Proc.* **24**, 437 (1975).
- [65] C. S. Severin and C. W. Chen, *J. Appl. Phys.* **49**, 1694 (1978).
- [66] G. Brown, B. Kraczek, A. Janotti, T. C. Schulthness, G. M. Stocks, and D. D. Johnson. *Phys. Rev. B* **68**, 052405 (2003).
- [67] G. Kresse and J. Furthmüller, *Comput. Mat. Scie.* **6**, 15 (1996).
- [68] P. Ravindran, A. Kjekshus, H. Fjellvag, P. James, L. Nordström, B. Johansson, and O. Eriksson, *Phys. Rev. B* **63**, 144409 (2001).

- [69] D. C. Jiles, *Introduction of Magnetism and Magnetic Material*, Chapman & Hall, London (1998).
- [70] J. T. Wang, D. S. Wang, Y. Kawazoe, *Appl. Phys. Lett.* **79**, 1507 (2001).
- [71] R. Y. Umetsu, C. Mitsumata, A. Sakuma, and K. Fukamichi, *Trans. Magn. Soc. Jpn.* **3**, 59 (2003).
- [72] W. L. Bragg, *Proceedings of the Cambridge Philosophical Society*, **17**, 43 (1913).
- [73] Manual of Model 2900 MicroMag™ Alternating Gradient Magnetometer.
- [74] O. Halpern and M. H. Johnson, *Phys. Rev.* **55**, 898 (1939).
- [75] R. J. Harrison, *Reviews in Mineralogy & Geochemistry*, **63**, 113 (2006).
- [76] G. Shirane, S. M. Shapiro, and J. M. T. Tranquada, *Neutron Scattering with a Triple-axis Spectrometer*, Cambridge University Press (2002).
- [77] J. Rodriguez-Carvajal, Abstract of the Satellite Meeting on Powder Diffraction of the XV Congress of IUCr, Toulous, France, 127 (1990).
- [78] P. Bomqvist, K. M. Krishnan, S. Srinath, and S. G. E. te Velthuis, *J. Appl. Phys.* **96**, 6523 (2004).
- [79] H. Leeb, M. Simon, K. Nikolics, and J. Kasper, *Physica B* **397**, 50 (2007).
- [80] D. Suess, T. Schrefl, R. Dittrich, M. Kirschner, F. Dorfbauer, G. Hrkac, and J. Fidler, *J. Magn. Magn. Mater.* **290-291**, part 1, 551 (2005).
- [81] S. Okamoto, N. Kikuchi, O. Kitakami, T. Miyazaki, Y. Shimada, and K. Fukamichi, *Phys. Rev. B* **66**, 024413 (2002).
- [82] R. F. C. Farrow, D. Weller, R. F. Marks, M. F. Toney, S. Hom, G. R. Harp, and A. Cebollada, *Appl. Phys. Lett.* **69**, 1166 (1996).

- [83] B. D. Cullity, *Elements of X-ray diffraction*, Addison-Wesley Publishing Company, Inc., (1978).
- [84] J. -U. Thiele, L. Folk , M. F. Toney, and D. K. Weller, *J. Appl. Phys.* **84**, 5686 (1998).
- [85] S. Okamoto, O. Kitakami, and Y. Shimada, *J. Magn. Magn. Mater.* **208**, 102 (2000).
- [86] A. Cebollada, D. Weller, J. Sticht, G. R. Harp, R. F. C. Farrow, R. F. Marks, R. Savoy, J. C. Scott, *Phys. Rev. B* **50**, 3419 (1994).
- [87] Y. K. Takahashi, K. Hono, T. Shima, and K. Takanashi, *J. Magn. Magn. Mater.* **267**, 248 (2003).
- [88] O.A. Ivanov, L. V. Solina, V. A. Demshina, and L. M. Magat, *Fiz. Met. Metalloved*, **35**, 92 (1973).
- [89] Y. M. Hu, J. C. A. Huang, S. Y Huang, and T. H. Wu, *IEEE Trans. Magn.* **37**, 2417 (2001)
- [90] Andrew C. C. Yu, M. M. Mizuno, Y. Sasaki, and H. Kondo, *Appl. Phys. Lett.* **85**, 6242 (2004).
- [91] T. Seki, T. Shima, K. Takanashi, Y. Takahashi, E. Matsubara, and K. Hono, *Appl. Phys. Lett.* **82**, 2461 (2003).
- [92] M. Watanabe, M. Homma, and T. Masumoto, *J. Magn. Magn. Mater.* **117-181**, 1231 (1998).
- [93] M. A. I. Nahid and T. Suzuki, *Appl. Phys. Lett.* **85**, 4100 (2004).
- [94] H. Zabel and D. Samuel, *Springer Tracts in Modern Physics*, Springer, **227**, 97 (2008).
- [95] R. Stamps, *J. Phys. D* **33**, R247 (2000).
- [96] J. Nogués and I.K. Schuller, *J. Magn. Magn. Mater.* **192**, 203 (1999).
- [97] C. Chappert, A. Fert, F.N. Van Dau, *Nature Materials* **6**, 813 (2007).

- [98] S. Parkin, X. Jiang, C. Kaiser, A. Panchula, K. Roche, and M. Samant, Proc. IEEE **91**, 661 (2003).
- [99] G.E. Bacon and J. Crangle, Proc. R. Soc. London, Ser. A **272**, 387 (1963).
- [100] D. Palaith, C. W. Kimball, R. S. Preston, and J. Crangle, Phys. Rev. **178**, 795 (1969).
- [101] S. Maat, O. Hellwig, G. Zeltzer, Eric E. Fullerton, G. J. Mankey, M. L. Crow, and J. L. Robertson, Phys. Rev. B **63**, 134426 (2001).
- [102] D. Lott, F. Klose, H. Ambaye, G. J. Mankey, P. Mani, M. Wolff, A. Schreyer, H. M. Christen and B. C. Sales, Phys. Rev. B **77**, 132404 (2008).
- [103] P. Mani, V.V. Krishnamurthy, S. Maat, A.J. Kellock, J. L. Robertson, and G. J. Mankey, J. Vac. Sci. Technol. A **23**, 785 (2005).
- [104] P. Mani, V.V. Krishnamurthy, J. L. Robertson, F. Klose, and G. J. Mankey, J. Appl. Phys. **99**, 08C109 (2006).
- [105] G. E. Bacon and J. Grangle, Proc. R. Soc. London, Ser. A **272**, 387 (1963).